RESEARCH ARTICLE SUMMARY

VOLCANOLOGY

Magma reservoir failure and the onset of caldera collapse at Kīlauea Volcano in 2018

Kyle R. Anderson*, Ingrid A. Johanson, Matthew R. Patrick, Mengyang Gu, Paul Segall, Michael P. Poland, Emily K. Montgomery-Brown, Asta Miklius

INTRODUCTION: The 2018 rift zone eruption of Kīlauea Volcano, Hawai'i, drained large volumes of magma from the volcano's summit reservoir system, causing high-rate subsidence of the ground surface and withdrawal of an active lava lake. Over the span of 1 week, the surface of the lava lake fell more than 300 m. Continued withdrawal of magma caused the rock above the reservoir to fail, triggering the onset of episodic caldera collapse. Surface collapse began near the evacuated lava lake vent, but as the eruption continued over 3 months, the area of the new caldera expanded to ~5 km^2 and its volume grew to 0.8 km^3. The precursory activity and subsequent growth of the caldera were recorded in far greater detail than was possible at the handful of other caldera collapses observed in the past century. These comprehensive observations permit new insights into the conditions that lead to magma reservoir host rock failure and caldera collapse.

RATIONALE: Volcanic caldera collapses can be highly destructive and create prominent topographic features, but little is known about the architecture of subcaldera magma storage zones or the critical decrease in pressure that triggers collapse. Withdrawal of Kīlauea's lava lake in 2018 can be used to gauge pressure change in the underlying magma reservoir. We developed a model of time-evolving reservoir depressurization to jointly explain lava lake withdrawal rate and the rate and spatial pattern of ground subsidence obtained from radar satellites and a dense local monitoring network.

RESULTS: We tracked the evolution of the magmatic system from steady elastic decompression to inelastic failure. We were able to estimate the location, geometry, volume, and time-evolving pressure within the reservoir as well as conditions required to trigger failure of the overlying crust. Before the onset of collapse, the ground at Kīlauea's summit was subsiding at nearly 10 cm/day, and the lava lake surface was retreating at ~50 m/day. We found that these phenomena were caused by drainage of magma at a high rate from a storage reservoir centered ~2 km below the surface, with a volume of several cubic kilometers. Drainage rapidly reduced reservoir pressure, stressing the surrounding crust. Two weeks after the rift zone intrusion and eruption began to drain magma from the summit, withdrawal of <4% of the stored magma had reduced pressure in the reservoir by ~17 MPa, causing the host rock above it to begin to fail episodically. The episodic collapses loaded the magma with the weight of the roof, increasing its pressure. The final collapse caldera was closely centered over the magma reservoir, and their horizontal dimensions were comparable. However, the estimated reservoir volume was substantially greater than the caldera volume, indicating incomplete evacuation at the end of the eruption.

ON OUR WEBSITE

Read the full article at http://dx.doi.org/10.1126/science.aaz1822

CONCLUSION: Our results tightly constrain the pressure decrease in the magma reservoir before the onset of collapse. Together with geodetic data, this bounds the magma storage volume and the stress changes needed to cause failure of the host rock above the reservoir. Our results demonstrate that a magma reservoir's roof may begin to fail after withdrawal of only a small fraction of the stored magma. At Kīlauea, this process was likely influenced by a relatively thin and wide reservoir roof and preexisting crustal weaknesses, including an established caldera ring-fault system and the lava lake vent. Roof collapses maintained magma pressure, sustaining the eruption, but they did not (as is sometimes assumed) completely repressurize the reservoir. This indicates residual frictional strength on the collapse-bounding faults. The eruption was not terminated by complete evacuation of stored magma, contrary to assumptions sometimes made when interpreting data from past caldera collapses, and indicates that a different process was responsible for the cessation of the eruption. Joint monitoring of ground deformation and lava lake elevation at other volcanoes, when possible, may yield rich insights into magmatic processes and conditions. ■

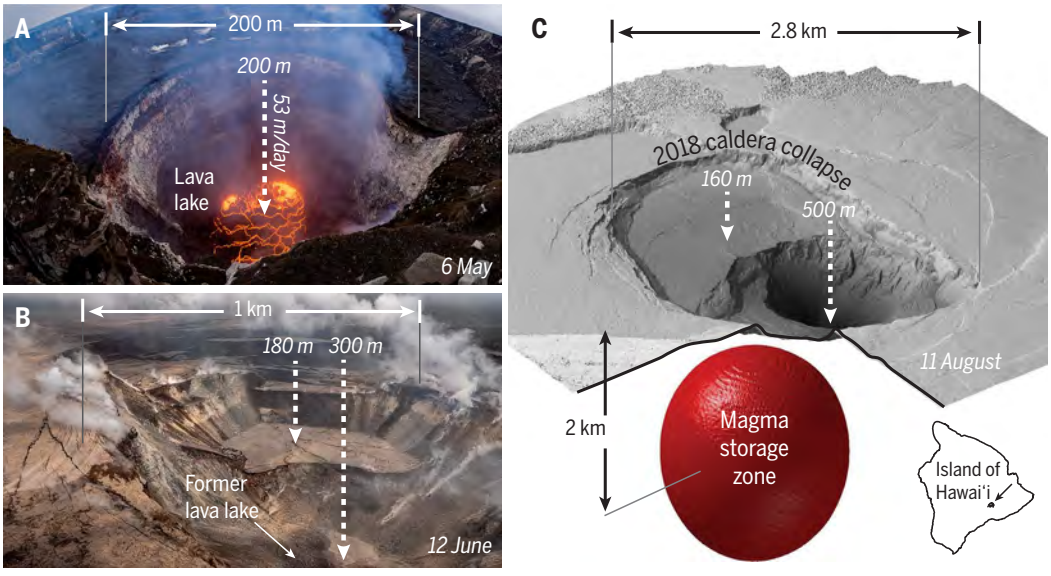

Caldera collapse at Kīlauea in 2018. (**A**) Precollapse lava lake on 6 May 2018. The lake surface had fallen ~200 m since the onset of the eruption. (**B**) Aerial photograph looking west across Kīlauea's summit on 12 June, after the onset of caldera collapse. Parts of the crater floor had subsided as much as ~180 m as intact blocks. (**C**) Estimated magma storage zone that partially collapsed to form the caldera. Shown is the isosurface enclosing the region that contained magma in our simulations, at 95% confidence. View is to the southeast.

PHOTOS: K. R. ANDERSON, U.S. GEOLOGICAL SURVEY

The list of author affiliations is available in the full article online.
*Corresponding author.
Email: kranderson@usgs.gov
Cite this article as K. R. Anderson *et al.*, *Science* **366**, eaaz1822 (2019).
DOI: 10.1126/science.aaz1822

RESEARCH ARTICLE

VOLCANOLOGY

Magma reservoir failure and the onset of caldera collapse at Kīlauea Volcano in 2018

Kyle R. Anderson[1]*, Ingrid A. Johanson[2], Matthew R. Patrick[2], Mengyang Gu[3], Paul Segall[4], Michael P. Poland[5], Emily K. Montgomery-Brown[1], Asta Miklius[2]

Caldera-forming eruptions are among Earth's most hazardous natural phenomena, yet the architecture of subcaldera magma reservoirs and the conditions that trigger collapse are poorly understood. Observations from the formation of a 0.8–cubic kilometer basaltic caldera at Kīlauea Volcano in 2018 included the draining of an active lava lake, which provided a window into pressure decrease in the reservoir. We show that failure began after <4% of magma was withdrawn from a shallow reservoir beneath the volcano's summit, reducing its internal pressure by ~17 megapascals. Several cubic kilometers of magma were stored in the reservoir, and only a fraction was withdrawn before the end of the eruption. Thus, caldera formation may begin after withdrawal of only small amounts of magma and may end before source reservoirs are completely evacuated.

A volcanic caldera is a topographic depression formed by fault-bounded subsidence or collapse of Earth's surface as magma is withdrawn from a crustal storage reservoir, causing the overlying rock to founder (*1*). Caldera formation can be triggered by magma withdrawal to feed violent explosive eruptions or by intrusion of magma into surrounding rock, sometimes feeding long-lived effusive lava flows. Calderas can be prominent topographic features measuring tens of kilometers in diameter.

Our understanding of volcanic caldera collapses has been strongly limited by a lack of well-documented caldera-forming eruptions. From 1900 to the beginning of 2018, only seven caldera collapses were clearly documented on Earth (*2*, *3*), mostly with limited geophysical and observational networks. Even the well-recorded 2014–2015 collapse at Bárðarbunga, Iceland, occurred beneath hundreds of meters of ice, preventing direct observation (*3*).

The 825 million m^3 caldera collapse at Kīlauea Volcano in 2018 was the largest at the volcano in more than two centuries and was tracked by a dense multiparametric monitoring network and through direct visual observations. These detailed datasets record the transition from steady elastic subsidence to fault-bounded collapse as the roof of Kīlauea's summit reservoir failed in response to high-rate magma withdrawal to supply the volcano's East Rift Zone (ERZ) intrusion and eruption. In this study, we modeled ground deformation and lava lake data to infer properties of the magma system as it evolved toward collapse in May 2018. The data offer direct evidence of pressure change in the magma reservoir and present an opportunity to resolve the volcano's subcaldera magma storage architecture and its relation to collapse timing, style, and volume.

[1]U.S. Geological Survey, California Volcano Observatory, Moffett Field, CA, USA. [2]U.S. Geological Survey, Hawaiian Volcano Observatory, Hilo, HI, USA. [3]Department of Statistics and Applied Probability, University of California, Santa Barbara, CA, USA. [4]Department of Geophysics, Stanford University, Stanford, CA, USA. [5]U.S. Geological Survey, Cascades Volcano Observatory Vancouver, WA, USA.
*Corresponding author. Email: kranderson@usgs.gov

Kīlauea Volcano and the 2018 eruption

Kīlauea Volcano, on the island of Hawai'i (Fig. 1), is one of the world's most active volcanoes and erupted almost continuously from 1983 to 2018. For most of that period, Kīlauea's mantle-derived magma supply largely passed through its summit reservoir system before migrating subhorizontally down the volcano's ERZ to erupt as lava flows ~20 km from the summit at or near the Pu'u 'Ō'ō vent.

Beginning in 2008, a lava lake was active at the summit of the volcano within Halema'uma'u crater; by April 2018 its surface area had grown to more than 40,000 m^2. The lava lake was supplied from a shallow magma storage zone (here termed the Halema'uma'u reservoir) hypothesized to exist 1 to 2 km beneath Kīlauea's existing summit caldera (formed in ~1500 CE). Variations in the surface height of the lava lake were strongly correlated with ground deformation, indicating that both were caused by pressure changes in the underlying magma reservoir. Thus, Kīlauea's lava lake acted as a magma reservoir pressure gauge (*4*–*6*).

Kīlauea's 35-year-long eruption ended spectacularly on 30 April 2018 with the intrusion of a dike downrift from Pu'u 'Ō'ō into the volcano's lower ERZ (LERZ) (*7*) (Fig. 1B). On 3 May, the intrusion emerged in the Leilani Estates subdivision, more than 40 km from the volcano's summit, ultimately erupting >1 km^3 of lava and destroying hundreds of homes. The intrusion and eruption triggered wholesale draining of Kīlauea's magma system, from the middle ERZ to the summit. Magma drainage from the summit led to lava lake withdrawal and vent collapse, a series of explosions, and ultimately the formation of a new caldera nested within the larger 1500 CE caldera. Summit collapse and most LERZ lava effusion ended in August 2018 after 3 months.

Magma evacuation and the onset of caldera collapse

We recorded subsidence and later collapse of the ground surface at Kīlauea's summit by visual observations, continuous Global Navigation Satellite System (GPS) stations, borehole tiltmeters, and interferometric synthetic aperture radar (InSAR) interferograms derived from satellite data (*8*) (Figs. 2 to 4). Variation in lava lake surface height was recorded by laser rangefinder, thermal camera imagery, and structure-from-motion photogrammetry (Figs. 3 and 4) (*9*).

Before the onset of the LERZ intrusion, Kīlauea's lava lake had been overflowing onto the floor of Halema'uma'u crater. Deflation began in earnest on 2 May with subsidence and contraction of the ground surface and withdrawal of the lava lake at a rate that reached ~40 m/day (Fig. 3 and fig. S8). On 4 May, an earthquake with moment magnitude (M_w) of 6.9 (M6.9) on the basal decollement between the volcanic pile and the oceanic crust underlying Kīlauea's south flank (*7*, *10*) shook the volcano and produced long-wavelength extensional strain across the summit. By the end of the day, lake withdrawal had accelerated to 53 m/day, and the ground tilt rate at summit instruments had more than doubled (*8*) (Fig. 4). Subsidence continued over the following days in a broad, roughly circular region centered near the east rim of Halema'uma'u at rates of up to nearly 10 cm/day (Fig. 2). Ground deformation and lava lake surface height were highly correlated (Fig. 3D). Before the M_w 6.9 earthquake, we observed ~5 m of lava lake withdrawal for every microradian of caldera-directed ground tilt at station UWE [located near the U.S. Geological Survey (USGS) Hawaiian Volcano Observatory (HVO); Fig. 2], in agreement with observations made over many years at Kīlauea (*4*, *5*). After the earthquake, this ratio had decreased by ~40%.

Rapid withdrawal of the lava lake was accompanied by sporadic explosions as unsupported conduit wall rock fell into the vent (Fig. 1), gradually increasing its diameter (Fig. 4). By 10 May, after dropping more than 300 m in just over a week (supplementary movie S1), the lava lake had disappeared from view and the vent was blocked by rubble. Ground subsidence continued, however,

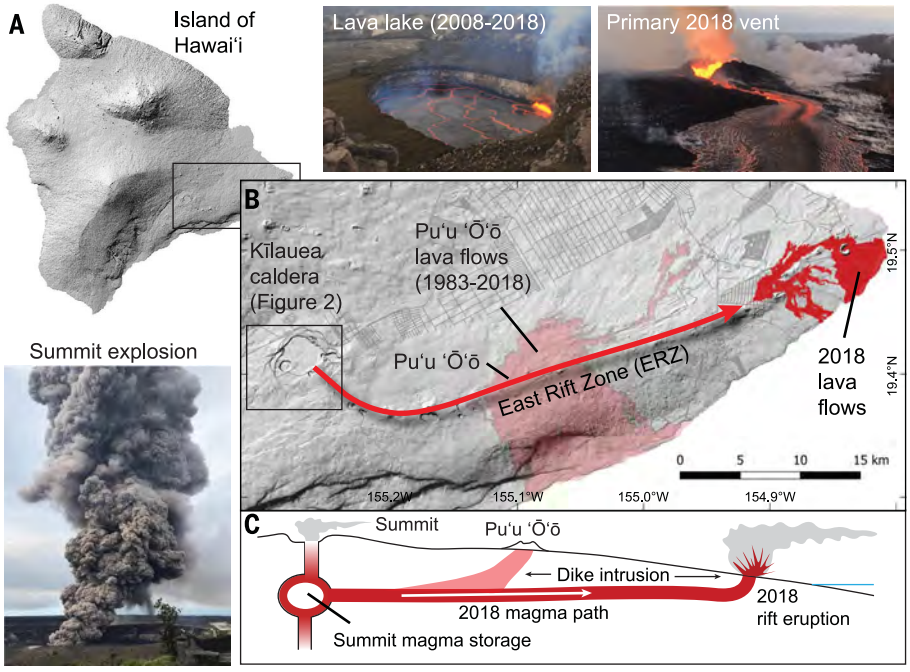

Fig. 1. Kīlauea Volcano and the 2018 eruption. Photos show a summit explosion on 9 May 2018, the lava lake as it appeared in April 2018, and the primary 2018 LERZ eruptive vent. (**A**) Shaded topographic map of the island of Hawai'i; the box shows the extent of the map in (B). (**B**) During the 2018 eruption, magma flowed >40 km underground subhorizontally from the summit (left) to the LERZ vents (right). See Fig. 2 for an enlargement of the summit area. (**C**) Schematic cross section (not to scale) showing flow of magma from the summit to the LERZ.

indicating ongoing depressurization, and HVO became concerned about failure of the rock above the reservoir. From 9 to 15 May, several $M \geq 3$ earthquakes per day shook the summit, and tremor [as indicated by the real-time seismic amplitude measurement (RSAM)] was recorded at very high levels. Ground cracks were observed near Halema'uma'u crater on 14 May, and by 16 May the GPS network had recorded total subsidence in that area of ~1 m.

On 16 May at 18:16 Hawaii Standard Time (HST), abrupt inflationary (radially outward) ground deformation and very-long-period (VLP) seismic energy (M_w 4.9) were recorded across the summit, an ashy gas plume rose to 20,000 ft, and summit RSAM dropped precipitously. Ground deformation and VLP observations were similar to those previously caused by rockfalls into the lava lake and ascribed to pressurization of the shallow magma system (*11*) but were much larger in amplitude. They were also similar to observations recorded during caldera collapses at Miyakejima (Japan) and Piton de la Fournaise (La Réunion) volcanoes (*12*–*15*). Eleven more of these events, informally termed "collapse/explosions" by HVO, occurred before the end of the month. Satellite observations and failure of instruments on the crater rim indicated that the (now empty) lava lake vent was growing more rapidly (Fig. 4) and beginning to cause failure outside of Halema'uma'u, but broader-scale, fault-bounded surface collapse was not yet detected. Summit SO_2 emission rates increased by two to three times (*7*), but erupted tephra volumes were much smaller than collapse volumes. Away from the widening vent, the summit continued to subside between collapses in a roughly circular pattern centered on the caldera.

The onset of broader-scale, clearly fault-bounded collapse outside of Halema'uma'u crater began in the early morning of 29 May with an abrupt down-dropping of the caldera floor around Halema'uma'u, approximately coincident with the onset of higher eruption rates (~150 m^3/s) in the LERZ. We measured 1.5 m of subsidence at a GPS station (NPIT) on the northeast rim of the crater during the seconds-long event, and visual observations from HVO revealed subsidence north-northeast and west of Halema'uma'u. Away from the subsiding block(s), however, inflationary radially outward deformation and VLP seismicity were observed that were similar to previous events in May but with much larger amplitudes (Fig. 4).

On 1 June, enabled by a marked reduction of Kīlauea's summit plume, an unoccupied aerial vehicle took the first clear photos of Halema'uma'u since mid-May. The photos showed major collapse and widening of the vent, ~30 m of subsidence of the western floor of Halema'uma'u, and faulting and subsidence of the 1500 CE caldera floor more than 1 km northwest of the former lava lake. As more collapses occurred through June, the surface expression and area of slumping expanded greatly. Collapse events were roughly periodic in time (Fig. 4A), preceded by marked increases in earthquake rate (*7*), and sometimes followed by surges in effusion rate at the LERZ vent ~40 km distant (*16*). The final collapse geometry was not fully established until mid- to late June, with clockwise propagation of a fault scarp through the center of the older 1500 CE caldera. By the time the new caldera stopped growing in early August, 62 collapses had occurred, producing as much as ~500 m of subsidence and a total collapse area of ~5 km^2.

Modeling lava lake and ground deformation data

Our goals were to estimate the subcaldera magma reservoir geometry; infer the conditions under which the reservoir's host rock began to fail; and evaluate how these parameters related to the style, location, and volume of subsequent caldera collapse. We used data from the period of near-constant high-rate subsidence after the M_w 6.9 earthquake and preceding the first collapse event on 16 May (Fig. 4), which we treated as the effective onset of caldera collapse. Observations suggest that during this time, rock at the summit responded elastically to changing stresses and slip on buried ring faults was minimal (*8*). We hypothesized that ground deformation and changes in lava lake surface height were generated by pressure change at constant rate $\dot{p}$ in a magma reservoir beneath Kīlauea's summit (*4*, *6*). We constructed a model that relates $\dot{p}$ to the rate of lava lake surface height change, assuming a magmastatic relationship, and to observed ground deformation velocities by using a continuum-mechanical model of a spheroidal magma reservoir embedded in an elastic half-space (Fig. 5) (*8*). The deformation model was implemented using the finite element method and then employed to construct a fast numerical surrogate suitable for Markov chain Monte Carlo (MCMC) estimation (*8*, *17*). Primary model parameters are shown in Fig. 5.

We performed a joint Bayesian parameter estimation using the lava lake withdrawal rate together with GPS, ground tilt, and InSAR velocities (*8*). We also used independent information from previous studies to constrain lava lake density and host rock rigidity, and we placed limits on the proximity of the top of the magma reservoir to the surface. We directly estimated reservoir location, geometry, and pressure change rate, and allowed "nuisance" parameters (including host rock shear

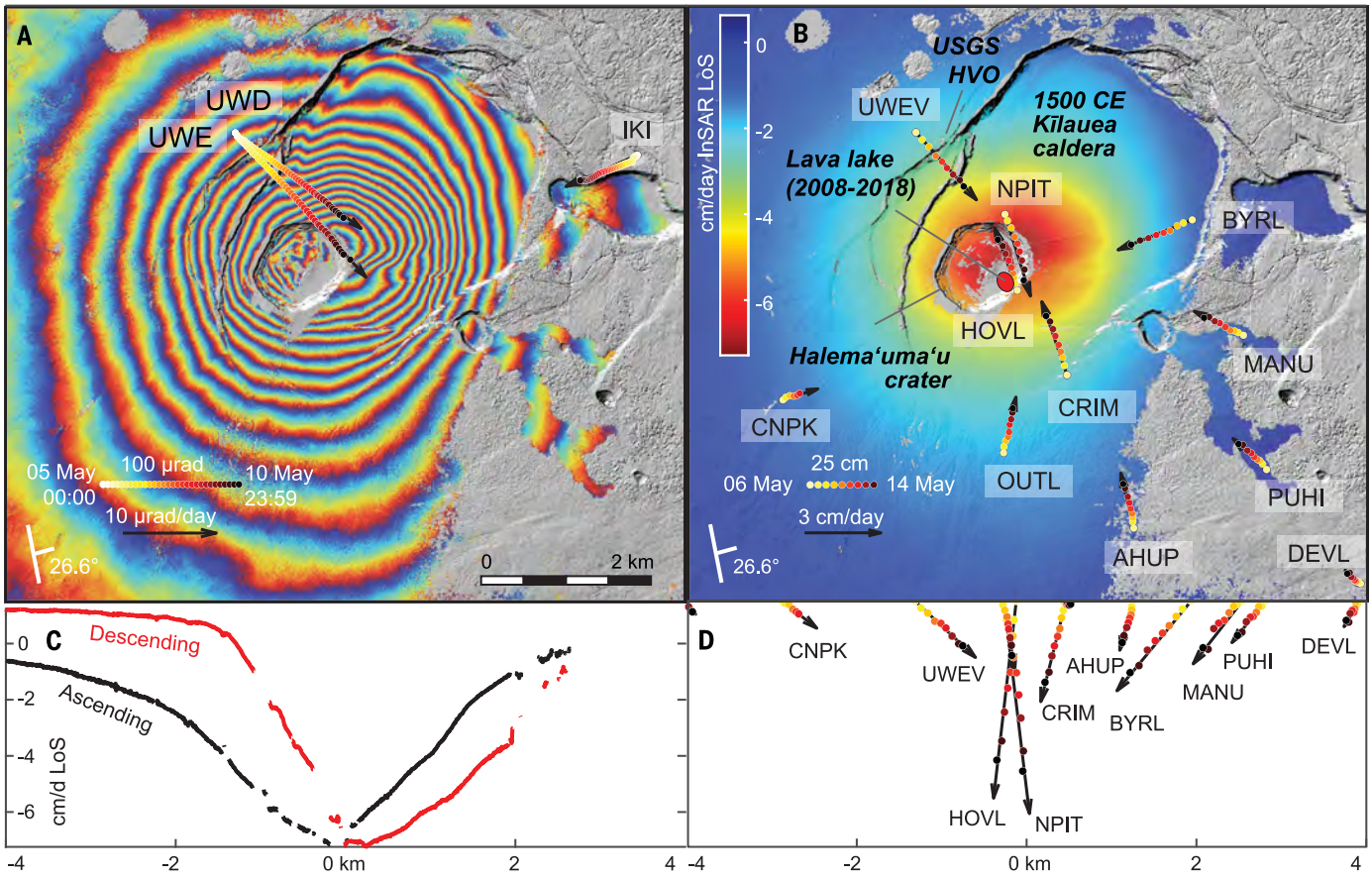

Fig. 2. Spatial pattern of subsidence at Kīlauea's summit in 2018. (**A**) Ground tilt overlaid on an ascending-mode COSMO-SkyMed interferogram spanning 6 to 10 May 2018 (table S1). Colored dots show observed tilt, and black arrows show best-fitting tilt velocities used for modeling. Each complete InSAR color fringe represents 1.55 cm of displacement in the look direction of the satellite (T symbol, 26.6° from vertical). Small-scale irregularities in the fringe pattern are evident in the caldera. Background shaded digital elevation model (DEM) shows Kīlauea's summit in 2009, similar to its appearance in April 2018. (**B**) Observed GPS displacements (colored dots) and best-fitting velocities (black arrows) overlaid on the unwrapped interferogram from (A). An active lava lake was nested within Halema'uma'u crater, itself nested in the larger 1500 CE Kīlauea caldera. LoS, line of sight. (**C**) West-east profiles of LoS COMSO-SkyMed InSAR velocities approximately through the center of Halema'uma'u crater. Profiles differ because of different look angles. (**D**) View of GPS data in (B), looking north.

modulus and magma density) to vary to account for their uncertainties. From the MCMC results and additional independent information we computed other parameters of interest, such as the rate of magma outflow from the reservoir. Parameter estimates take the form of probability density functions (PDFs), which account for uncertainties in data and prior information. We found that model output is consistent with the withdrawal rate of Kīlauea's lava lake and the first-order temporal and spatial pattern of ground deformation preceding caldera collapse (Fig. 6). We discuss our modeling results and implications throughout the following sections.

Location and geometry of subcaldera magma storage

Magma reservoir depth, volume, and geometry play a direct role in the onset, style, and duration of caldera collapse (*15*, *18*–*21*), but magma storage beneath most calderas is poorly understood and subject to controversy (*22*, *23*). Investigations at volcanoes that have hosted historic caldera-forming eruptions suggest that storage zones may be complex and occur over a range of depths (*3*, *24*–*28*). We found that geodetic data preceding caldera collapse at Kīlauea in 2018 are consistent with evacuation of magma from a storage reservoir centered at ~2 km depth just east of Halema'uma'u crater (Fig. 5 and table S2). The estimated magma reservoir is somewhat vertically elongated, as required to explain the observed ratio of vertical to horizontal displacements. The reservoir's depth implies an initial (pre-eruptive) magma pressure of ~45 MPa on the basis of the magmastatic lava lake relationship together with prior constraint on magma density (*8*). To the extent that magma density and lithostatic density were similar, the open lava lake vent precludes large magmatic overpressures before the onset of the eruption (*8*).

In the past two millennia, two long-lived, deep calderas have existed at the summit of Kīlauea: one from ~200 BCE to ~1000 CE, and the modern caldera, which formed in ~1500 CE and began refilling in ~1800 CE (*29*). Magma storage beneath Kīlauea's 1500 CE caldera was inferred in the first written records of the volcano nearly two centuries ago (*30*) and explains subsidence associated with rift zone intrusions and eruptions. At least two persistent magma reservoirs—the Halema'uma'u reservoir just east of Halem'uma'u crater and another at greater depth beneath the south part of the 1500 CE caldera—have been hypothesized on the basis of geodetic and other observations (*6*, *31*–*38*). Several transient storage zones may also have existed (*36*), and VLP seismic energy frequently emitted from a source ~1 km beneath the northeast rim of Halema'uma'u (*39*) has been interpreted as the intersection of north- and east-trending dikes (*11*, *40*). The geometries and relationships between these various magma storage regions have been difficult to interpret, and in some cases appear to change over time.

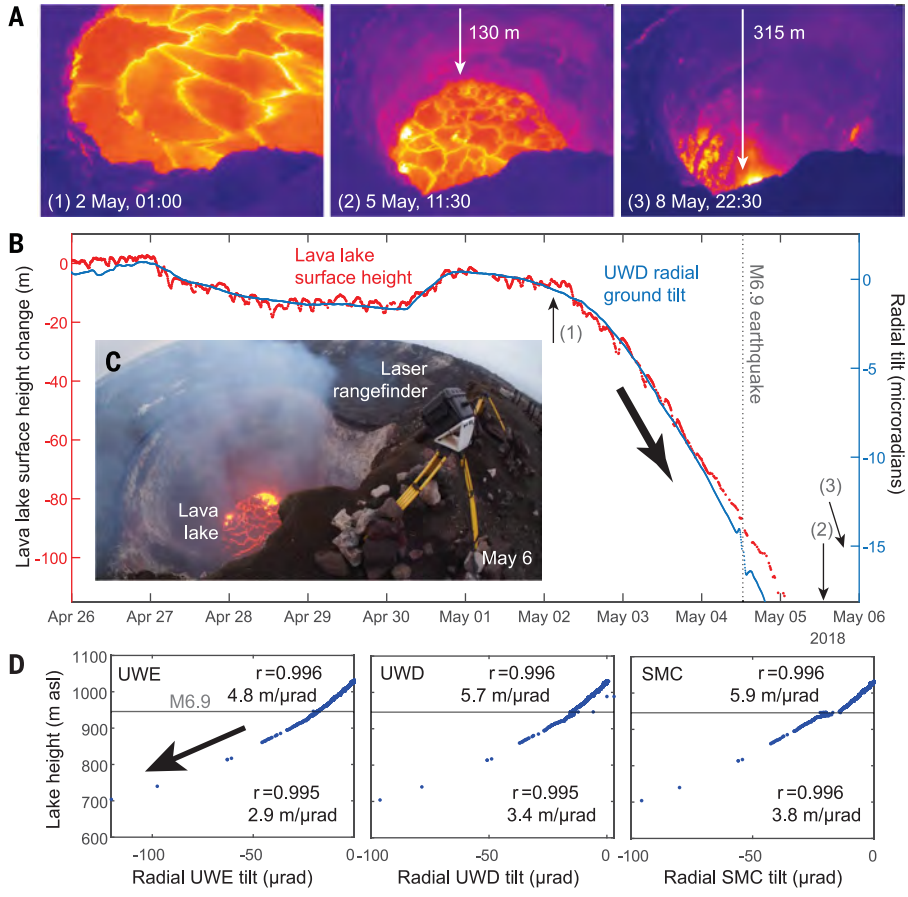

Fig. 3. Withdrawal of Kīlauea's lava lake in early May. (**A**) Thermal images of the lava lake surface taken from the south rim of Halema'uma'u crater while the lake was draining. (**B**) Time series of change in lava lake surface height relative to 26 April, and radially outward low-pass–filtered ground tilt at UWD. Time series after 5 May are shown in Fig. 4. Numbers correspond to acquisition times of images in (A). (**C**) Photograph showing the lava lake on 6 May and the laser rangefinder used to measure its surface height. (**D**) Relationship between lava lake surface height and radially outward tilt (with M_w 6.9 earthquake offset approximately removed). At all stations, the ratio decreased by ~40% around the time of the M_w 6.9 earthquake, denoted by the horizontal gray line. Correlation coefficients are denoted by r.

The reservoir location and geometry we estimate here lead us to conclude that magma withdrawal from the Halema'uma'u reservoir was responsible for observed ground subsidence in 2018.

Misfits between model predictions and geodetic data provide additional insight into magma storage (Fig. 6). Our model closely fits lava lake withdrawal rate data but cannot account for small-scale features observed in the InSAR data (fig. S7), nor can it explain the very-high-quality GPS data to within formal uncertainties. Material heterogeneity such as preexisting faults and altered rocks, localized shallow magma storage, or irregularities in the top of the reservoir itself may be responsible for these features [we scale data uncertainties to account for these limitations (*8*)]. The model also inadequately accounts for subsidence observed south of the caldera. This likely reflects the early stages of magma drainage from Kīlauea's deeper and more enigmatic south caldera reservoir. Ground deformation believed to be due to magma evacuation from this reservoir increased in cumulative magnitude and spatial extent through June and July and continued after the cessation of the eruption (presumably as magma drained to refill the ERZ). However, most of the deformation during our modeled time period can be attributed to the Halema'uma'u reservoir (predicted deformation from the model reduces variance in modeled InSAR scenes by 93 to 96%).

Volume of magma storage

The volume of magma stored beneath a volcano exerts a primary control on nearly all aspects of volcanic activity, including limiting the size of an eruption and any possible caldera collapse. Yet, magma storage volumes are very poorly known at almost all of Earth's volcanoes. Intensive study at Kīlauea over previous years has yielded estimates for the Halema'uma'u reservoir varying over two orders of magnitude [from 0.2 to >20 km^3 (*6*, *34*, *41*–*44*)].

In general, geodetic data can be used to resolve the quantity $V\dot{p}/\mu$ for a magma reservoir, where V is reservoir volume, $\dot{p}$ is pressure change rate, and μ is host rock shear modulus, but not these terms independently (*45*). Our parameter estimation resolved V by using constraints on $\dot{p}$ from the lava lake data (below) and on μ from previous studies (*6*, *41*). Because $\dot{p}$ is much more tightly constrained than μ, we were able to resolve the ratio $V/\mu \cong 1.3 \pm 0.15\ m^3/Pa$ (*8*) (fig. S16). This implies that reservoir volume should be of the same order as the rigidity of the host rock. The combination of spatially dense geodetic data with the finite-source model used in our study provided additional constraint on reservoir volume (*45*), and the maximum size of the reservoir was geometrically limited by its depth and shape (both resolved geodetically).

We found that 2.5 to 7.2 km^3 of magma (at 68% credible bounds) was stored beneath the summit of the volcano in the Halema'uma'u reservoir at the beginning of May 2018. The upper bound should be considered only approximate; volumes of 10 km^3 or even larger cannot strictly be ruled out by the data, particularly if we relax a priori limits on the presence of magma storage at very shallow depths (<750 m) (*8*). On the other hand, volumes of <1 km^3 are improbable, because smaller reservoirs cannot explain the high rate of observed ground deformation without requiring an unreasonably weak host rock (pressure change rate is tightly constrained by the lava lake data). Precollapse storage volumes for other basaltic calderas are not well known, but our calculated volume is far smaller than that of reservoirs inferred to have supplied large silicic caldera-forming eruptions.

Rate of magma depressurization and drainage

Reservoir pressure change rate $\dot{p}$ is constrained in our parameter estimation by the observed rate of lava lake withdrawal, the prior distribution on lava lake density, and the magmastatic assumption (*8*). Thus, $\dot{p}$ is insensitive to geodetic data and modeling. We estimated that pressure in the reservoir decreased at 1.25 ± 0.09 MPa/day (Fig. 5B) after the M_w 6.9 earthquake. At this rate, pressure at the reservoir's centroid would have decreased to atmospheric (an impossibility) by early June. Continuation of the eruption at a high rate for 3 months therefore required an increase of reservoir pressure through collapse of the overlying rock. This mechanism is also consistent with surges in effusion rate after collapses later in the eruption (*16*).

The volumetric rate of contraction $\dot{V}$ of the magma reservoir and the volumetric rate q

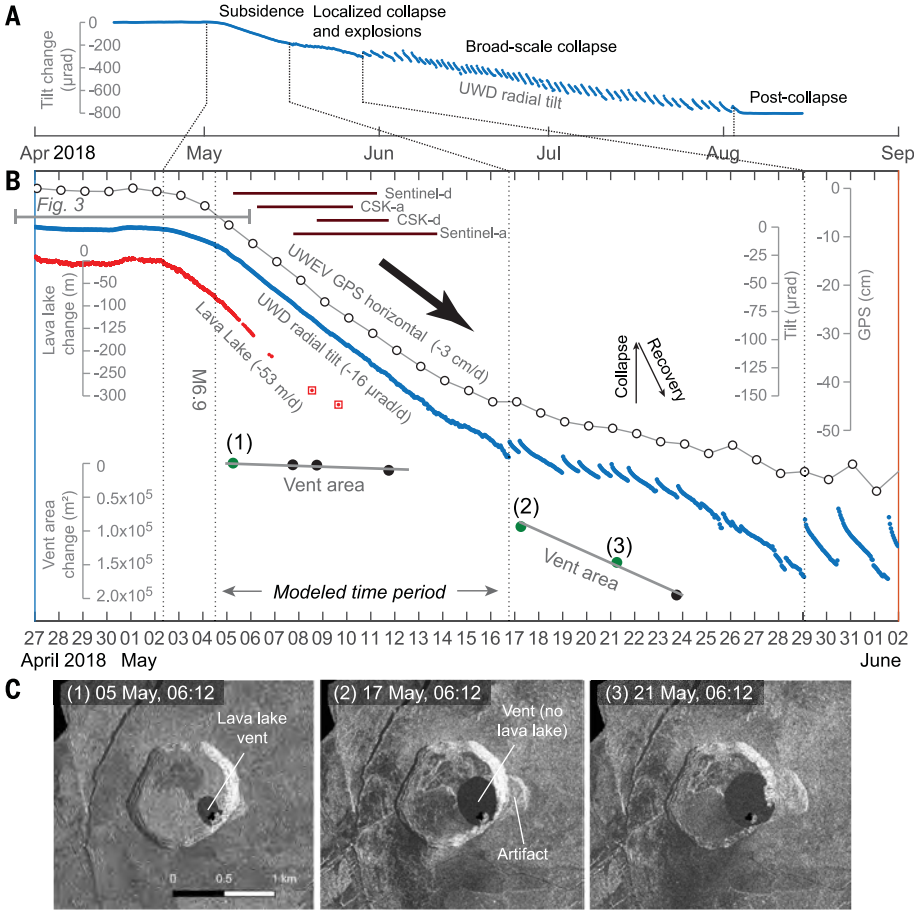

Fig. 4. Temporal evolution of summit deflation. (**A**) Radial ground tilt at UWD over the full eruption. Positive tilt is consistent with reservoir inflation (pressurization) and negative tilt with deflation. Collapses appear as small sawteeth from 16 to 26 May (nearly invisible at this scale) and as much larger sawteeth during broad-scale collapse (29 May and after). Time series were corrected for certain tectonic offsets. (**B**) GPS, tilt, lava lake surface height, and vent area time series indicating summit deflation from late April to early June 2018. Stations UWD (tilt) and UWEV (GPS) are approximately colocated (see Fig. 2 for station locations). Lava lake points with boxes were derived from structure-from-motion photogrammetry and are more uncertain. Vent area was inferred from satellite radar (ascending mode in green and descending mode in black) amplitude images as shown in (C); numbers on the time series correspond to these images. Time spans of modeled InSAR data are shown as horizontal bars and denoted with "-a" for ascending mode and "-d" for descending mode. The gray horizontal bar indicates the time span shown in Fig. 3. CSK, COSMO-SkyMed. (**C**) CSK radar amplitude images showing enlargement of the summit vent. Brighter pixels indicate higher radar reflectivity, so the vent appears black.

at which magma exited the reservoir are important to the timing of caldera collapse and the dynamics of summit draining and its relation with processes in the ERZ (*19*, *21*). We computed $\dot{V} = -1.3 \times 10^6 \pm 0.1$ m^3/day (~15 m^3/s) using estimated model parameters together with a numerical model for the elastic compressibility of the magma reservoir (*8*). This estimate is tightly constrained by the geodetic data. Combined with our posterior distribution for $\dot{p}$, we found that each pascal of pressure reduction in the reservoir reduced its volume by ~1 m^3 (dV/dp = 1.0 ± 0.1 m^3/Pa). Because of the rigidity of the host rock, the reservoir itself was contracting at only ~0.03% per day while its internal centroid pressure was decreasing at ~3% per day. At shallower depths in the reservoir, the relative pressure change rate would have been even greater.

Because magma is compressible, the rate at which the reservoir contracted was likely not equal to the rate of magma withdrawal. Using our distribution for $\dot{V}$ and independent constraint on compressibility (*8*), we estimated a net magma outflow rate q from the Halema'uma'u reservoir of 2.3 million to 5.4 million m^3/day (27 to 62 m^3/s) at 68% credible bounds. This rate exceeds the average supply to Kīlauea from the mantle by an order of magnitude (*37*, *46*, *47*) and thus should approximate the total rate of flow to the ERZ from the contracting reservoir. Adding another ~5 to 10 m^3/s from the draining lava lake and its feeder conduit (*8*) yields a combined outflow rate of ~35 to 70 m^3/s from the lava lake and Halema'uma'u reservoir. This is much higher than the time-averaged eruption rate from 3 to 18 May (7 m^3/s) (*48*), indicating that summit magma was entering the rift without erupting in order to feed deflation of the middle ERZ and growth of the LERZ intrusion. By June, after the onset of collapse events, LERZ eruption rates had increased by at least an order of magnitude (*7*), and the time-averaged rate of caldera collapse was ~two to five times larger than our estimated magma outflow rate. These observations strongly suggest a large increase in magma withdrawal rate from the summit in association with caldera collapse.

Reservoir failure thresholds

Placing bounds on the thresholds at which magma reservoirs begin to fail is important for determining the collapse hazard of an ongoing eruption (*49*), interpreting the geological record, and understanding the mechanical processes that lead to caldera collapse. Reservoir failure is triggered by stresses imparted to the host rock by changes in internal pressure. Kīlauea's lava lake provided a window into changing magma system pressure but disappeared from view ~1 week before the first collapse event. However, by assuming that pressure continued to decrease at rate $\dot{p}$ between the end of the modeled time period (14 May) and the first collapse (16 May), as suggested to first order by geodetic data, we estimated a pressure change at failure Δp_f = −17.2 ± 1.1 MPa (*8*).

We also used tilt data as a direct empirical proxy for pressure change, using the scaling relationship established while the lava lake was active (at UWD, 0.078 ± 0.006 MPa per microradian of radial tilt). This approach does not rely on any model except for the magmastatic relationship used to establish the scaling ratio, nor does it require an assumption of constant rates, but it can be affected by ground deformation caused by processes other than reservoir pressure change. We used this approach to estimate pressure changes after 16 May under the assumption that ground tilt during collapse events was caused entirely by changes in reservoir pressure [this likely overestimates pressure changes somewhat owing to faulting processes (*50*)]. With this approach, we obtained pressure changes of ~17.8 and ~25.0 MPa immediately before the first collapse event on 16 May (similar to the model-based results) and the first broad-scale collapse on 29 May, respectively (Fig. 7 and fig. S10) (*8*). These estimates

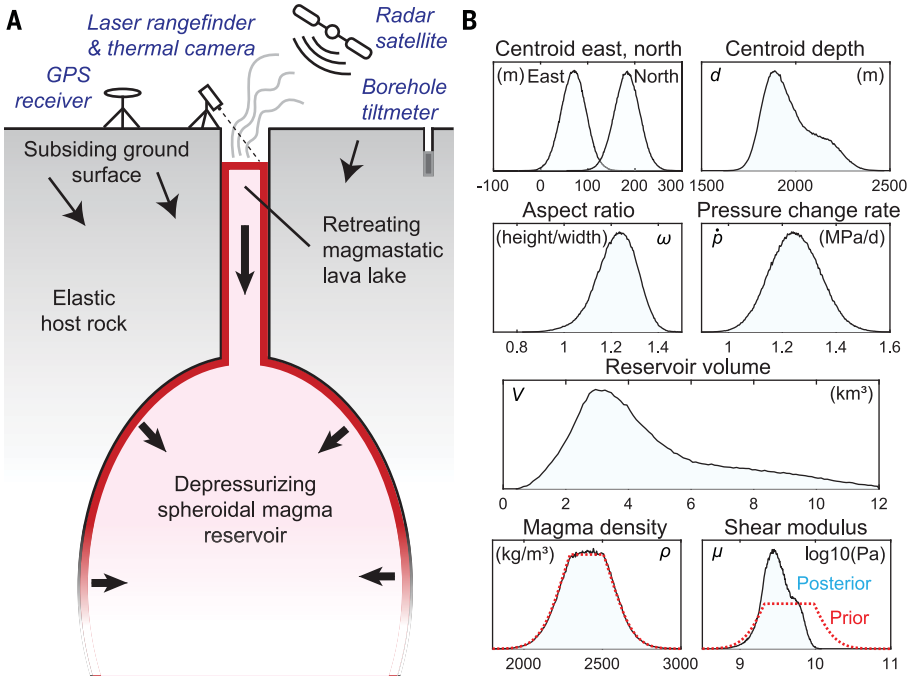

Fig. 5. Model geometry and estimated parameters. (**A**) Conceptual model geometry including instruments that recorded observations used in this study. The reservoir centroid is shown for simplicity directly beneath the lava lake, but this is not required in our model. (**B**) Marginal posterior PDFs of primary estimated model parameters (*8*), excluding "nuisance" parameters associated with data uncertainties (fig. S17). East and north positions are relative to 19.4073°N, 155.2784°W (the east rim of precollapse Halema'uma'u crater), and depth is approximately relative to the volcano's summit.

imply a relative pressure reduction exceeding 30% at the reservoir's centroid by 16 May. They can also be related to shear stresses in the host rock, although the conditions required to trigger failure are complex and poorly understood. Using simple geometrical arguments, we computed the shear stress that the deflating reservoir imparted to an overlying cylindrical ring fault and estimated a stress change of between ~8 and 13 MPa (*8*, *18*).

Although it is pressure changes that trigger collapse, due to the lack of observations at natural systems failure criteria are more typically formulated in terms of volume changes. Reservoir volume change may be tracked nearly in real-time using geodetic data, and erupted volume may be tracked directly or with geophysical observations. We defined critical fractions $V_{crit} = -\Delta V_f / V$ and $f_{crit} = -\Delta q_f / V$ (*19*), where ΔV_f and Δq_f are the reservoir volume change and total magma extraction volume at the time of failure, respectively. To estimate ΔV_f, we scaled the model-based estimate of Δp_f at the first collapse by the ratio dV/dp obtained from the Bayesian estimation results. Because $dV/dp \approx 1$, the magnitudes of pressure and volume changes were comparable. Scaling by reservoir volume yielded V_{crit} = 0.27 to 0.66%, and further scaling by system compressibility yielded f_{crit} = 0.68 to 2.2%, both at 68% credible bounds (table S2). At 95% confidence, we concluded that <3.5% of magma was evacuated before the onset of collapse at Kīlauea.

Geometry of the roof block

The aspect ratio of the roof block above a magma reservoir (Fig. 8, C and D) influences not only the timing of collapse onset but also its subsequent structural development and style (*20*, *51*, *52*). In general, low-aspect roof blocks [$R_a < 1$, where R_a is the thickness T of the crust above the magma reservoir divided by the reservoir diameter D (*52*)] tend to favor a central coherent collapse "piston" bounded by reverse faults, whereas high-aspect ($R_a > 1$) blocks favor incoherent subsidence through migration of fractures upward from the reservoir. However, observational constraints on R_a from real-world caldera collapses are limited, owing to poor knowledge of the geometry of subcaldera magma reservoirs. Caldera diameter must generally be used as a proxy for reservoir diameter and roof thickness inferred roughly from geological or geophysical data (*18*, *19*, *53*, *54*).

The set of finite-source geodetic models derived from our MCMC analysis allowed us to estimate R_a. Taking T to be the distance between the surface and the top depth of each magma reservoir in the posterior probability distribution, we found that the roof block at Kīlauea was thin and wide, with $R_a \approx$ 0.4 (Fig. 8). R_a would be smaller if we were to relax our minimum reservoir top depth (*8*) but would be larger if we measured height from a point other than its very top. Small reservoirs from our probability distribution yield aspect ratios closer to 1, but in general $R_a > 1$ appears unlikely.

Reservoir evacuation and the end of the eruption

It is often assumed that caldera-forming eruptions are terminated by the near-complete evacuation of their source reservoirs (*3*, *49*, *54*, *55*), as suggested by some models (*56*) and perhaps indicated by long repose periods after some collapses (*55*). This hypothesis has implications for hazards during ongoing eruptions. It also allows for interpreting data from past events because it implies that erupted volume is approximately equal to reservoir volume. Although there is evidence that this assumption may not be valid (*20*, *56*), it has been difficult to evaluate because of limited knowledge of subcaldera magma reservoir volumes.

Taking the total 2018 summit collapse volume (*7*) as a proxy for the total volume change of the shallow reservoir during the eruption, we used our posterior PDF for reservoir volume to estimate that only 11 to 33% of Kīlauea's shallow magma reservoir was evacuated by the end of the eruption. The probability of complete drainage is very small; we estimated <5% probability that even half of the reservoir was drained (Fig. 8). This inference is consistent with the relative constancy of collapse-related geophysical signals from June to August (*7*), which might have changed in character if the reservoir had neared complete evacuation, and also with the post-eruptive return of episodic days-long ground deformation cycles at the summit, which are believed to be caused by pressure perturbations in the shallow magma reservoir (*6*). Our results suggest caution in assuming that magma reservoirs (at least basaltic ones) fully evacuate during caldera-forming eruptions.

Discussion

Caldera collapse at Kīlauea in 2018 was caused by high-rate magma evacuation from a roughly equant storage zone of several cubic kilometers at shallow depth (~2 km), centered just east of the former Halema'uma'u crater. Many previous studies have inferred magma storage in this area, but 2018 data provide new insights. Our simple geodetic model cannot account for magma withdrawal from other reservoirs or the fine-scale topology of magma storage [for instance, we likely cannot rule out magma stored in a broad plexus of interconnected magma-filled cracks (*57*) with similar magma volume], but it well explains the observed overall spatial pattern of ground deformation. Likewise, the rate of magma system depressurization estimated by our model can

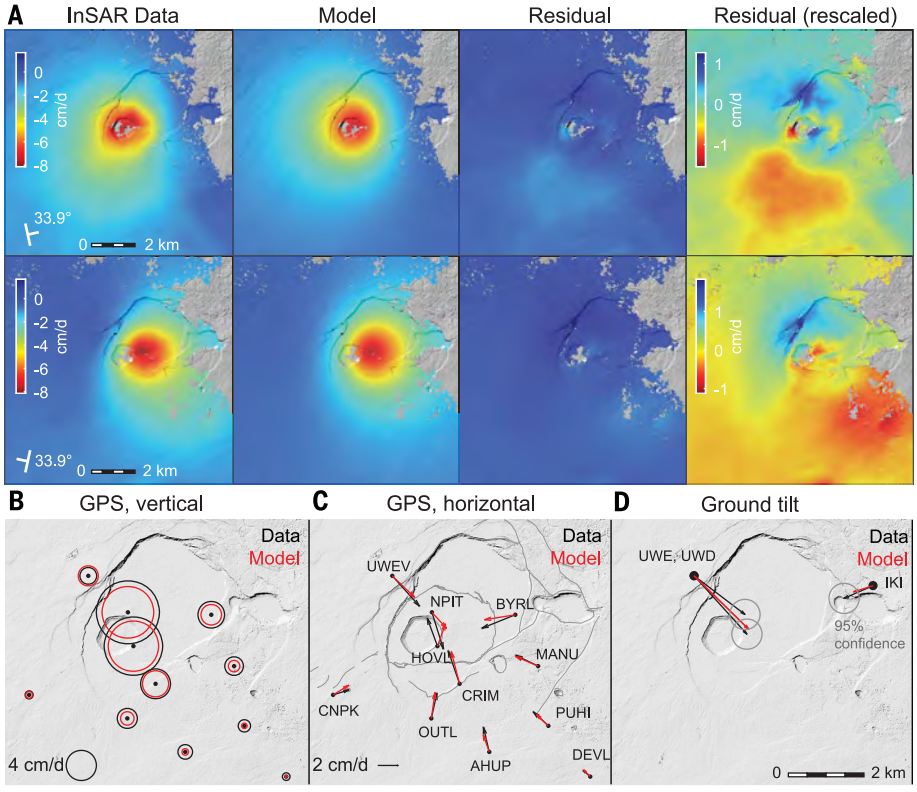

Fig. 6. Fit of model to observations. Shown are predictions from the mean of the posterior distribution. We do not show lava lake data, which the model is able to fit "exactly" (to within an arbitrary precision). (**A**) Sentinel-1 ascending- and descending-mode interferograms (see fig. S15 for COSMO-SkyMed). The variance of the InSAR data is reduced by more than 95% after subtracting model predictions. Residuals in and south of the caldera do remain (the images in the rightmost column have a different color scale to highlight these effects). (**B**) Vertical GPS velocities. (**C**) Horizontal GPS velocities. Formal 95% data uncertainty ellipses are shown but are too small to be easily visible; in the estimation, these uncertainties are scaled using data-weighting hyperparameters (*8*). (**D**) Ground tilt rates.

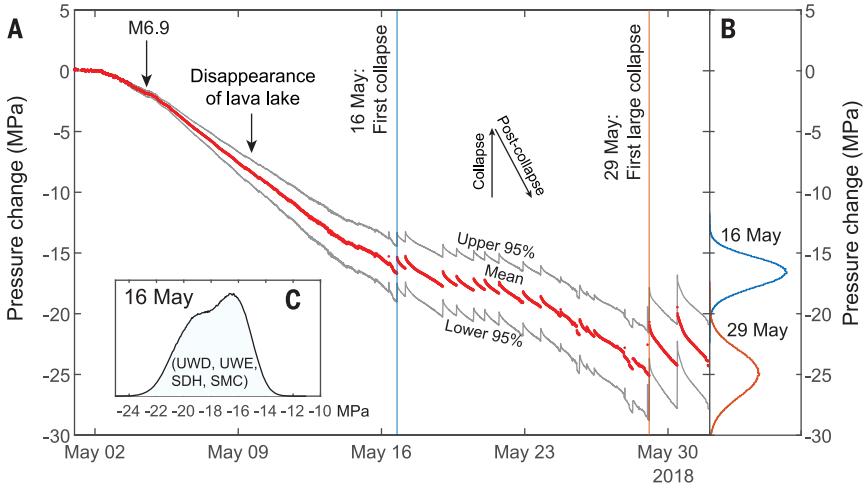

Fig. 7. Pressure change in the magma reservoir. (**A**) Time series of reservoir pressure change derived from scaled tilt at UWD. The time span is similar to that in Fig. 4. Uncertainties are due to lava lake density and the lake-tilt ratio (Fig. 3). Certain offsets not apparently related to magmatic processes were removed from UWD tilt data. (**B**) Marginal distributions for pressure change immediately preceding the first collapse (16 May) and the first large collapse (29 May). We combined marginal distributions for tiltmeters UWD, UWE, SDH, and SMC to produce the distribution in (**C**).

explain the observed rate of lava lake withdrawal and ground deformation.

When did caldera collapse begin? Seismicity after the M_w 6.9 earthquake might have indicated the early stages of caldera-fault propagation at depth (*58*), but there appeared to be relatively little effect on surface deformation during the first half of May (*8*), and there was no geophysical evidence for collapse of rock into the deeper magmatic system. Quasi-periodic VLP seismic and geodetic signals recorded from 16 to 26 May were associated with vent widening, volume loss, and ejection of ash, but not surface faulting over a broad area. Yet, InSAR data from this time showed a more complex deformation pattern in the caldera than that present earlier in the month, suggestive of the early-stage surface expression of slip on buried caldera faults. Furthermore, geophysical signals were similar to those recorded during caldera collapses at other volcanoes and at Kīlauea after 29 May, when broadscale collapse was visually observed. Thus, the events of 16 to 26 May were evidently related to collapse of rock into the magmatic system, although the extent to which these collapses occurred into the lava lake feeder conduit and/or shallow dike-like storage bodies, as opposed to the Halema'uma'u reservoir, remains an open question. Also unclear is the extent to which any propagation of buried caldera faults during this time related to geophysical observations. Nonetheless, we conclude that caldera collapse effectively began on 16 May, accelerated and enlarged on 29 May (when we were able to closely tie visual observations of broader-scale collapse to geophysical signals), and did not reach its full surface expression until late June.

The critical thresholds required for caldera collapse are thought to be controlled by many factors, including the shape (aspect ratio) of the roof rock above the reservoir (*18*, *19*); exsolved magmatic volatiles, which buffer pressure drop due to magma extraction (*56*, *59*, *60*); and preexisting faults and weaknesses (*49*). At Kīlauea, the 2018 collapse occurred within an older, larger caldera and, in some areas, appeared to proceed along preexisting faults. We speculate that both the empty lava lake vent and the relatively thin and wide roof block might have promoted failure (*18*, *19*). It is also possible that, at shallow depths, the retreating magma surface could have encountered a flared conduit geometry, leading to instability. An open question is how critical failure thresholds might differ between small nested-caldera basaltic systems, such as Kīlauea, and large silicic systems.

Caldera collapse began at Kīlauea after the elastic reservoir had contracted only very slightly (V_{crit} < 1.1%), caused by withdrawal of only a very small fraction of its stored magma

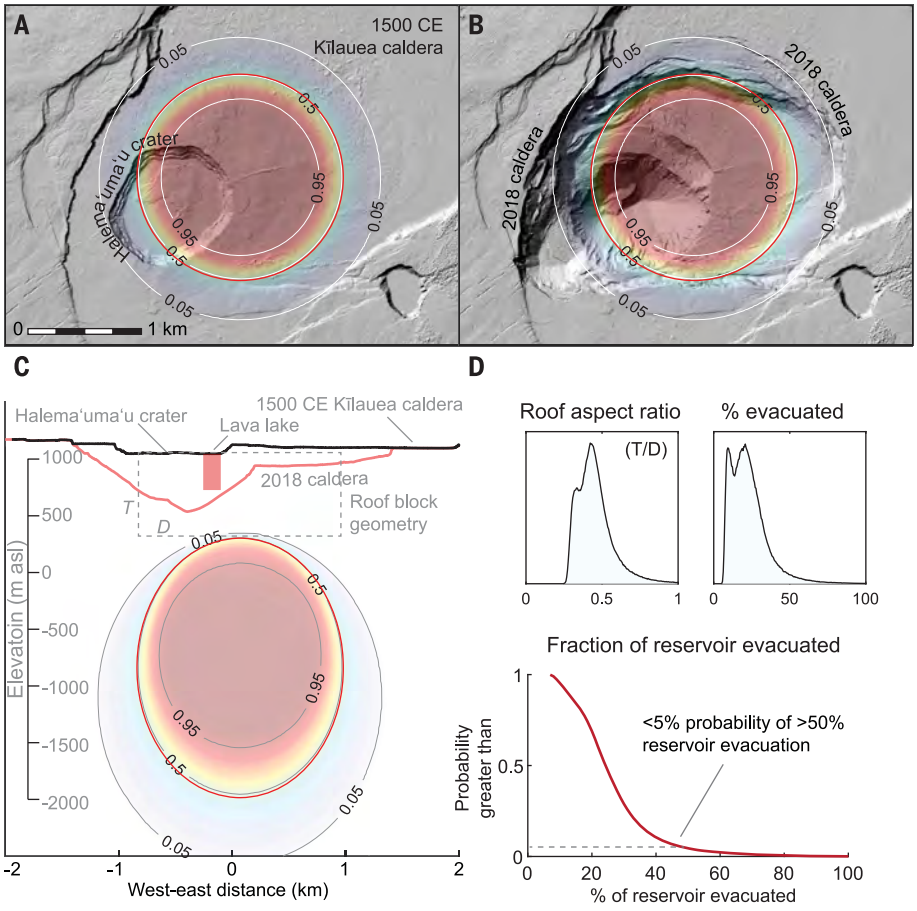

Fig. 8. Probabilistic magma storage in the Halema'uma'u reservoir beneath Kīlauea's summit. Contours and shading indicate estimated probability of magma storage based on the range of model geometries inferred in the parameter estimation (*8*). (**A** and **B**) Results for a horizontal slice near the reservoir centroid at 2 km depth. (**C**) Probability along an east-west slice at the reservoir centroid. Model depths are converted to vertical elevations using the approximate mean geodetic observation elevation [1100 m above sea level (asl)]. Colors indicate relative probability (red, more likely; blue and white, less likely). Red circles show geometry predicted by the median of the posterior distribution. Shaded DEMs in (A) and (B) show the summit as it appeared before and after the 2018 caldera collapse, respectively. The dashed rectangle above the storage zone in (C) shows the rough geometry of the roof block. The bulk of magma was stored below sea level and the subaerial ERZ vents (Fig. 1). (**D**) Posterior PDFs of roof aspect ratio and the probability of complete reservoir evacuation given the observed caldera collapse volume, along with complementary cumulative distribution.

(f_{crit} < 4%). Geological observations and models have suggested that f_{crit} may range from <10% to >90% (*18*, *19*), but direct evidence has been lacking (note that many studies do not distinguish between V_{crit} and f_{crit}, which are equal only if magma is incompressible). Geophysical observations from basaltic collapses at Piton de la Fournaise, Fernandina (Galápagos), Miyakejima, and Bárðarbunga volcanoes yielded f_{crit} of ~8 to 20%, in some cases much lower than values suggested by analog models (*3*, *49*) but still much higher than we found for Kīlauea. Although it is possible that collapse began unusually quickly at Kīlauea, these previous estimates had to rely on assumptions that the volumes of initial collapse events were comparable to precollapse magma withdrawal volumes and that eruptions completely drained their magma reservoirs (*3*, *49*, *54*). As we have shown here, these assumptions are not always valid and could lead to a substantial overestimation of f_{crit}. These discrepancies indicate that calderas may fail more quickly than previously understood.

Although it is changes in magma pressure that drive host rock failure and caldera collapse, robust estimates of precollapse pressure changes have previously been unavailable. Magma extraction volumes are far more readily measured in nature but are only relevant to collapse to the extent that they influence reservoir pressure (an effect modulated by the compressibility of magma in the reservoir). Data from Kīlauea allowed us to move beyond reliance on f_{crit} and directly estimate precollapse pressure change. Knowledge of the pressure change makes it possible to compute stress changes on the roof block and thus tie the observations to the failure process.

Once failure began, episodic roof block collapse transferred the load of the overlying rock to the magma, increasing its pressure. This process may explain similar episodic geophysical observations at other basaltic caldera collapses (*14*, *15*, *61*). By using ground tilt as a proxy for reservoir pressure change, we estimated that inflationary deformation during the first collapse event on 16 May was caused by a pressure increase of ~1.3 MPa in the reservoir, only a fraction of the preceding deflation. Because reservoir pressure was likely near lithostatic at the onset of the eruption, this result indicates incomplete repressurization of the reservoir after the onset of collapse and implies residual frictional strength on the walls of the collapsing block(s) such that the weight of the roof was not entirely supported by the magma. This finding stands in contrast to assumptions that roof collapses reestablish lithostatic pressure in the reservoir (*56*, *59*) but supports the results of some numerical models (*62*).

The surface expression of caldera collapse was complex, asymmetric, and evolving, consisting of funnel-like gravitational failure into the evacuated lava lake vent and piston-like slumping of coherent blocks as large as ~150 ha, in some cases clearly bounded by preexisting faults. Taken as a whole, these events were consistent with collapse of roof rock into a shallow reservoir, governed not only by the aspect ratio of the roof but also by preexisting caldera faults and structural weaknesses, and possibly shallow unmodeled magma storage [e.g., (*11*, *63*)]. These observations are consistent with geological investigations and numerical experiments that demonstrate the complex diversity of collapse styles that can occur during caldera formation (*51*, *64*).

The location and lateral extent of magma storage inferred from our model are similar to the final geometry of the 2018 caldera collapse (Fig. 8). To first order, the relationship between the range of plausible reservoir geometries and observed caldera dimensions favors primary collapse faults ranging from near-vertical to inward dipping. Results indicate that the shallow subcaldera magma storage system spanned only a portion of the caldera in existence from 1500 CE to the present. The larger magma storage body required to explain the 1500 CE collapse may have been partially destroyed then or in a subsequent event (such as a large collapse that occurred at the volcano in 1868) or may

have involved failure of deeper parts of the summit magma system.

Globally, lava lakes are rare. Where they do exist, close observation during magma draining events may bear rich dividends, particularly if relayed in real time. Some of the data used in this study were evaluated in rapid-response mode internally by the USGS during the eruption with a preliminary form of our model. Resulting parameter estimates were used to better understand the possible course of the eruption and guided our thinking about hazards as the eruption progressed, highlighting the importance of near–real-time data and modeling capabilities at the world's volcano observatories.

Outlook

Despite insights into volcanic calderas afforded over the past two decades by well-documented collapses at Miyakejima, Piton de la Fournaise, and Bárðarbunga volcanoes, the conditions that trigger the onset of collapse remain only poorly understood. Draining of Kīlauea's summit lava lake in 2018 yielded a window into changing pressure in the volcano's shallow magma reservoir. We tracked the evolution of the magmatic system as it underwent steady high-rate elastic decompression due to magma withdrawal, followed by episodic fault-bounded caldera collapse. We were able to quantify the changing pressure in the reservoir, which, together with geodetic data, made it possible to estimate the volume of magma storage and the critical thresholds that preceded the onset of collapse. Caldera collapse began due to a relatively large decrease in the magma reservoir's internal pressure caused by withdrawal of only a small fraction of stored magma. Episodic fault-bounded subsidence of the roof block above the reservoir increased magma pressure, sustaining the flow of magma and thus representing a critical turning point in the evolution of the eruption.

REFERENCES AND NOTES

1. H. Williams, in *Bulletin of the Department of Geological Sciences*, G. D. Louderback, C. A. Anderson, C. L. Camp, R. W. Chaney, H. Williams, Eds. (Univ. of California Publications, ed. 25, 1941), pp. 239–346.
2. A. Geyer, J. Martí, The new worldwide collapse caldera database (CCDB): A tool for studying and understanding caldera processes. *J. Volcanol. Geotherm. Res.* **175**, 334–354 (2008). doi: 10.1016/j.jvolgeores.2008.03.017
3. M. T. Gudmundsson *et al*., Gradual caldera collapse at Bárdarbunga volcano, Iceland, regulated by lateral magma outflow. *Science* **353**, aaf8988 (2016). doi: 10.1126/science.aaf8988; pmid: 27418515
4. M. R. Patrick, K. R. Anderson, M. P. Poland, T. R. Orr, D. A. Swanson, Lava lake level as a gauge of magma reservoir pressure and eruptive hazard. *Geology* **43**, 831–834 (2015). doi: 10.1130/G36896.1
5. M. Patrick, D. Swanson, T. Orr, A review of controls on lava lake level: Insights from Halema'uma'u Crater, Kīlauea Volcano. *Bull. Volcanol.* **81**, 13 (2019). doi: 10.1007/s00445-019-1268-y
6. K. R. Anderson, M. P. Poland, J. H. Johnson, A. Miklius, "Episodic deflation-inflation events at Kīlauea Volcano and implications for the shallow magma system," chapter 11 in *Hawaiian Volcanism: From Source to Surface*, R. J. Carey, M. P. Poland, V. Cayol, D. Weis, Eds. (AGU Geophysical Monograph Series vol. 208, AGU, 2015), pp. 229–250; doi: 10.1002/9781118872079.ch11.
7. C. A. Neal *et al*., The 2018 rift eruption and summit collapse of Kīlauea Volcano. *Science* **363**, 367–374 (2019). doi: 10.1126/science.aav7046; pmid: 30538164
8. Materials and methods are available as supplementary materials.
9. M. R. Patrick, E. F. Younger, W. Tollett, Lava level and crater geometry data during the 2018 lava lake draining at Kilauea Volcano, Hawaii, ScienceBase (2019). doi: 10.5066/P9MJY24N
10. H. L. Kehoe, E. D. Kiser, P. G. Okubo, The rupture process of the 2018 Mw 6.9 Hawai'i earthquake as imaged by a genetic algorithm-based back-projection technique. *Geophys. Res. Lett.* **46**, 2467–2474 (2019). doi: 10.1029/2018GL080397
11. P. Dawson, B. Chouet, Characterization of very-long-period seismicity accompanying summit activity at Kīlauea Volcano, Hawai'i: 2007–2013. *J. Volcanol. Geotherm. Res.* **278–279**, 59–85 (2014). doi: 10.1016/j.jvolgeores.2014.04.010
12. H. Munekane, J. Oikawa, T. Kobayashi, Mechanisms of step-like tilt changes and very long period seismic signals during the 2000 Miyakejima eruption: Insights from kinematic GPS. *J. Geophys. Res.* **121**, 2932–2946 (2016). doi: 10.1002/2016JB012795
13. T. Staudacher *et al*., The April 2007 eruption and the Dolomieu crater collapse, two major events at Piton de la Fournaise (La Réunion Island, Indian Ocean). *J. Volcanol. Geotherm. Res.* **184**, 126–137 (2009). doi: 10.1016/j.jvolgeores.2008.11.005
14. L. Michon, N. Villeneuve, T. Catry, O. Merle, How summit calderas collapse on basaltic volcanoes: New insights from the April 2007 caldera collapse of Piton de la Fournaise volcano. *J. Volcanol. Geotherm. Res.* **184**, 138–151 (2009). doi: 10.1016/j.jvolgeores.2008.11.003
15. H. Kumagai *et al*., Very-long-period seismic signals and caldera formation at Miyake Island, Japan. *Science* **293**, 687–690 (2001). doi: 10.1126/science.1062136; pmid: 11474109
16. M. R. Patrick *et al*., Cyclic lava effusion during the 2018 eruption of Kīlauea Volcano. *Science* **366**, eaay9070 (2019). doi: 10.1126/science.aay9070
17. M. Gu, J. O. Berger, Parallel partial Gaussian process emulation for computer models with massive output. *Ann. Appl. Stat.* **10**, 1317–1347 (2016). doi: 10.1214/16-AOAS934
18. O. Roche, T. H. Druitt, Onset of caldera collapse during ignimbrite eruptions. *Earth Planet. Sci. Lett.* **191**, 191–202 (2001). doi: 10.1016/S0012-821X(01)00428-9
19. A. Geyer, A. Folch, J. Martí, Relationship between caldera collapse and magma chamber withdrawal: An experimental approach. *J. Volcanol. Geotherm. Res.* **157**, 375–386 (2006). doi: 10.1016/j.jvolgeores.2006.05.001
20. N. Geshi, J. Ruch, V. Acocella, Evaluating volumes for magma chambers and magma withdrawn for caldera collapse. *Earth Planet. Sci. Lett.* **396**, 107–115 (2014). doi: 10.1016/j.epsl.2014.03.059
21. S. Kusumoto, A. Gudmundsson, Magma-chamber volume changes associated with ring-fault initiation using a finite-sphere model: Application to the Aira caldera, Japan. *Tectonophysics* **471**, 58–66 (2009). doi: 10.1016/j.tecto.2008.09.001
22. B. M. Kennedy *et al*., Magma plumbing beneath collapse caldera volcanic systems. *Earth Sci. Rev.* **177**, 404–424 (2018). doi: 10.1016/j.earscirev.2017.12.002
23. J. Martí, A. Geyer, A. Folch, J. Gottsmann, in *Caldera Volcanism: Analysis Modelling and Response* (Elsevier, 2008), vol. 10, pp. 233–283.
24. A. Di Muro *et al*., The shallow plumbing system of Piton de la Fournaise Volcano (La Réunion Island, Indian Ocean) revealed by the major 2007 caldera-forming eruption. *J. Petrol.* **55**, 1287–1315 (2014). doi: 10.1093/petrology/egu025
25. G. Saito, Y. Morishita, H. Shinohara, Magma plumbing system of the 2000 eruption of Miyakejima volcano, Japan, deduced from volatile and major component contents of olivine-hosted melt inclusions. *J. Geophys. Res.* **115**, B11202 (2010). doi: 10.1029/2010JB007433
26. M. Bagnardi, F. Amelung, Space-geodetic evidence for multiple magma reservoirs and subvolcanic lateral intrusions at Fernandina Volcano, Galápagos Islands. *J. Geophys. Res.* **117**, 1–19 (2012). doi: 10.1029/2012JB009465
27. A. Belousov, M. Belousova, B. Edwards, A. Volynets, D. Melnikov, Overview of the precursors and dynamics of the 2012–13 basaltic fissure eruption of Tolbachik Volcano, Kamchatka, Russia. *J. Volcanol. Geotherm. Res.* **307**, 22–37 (2015). doi: 10.1016/j.jvolgeores.2015.06.013
28. W. W. Chadwick *et al*., The May 2005 eruption of Fernandina volcano, Galápagos: The first circumferential dike intrusion observed by GPS and InSAR. *Bull. Volcanol.* **73**, 679–697 (2011). doi: 10.1007/s00445-010-0433-0
29. D. A. Swanson *et al*., Cycles of explosive and effusive eruptions at Kīlauea Volcano, Hawai'i. *Geology* **42**, 631–634 (2014). doi: 10.1130/G35701.1
30. W. Ellis, *Narrative of a Tour Through Hawaii, Or Owhyhee* (Fisher and Jackson, 1825).
31. S. Baker, F. Amelung, Top-down inflation and deflation at the summit of Kīlauea Volcano, Hawaii observed with InSAR. *J. Geophys. Res.* **117**, B12406 (2012). doi: 10.1029/2011JB009123
32. R. S. Fiske, W. T. Kinoshita, Inflation of Kilauea volcano prior to its 1967–1968 eruption. *Science* **165**, 341–349 (1969). doi: 10.1126/science.165.3891.341; pmid: 17809512
33. P. F. Cervelli, A. Miklius, in *The Pu'u 'O'o-Kupaianaha Eruption of Kilauea Volcano, Hawai'i: The First 20 Years*, C. Heliker, D. Swanson, J. T. Takahashi, Eds. (USGS Professional Paper 1676, 2003), pp. 149–164.
34. M. P. Poland, J. Sutton, T. M. Gerlach, Magma degassing triggered by static decompression at Kilauea Volcano, Hawai'i. *Geophys. Res. Lett.* **36**, L16306 (2009). doi: 10.1029/2009GL039214
35. P. Lundgren *et al*., Evolution of dike opening during the March 2011 Kamoamoa fissure eruption, Kīlauea Volcano, Hawai'i. *J. Geophys. Res.* **118**, 897–914 (2013). doi: 10.1002/jgrb.50108
36. M. P. Poland, A. Miklius, E. K. Montgomery-Brown, Magma supply, storage, and transport at shield-stage Hawaiian volcanoes. *U.S. Geol. Surv. Prof. Pap. 1801*. **2010**, 1–52 (2014).
37. K. R. Anderson, M. P. Poland, Bayesian estimation of magma supply, storage, and eruption rates using a multiphysical volcano model: Kīlauea Volcano, 2000–2012. *Earth Planet. Sci. Lett.* **447**, 161–171 (2016). doi: 10.1016/j.epsl.2016.04.029
38. J. Dvorak, A. Okamura, J. H. Dieterich, Analysis of surface deformation data, Kilauea Volcano, Hawaii: October 1966 to September 1970. *J. Geophys. Res.* **88**, 9295–9304 (1983). doi: 10.1029/JB088iB11p09295
39. T. Ohminato, B. A. Chouet, P. Dawson, S. Kedar, Waveform inversion of very long period impulsive signals associated with magmatic injection beneath Kilauea volcano, Hawaii. *J. Geophys. Res.* **103**, 23839–23862 (1998). doi: 10.1029/98JB01122
40. B. Chouet, P. Dawson, Seismic source dynamics of gas-piston activity at Kīlauea Volcano, Hawai'i. *J. Geophys. Res.* **120**, 2525–2560 (2015). doi: 10.1002/2014JB011789
41. P. Segall, P. Cervelli, S. Owen, M. Lisowski, A. Miklius, Constraints on dike propagation from continuous GPS measurements. *J. Geophys. Res.* **106**, 19301–19317 (2001). doi: 10.1029/2001JB000229
42. D. J. Johnson, Dynamics of magma storage in the summit reservoir of Kilauea Volcano, Hawaii. *J. Geophys. Res.* **97**, 1807–1820 (1992). doi: 10.1029/91JB02839
43. A. J. Pietruszka, D. E. Heaton, J. P. Marske, M. O. Garcia, Two magma bodies beneath the summit of Kīlauea Volcano unveiled by isotopically distinct melt deliveries from the mantle. *Earth Planet. Sci. Lett.* **413**, 90–100 (2015). doi: 10.1016/j.epsl.2014.12.040
44. A. J. Pietruszka, J. P. Marske, D. E. Heaton, M. O. Garcia, J. M. Rhodes, An isotopic perspective into the magmatic evolution and architecture of the rift zones of Kīlauea Volcano. *J. Petrol.* **59**, 2311–2352 (2018). doi: 10.1093/petrology/egy098
45. D. F. McTigue, Elastic stress and deformation near a finite spherical magma body: Resolution of the point source paradox. *J. Geophys. Res.* **92**, 12931 (1987). doi: 10.1029/JB092iB12p12931
46. T. L. Wright, F. W. Klein, in *Dynamics of Crustal Magma Transfer, Storage and Differentiation*, C. Annen, G. F. Zellmer, Eds. (Geological Society of London, 2008), vol. 304, pp. 83–116. doi: 10.1144/SP304.5
47. D. Dzurisin, M. P. Poland, in *Field Volcanology: A Tribute to the Distinguished Career of Don Swanson*, M. P. Poland, M. O. Garcia, V. E. Cam, A. Grunder, Eds. (Geological Society of America, 2018), vol. 2538, pp. 275–295. doi: 10.1130/2018.2538(12)
48. P. R. Lundgren, M. Bagnardi, H. Dietterich, Topographic changes during the 2018 Kīlauea eruption from single-pass airborne InSAR. *Geophys. Res. Lett.* **46**, 9554–9562 (2019). doi: 10.1029/2019GL083501
49. L. Michon, F. Massin, V. Famin, V. Ferrazzini, G. Roult, Basaltic calderas: Collapse dynamics, edifice deformation, and variations of magma withdrawal. *J. Geophys. Res.* **116**, B03209 (2011). doi: 10.1029/2010JB007636
50. P. Segall, K. R. Anderson, I. Johanson, A. Miklius, Mechanics of inflationary deformation during caldera collapse: Evidence from the 2018 Kīlauea eruption. *Geophys. Res. Lett.* 2019GL084689 (2019). doi: 10.1029/2019GL084689

51. E. P. Holohan, M. P. J. Schöpfer, J. J. Walsh, Mechanical and geometric controls on the structural evolution of pit crater and caldera subsidence. *J. Geophys. Res.* **116**, B07202 (2011). doi: 10.1029/2010JB008032
52. O. Roche, T. H. Druitt, O. Merle, Experimental study of caldera formation. *J. Geophys. Res. Solid Earth* **105**, 395–416 (2000). doi: 10.1029/1999JB900298
53. R. Scandone, V. Acocella, Control of the aspect ratio of the chamber roof on caldera formation during silicic eruptions. *Geophys. Res. Lett.* **34**, L22307 (2007). doi: 10.1029/2007GL032059
54. J. Stix, T. Kobayashi, Magma dynamics and collapse mechanisms during four historic caldera-forming events. *J. Geophys. Res.* **113**, B09205 (2008). doi: 10.1029/2007JB005073
55. A. Folch, J. Martí, Time-dependent chamber and vent conditions during explosive caldera-forming eruptions. *Earth Planet. Sci. Lett.* **280**, 246–253 (2009). doi: 10.1016/j.epsl.2009.01.035
56. J. Martí, A. Folch, A. Neri, M. Giovanni, Pressure evolution during explosive caldera-forming eruptions. *Earth Planet. Sci. Lett.* **175**, 275–287 (2000). doi: 10.1016/S0012-821X(99)00296-4
57. B. A. Chouet, P. B. Dawson, M. R. James, S. J. Lane, Seismic source mechanism of degassing bursts at Kilauea Volcano, Hawaii: Results from waveform inversion in the 10–50 s band. *J. Geophys. Res.* **115**, B09311 (2010). doi: 10.1029/2009JB006661
58. D. R. Shelly, W. Thelen, P. Okubo, "Anatomy of a caldera collapse: Kilauea 2018 summit seismicity sequence in high resolution," presented at the Seismological Society of America Annual Meeting, Seattle, WA, 23 to 26 April 2019.
59. T. H. Druitt, R. S. J. Sparks, On the formation of calderas during ignimbrite eruptions. *Nature* **310**, 679–681 (1984). doi: 10.1038/310679a0
60. S. M. Bower, A. W. Woods, Control of magma volatile content and chamber depth on the mass erupted during explosive volcanic eruptions. *J. Geophys. Res.* **102**, 10273–10290 (1997). doi: 10.1029/96JB03176
61. T. Simkin, K. A. Howard, Caldera collapse in the Galápagos Islands, 1968. *Science* **169**, 429–437 (1970). doi: 10.1126/science.169.3944.429; pmid: 17739001
62. E. P. Holohan, M. P. J. Schöpfer, J. J. Walsh, Stress evolution during caldera collapse. *Earth Planet. Sci. Lett.* **421**, 139–151 (2015). doi: 10.1016/j.epsl.2015.03.003
63. L. Gailler *et al.*, 3D electrical conductivity imaging of Halema'uma'u lava lake (Kīlauea volcano). *J. Volcanol. Geotherm. Res.* **381**, 185–192 (2019). doi: 10.1016/j.jvolgeores.2019.06.001
64. P. W. Lipman, Subsidence of ash-flow calderas: Relation to caldera size and magma-chamber geometry. *Bull. Volcanol.* **59**, 198–218 (1997). doi: 10.1007/s004450050186
65. European Space Agency Sentinel Data Access; https://sentinel.esa.int/web/sentinel/sentinel-data-access.
66. Hawaiian Volcanoes Supersite; http://geo-gsnl.org/supersites/permanent-supersites/hawaiian-volcanoes-supersite/.
67. National Center for Airborne Laser Mapping, Hawaii Big Island Survey, OpenTopography (2012); doi: 10.5069/G9DZ067X
68. Kīlauea LiDAR Data (2018); https://kilauealidar.com.
69. I. A. Johanson, A. Miklius, Tiltmeter data from Kīlauea Volcano, Hawaii, spanning the 2018 eruption and earthquake sequence. U.S. Geological Survey data release, ScienceBase (2019). doi: 10.5066/P9310M9N
70. UNAVCO; https://unavco.org.

ACKNOWLEDGMENTS

E. Rumpf analyzed vent collapse from HVO webcam photos. P. Cervelli assisted with implementation of the analytical deformation model. M. McLay and Y. Zheng assisted with interferogram processing. This work benefited from numerous discussions with scientists at the Hawaiian Volcano Observatory and throughout the USGS. Any use of trade, firm, or product names is for descriptive purposes only and does not imply endorsement by the U.S. government. **Funding:** This work was funded by the USGS Volcano Hazards Program. **Author contributions:** K.R.A. conceptualized the project, analyzed data, developed the model, performed inversions, and coordinated manuscript writing. I.A.J. operated geodetic instruments, analyzed geodetic data, and contributed to modeling. M.R.P. installed and operated lava lake instrumentation and analyzed lava lake data. M.G. implemented the emulator, analyzed data uncertainties, and contributed to the Bayesian inversion. P.S. contributed to conceptualization, modeling, and validation of results. M.P.P. processed and analyzed InSAR data. E.K.M.-B. interpreted results and contributed to modeling. A.M. and all other authors contributed to data interpretation and manuscript production, and all USGS authors contributed to the eruption response and data collection. **Competing interests:** The authors declare no competing interests. **Data and materials availability:** Sentinel SAR data are available from (*65*); COSMO-SkyMed SAR data from (*66*); DEM data from (*67*, *68*), tilt data from (*69*), GPS data from (*70*), and lava lake data from (*9*).

SUPPLEMENTARY MATERIALS

science.sciencemag.org/content/366/6470/eaaz1822/suppl/DC1
Materials and Methods
Figs. S1 to S17
Tables S1 and S2
References (*71*–*117*)
Movie S1

20 August 2019; accepted 13 November 2019
10.1126/science.aaz1822

Science

Magma reservoir failure and the onset of caldera collapse at Kilauea Volcano in 2018

Kyle R. Anderson, Ingrid A. Johanson, Matthew R. Patrick, Mengyang Gu, Paul Segall, Michael P. Poland, Emily K. Montgomery-Brown and Asta Miklius

Science **366** (6470), eaaz1822.
DOI: 10.1126/science.aaz1822

Caldera collapse and flank eruption

Real-time monitoring of volcanic eruptions involving caldera-forming events are rare (see the Perspective by Sigmundsson). Anderson *et al.* used several types of geophysical observations to track the caldera-forming collapse at the top of Kilauea Volcano, Hawai'i, during the 2018 eruption. Gansecki *et al.* used near–real-time lava composition analysis to determine when magma shifted from highly viscous, slow-moving lava to low-viscosity, fast-moving lava. Patrick *et al.* used a range of geophysical tools to connect processes at the summit to lava rates coming out of far-away fissures. Together, the three studies improve caldera-collapse models and may help improve real-time hazard responses.

Science, this issue p. 1225, p. eaaz0147, p. eaay9070; p. eaaz1822; see also p. 1200

Science (print ISSN 0036-8075; online ISSN 1095-9203) is published by the American Association for the Advancement of Science, 1200 New York Avenue NW, Washington, DC 20005. The title *Science* is a registered trademark of AAAS.

Supplementary Materials for

Magma reservoir failure and the onset of caldera collapse at Kīlauea Volcano in 2018

Kyle R. Anderson*, Ingrid A. Johanson, Matthew R. Patrick, Mengyang Gu, Paul Segall, Michael P. Poland, Emily K. Montgomery-Brown, Asta Miklius

*Corresponding author. Email: kranderson@usgs.gov

Published 6 December 2019, *Science* **366**, eaaz1822 (2019)
DOI: 10.1126/science.aaz1822

This PDF file includes:

Other Supplementary Material for this manuscript includes the following:
(available at science.sciencemag.org/content/366/6470/eaaz1822/suppl/DC1)

Movie S1 (.mp4)

Materials and Methods

Time zone

All times are given in Hawaii Standard Time (HST).

GPS data

Daily positions (fig. S1) were generated from raw GPS phase and pseudorange data using the GIPSY software package, developed by JPL, with final satellite orbit files and clock corrections produced by JPL using data from International GNSS Service (IGS) stations. We computed station velocities separately using daily solutions from two time periods: 1) the three-day period between 2 May to 4 May inclusive (before the M_w 6.9 earthquake), and 2) the nine-day period between 6 May to 14 May inclusive (after the M_w 6.9 earthquake) (the former is used for interpretation only, not modeling). These daily solutions were derived from position data from 1 May at 14:00 to 4 May at 14:00, and 5 May at 14:00 to 14 May at 14:00, respectively. To be conservative we did not model GPS data before 5 May, so the time series excludes slightly more than one day of post-seismic motion triggered by the M_w 6.9 south flank earthquake.

We computed white noise uncertainties from standard deviations of detrended data from 1 January to 1 April 2018. We neglected random-walk and other temporally-correlated noise terms due to the short period of observation. We also neglected correlated uncertainty between instruments and between channels. Constant velocities (Figs. S1, S2, S3) were estimated by linear regression, with uncertainty determined by linear propagation of errors utilizing the white noise covariance matrix. The highest subsidence rate during 6-14 May is ~8 cm/day at NPIT and formal velocity errors are less than 1 mm/day on all stations and channels; thus, signal-to-noise ratio on near-field instruments was very high.

Tilt data

Tilt rates were computed from one-minute data recorded over the six-day period from 5 May (00:00) to 10 May (23:59) (fig. S4). This time period is slightly shorter than that for the GPS data in order to avoid data gaps at station IKI, loss of the east channel at UWE (the instrument reached its maximum tilt), and a change in tilt azimuth at SDH beginning on the morning of 11 May which is not reflected at other instruments. However, due to the steady nature of summit deflation, use of a shorter time period should not bias estimated rates. We removed an offset in time series at ESC, SDH, and SMC due to an M_w 3.7 earthquake south of the caldera on 6 May at 19:50, but we did not attempt to remove small offsets associated with pre-collapse explosions. Note that in our modeling we do not use data from stations SMC and SDH (the former due to persistent questions about its response to reservoir pressure change (*6*, *71*), and the latter due to flooding of its borehole by groundwater at the end of March 2018, the effect of which on the data is not yet well understood).

We estimated tilt rates by linear regression of unweighted time series data. Noise in tilt data can be difficult to characterize, exhibiting strong temporal correlations and varying greatly between instruments; uncertainty in the orientation of the instrument in the ground can also add a constant bias to all measurements (*71–74*). By analyzing years of tilt data at the summit of Kīlauea prior to 2014, (*6*) estimated uncertainties in

computed net (total) tilts over 7 days at most stations of roughly 0.3 to 1 μrad, which suggests an uncertainty exceeding 0.1 μrad /day (in reality the uncertainty does not grow linearly with time). Differences in recorded tilt at stations UWE and UWD, which are located in the same borehole, can shed additional light on uncertainty. UWE is an Applied Geomechanics 722 analog borehole tiltmeter sampling at one minute, while UWD is an Applied Geomechanics LILY digital borehole tiltmeter sampling at 1 Hz, from which one-minute data are computed by averaging. We found that azimuths differed by roughly 10 degrees (fig. S5) and tilt rates over the studied period by about 4 μrad/day (20.8 μrad/day at UWE vs. 16.9 μrad/day at UWD). These differences are larger than would be expected from the noise characteristics of the individual instruments. Based on these differences we assigned a subjective 1σ uncertainty of ±2 μrad/day to each channel for each instrument. We did not attempt to account for correlation of uncertainties between channels or stations.

InSAR data

We used two interferograms from the COSMO-SkyMed platform operated by the Italian Space Agency (ASI) and two from the Sentinel-1 platform, operated by the European Space Agency (ESA) (figs. S6, S7); times of acquisitions are given in table S1. Interferograms were processed using the GAMMA software package and corrected for topographic phase using digital elevation models from 30-m-resolution Shuttle Radar Topography Mission data (*75*) for Sentinel interferograms, and from 4.5-m-resolution airborne SAR data (collected by NOAA in 2005; see (*76*) for more information) for Cosmo-SkyMed interferograms. Interferograms were filtered following (*77*) and unwrapped using the Statistical-Cost, Network-Flow Algorithm for Phase Unwrapping (SNAPHU) and masked at a cost threshold of 300 (*78*). InSAR deformation rates were computed by dividing line-of-sight (LoS) displacements by the time between acquisitions.

InSAR data measure line-of-sight displacements relative to a point assumed to be nondeforming and vertical biases (shifts) are evident between images. We approximately removed these biases using velocities from the continuous GPS network, and we also estimated an unknown stochastic bias term for each interferogram in our full Bayesian parameter estimation; see below.

InSAR data contain not only random pixel noise but also strong spatial correlations caused by atmospheric phase delays. To estimate noise, including spatial correlation between pixels, we assumed that noise in each image is stationary and computed empirical isotropic semivariograms (*79*) using 5000 pixels selected randomly from a disc-shaped region extending from 5 to 20 km from the approximate center of maximum summit subsidence. This excludes most volcanic deformation and also very distant points which may have different noise characteristics due to large horizontal gradients in topography and atmospheric conditions at Kīlauea. In order to obtain stable range and sill parameters (below) we also removed best-fit ramp functions (planes) from each interferogram before computing semivariograms (but note that these planes are not removed from the data we use for the inversion).

Empirical semivariograms vary between the four InSAR scenes due to the complex spatiotemporal variations of atmospheric noise (and also any small unwrapping errors). We fit empirical semivariograms Υ using an exponential model with nugget fixed to zero:

$\Upsilon(\nabla) = s[1 - \exp(-\nabla/r)]$, where h_I is the Euclidian distance between pixels in each InSAR scene, s is the variance at large distances (the sill), and r controls the change in variance with distance (the range). Covariance between any two points may be computed using $C(\nabla) = s[\exp(-\nabla/r)]$. We estimated range parameters of 6-9 km, and sills of ~0.3 to 0.4 cm/day for all scenes except for the descending-model COSMO-SkyMed scene, for which we estimated a sill of 0.6 cm/day (note that we converted interferograms from displacements to rates before computing semivariograms).

To reduce computational cost, we downsampled data using the quadtree algorithm of (*80*), yielding ~200-300 observation points for each interferogram. The quadtree procedure averages groups of pixels of variable size (box size depends on data variance within each box); thus, the variance of each quadtree pixel is lower than the variance of the full-resolution data (*79*, *81*). To compute covariance Σ between quadtree pixels with indices i and j using the covariance derived from the full un-binned data we used (*79*, *81*)

$$\Sigma_{i,j} = \frac{1}{n_i n_j} \sum_{k=1}^{n_i} \sum_{l=1}^{n_j} C_{k,l}(\nabla_{i,j,k.l})$$

where n_i and n_j are the number of points in quadtree box i and j, respectively, and $\nabla_{i,j,k.l}$ is the Euclidian distance between the kth point and lth point in the quadtree box i and j, respectively. (Note that if all pixels share the same uncorrelated variance σ^2 then off-diagonal terms are zero and $\Sigma_{i,i} = \sigma^2/n_i$).

Lava lake data

Surface height of the lava lake (fig. S8) was obtained chiefly from automated laser rangefinder measurements, but as the lake drained the system became unable to image the surface (*9*). We therefore supplemented this time series with 1) a manual laser rangefinder measurement on 6 May, 2) and structure-from-motion (SfM)-based estimates derived from photographs taken on 8 and 9 May (*9*). Additionally, images from a continuously operating thermal camera located on the rim of Halema‘uma‘u crater (*82*) and with a view deep into the vent yielded a near-continuous estimate of lava lake surface height until 9 May, when the lake drained out of sight of the camera. Lava lake level was manually measured in units of pixels in the thermal images using the program Tracker (https://physlets.org/tracker/), and then converted to absolute elevation using the camera's GPS position and viewing geometry together with an SfM-derived model of the drained lava lake vent (*9*).

Absolute uncertainties in laser rangefinder distances were of order ~centimeters, but height and orientation of the instrument added additional (fixed) uncertainties of order ~1 m (*9*). For simplicity we assumed uncorrelated white noise errors of 0.5 m. For a handheld laser rangefinder measurement on 6 May at 18:20 we used an uncertainty of 1 m (*9*). For SfM-based estimates we used uncertainties from (*9*) of 1.9 m and 8.3 m on 8 and 9 May, respectively. The thermal camera images yield a height estimate that may be somewhat biased by the optical properties of the lens, uncertainty in viewing geometry, and estimating the lake surface using thermal gradients on the far wall of the vent.

We found that raw thermal camera estimates align imperfectly with the laser data, which we consider to be far more precise. We therefore adjusted the thermal time series

by estimating an unknown slope and offset which minimizes the squared residual between the laser observations and the thermal observations from the time period after the M_w 6.9 earthquake. The resulting fit is quite good. We use the adjusted thermal camera data only to qualitatively infer draining rate between 6-9 May for comparison with SfM-based estimates.

The data show a clear increase in the rate of lava lake draining on the evening of 4 May, after which the rate is remarkably constant (thermal data after 7 May do suggest some irregularity in the withdrawal rate, but a fairly stable average rate). The final SfM estimate on 9 May suggests a slightly reduced rate of draining, but this estimate was relatively uncertain, and geodetic data do not suggest a reduction in pressure change rate.

We computed the rate of withdrawal of the lava lake surface by weighted linear regression to the combined laser and SfM time series from after the M_w 6.9 earthquake using for simplicity uncorrelated (white noise) uncertainties specified above. We decimate the laser rangefinder data to a ~1 minute sampling rate. We estimated a post-M_w 6.9 velocity of -52.97 m/day and subjectively assigned an uncertainty of ±2 m/day.

Finally, the rate of lava lake withdrawal may be combined with subsequent vent photogrammetry to estimate volumetric rates of magma withdrawal (*9*). Rates averaged around ~15 m^3/s over eight days but were much reduced as the lake fell due to a smaller conduit diameter at depth. Here we assumed an average rate of withdrawal from the lava lake and its feeder conduit of no more than 5-10 m^3/s before 16 May.

Lava lake density

Gravity data indicated that the density of lava in the very top tens to perhaps hundreds of meters of the lake was only ~1,000-1500 kg/m^3 (*83*, *84*). However, density must increase greatly with depth due to greater pressure and consequent increased volatile solubility, eventually reaching the density of magma stored in the Halema‘uma‘u reservoir – estimated to be 2550-2650 kg/m^3 [e.g., (*37*)]. Furthermore, (*4*) argued that a difference in elevation between lava in the summit lake and at the ERZ eruptive vent during brief eruption pauses could be explained by an ERZ magma density that was 50-140 kg/m^3 higher than the average lava lake density (from reservoir to surface). Thus, average bulk lava lake density cannot have differed greatly from the density of magma stored at greater depth in the summit and ERZ.

To characterize uncertainty in density we used a probability distribution that is uniform between 2300 and 2500 kg/m^3 and falls off with a normal distribution (standard deviation = 150 kg/m^3) outside of this range (fig. S9). These values are comparable to summit host rock densities inferred from Bouguer gravity studies (*85*) and seismic p-wave velocities (*86*) using relationships in (*87*), but are somewhat lower than the density of shallow (upper few hundred meters) caldera fill (*88*).

Host rock shear modulus

Elastic stiffness of the rock surrounding Kīlauea’s shallow magma reservoir is not well known. Laboratory experiments on Hawaiian basalt suggest a shear modulus from less than 5 to more than 40 GPa (*42*, *89*) but in-situ rigidities are almost certainly lower than laboratory values, and some authors have argued that μ<3 GPa is required to explain the lack of a piezomagnetic effect during unrest at Kīlauea (*42*, *90*). Based on these studies, (*6*) used a lognormal prior distribution with mean of 3 GPa. Recent tomography

and near-source v_p/v_s estimates at the summit (*86*, *91*) suggest p-wave velocities increasing from ~3.3 km/s at 2 km below the summit to ~5.2 km/s at 4 km and v_p/v_s of ~1.7. Using

$$\mu_d = \rho_r v_s^2$$

where ρ_r is rock density we estimated a dynamic shear modulus μ_d of roughly 10-25 GPa from 2-4 km depth. Static shear moduli of rocks are generally lower than dynamic moduli, but the relationship depends on uncertain factors such as crack density (*92*). To characterize the uncertainty in shear modulus we used a probability distribution for $\log_{10}(\mu)$ that is uniform between 2 and 10 GPa, falls off with standard deviation of 0.3 GPa outside of this range, and is zero below 0.5 GPa and above 20 GPa (fig. S9).

Lava lake model

Based on previous observations that the surface of Kīlauea's lava lake rises and falls in direct proportion to magma reservoir pressure (*4*) we assume that the lava lake acted as a piezometer (manometer) of magma reservoir pressure such that reservoir centroid pressure change rate $\dot{p}$ was related to rate of change in lava lake surface height $\dot{h}$ through

$$\dot{p} = \rho g \dot{h}$$

where ρ is the average density of magma in the lava lake (from the top of the reservoir to the surface) and g is gravity.

The magmastatic relationship between reservoir pressure and lava lake surface height was well-established prior to the 2018 eruption. This relationship requires that viscous resistance to flow in the conduit is minimal compared with gravitational forces. To verify that this assumption held in 2018, when draining rates were high, we looked at data from the Kamoamoa intrusion and fissure eruption in 2011, during which the summit lava lake drained nearly 200 m in a little over a day, simultaneous with inward tilt of ~40 μrad at station UWE. Although sustained for a much shorter period than in 2018, these rates were much higher (the lava lake receded almost four times as rapidly in 2011 as in 2018). These rates give a lake-tilt ratio at UWE of about 5 meters per μrad – very similar to the rate for much slower pressure changes over many years (*4*, *5*). We conclude that the magmastatic relationship was valid in 2011 and thus almost certainly must have held during lower draining rates in 2018 (neglecting as unimportant any changes in lava lake vent dimensions between the two time periods).

We also evaluated the validity of assuming a time-invariant average lava lake density. Because the lava lake density must have increased with depth, the average lake density from the reservoir to the surface decreased as the total magma column length decreased during draining. Such a change would alter the relationship between reservoir pressure and lava lake surface height. To test the influence of this effect we assumed a uniform vent radius and approximated the lake as a low-density foam of $\rho_1 = 1000$ kg/m^3 above magma of $\rho_2 = 2500$ kg/m^3. This formulation is simple but generally consistent with gravity data and with the idea that changes in lake density are driven by bubbles, which rise through the magma and accumulate in a foam layer at the top (or collapse and lose gas). Under these assumptions, average density can be computed using

$\rho = \rho_1 L/h + \rho_2(1 - L/h)$ where L is the height of the low-density foam cap and h is the total column height. Change in density during draining is greatest for a relatively thick cap above a relatively short conduit. For a cap height of 150 m (*83*, *84*) and H decreasing by 350 m (somewhat greater than observed during lake draining in 2018) from an initial 750 m, the change in average density is only a little more than 10%. This minor change is consistent with the near-constant relationship between tilt and lava lake level observed after the M_w 6.9 earthquake during draining, and we conclude that changing lava lake density did not significantly affect our measurements in 2018. Note also that although the final 2018 lava lake height estimate suggested a slightly reduced rate of lake withdrawal (fig. S8), the uncertainty in this observation was high, and a reduction in withdrawal rate is not expected from a reduction in average density (which would rather increase the change in lava lake surface height for a given change in reservoir pressure).

Relationship between lava lake and ground tilt

We defined R_t as the ratio of lava lake surface height to ground tilt (in units of m/μrad). To estimate R_t we resampled the 1-minute caldera-radial tilt time series to obtain values at the time of lava lake observations and then performed separate weighted linear regressions to data from before and after the earthquake (for the latter we used data after 5 May). We weighted lava lake data by uncertainties described above and assumed that tilt data are error-free. The final two lava lake data points, derived from SfM, fall slightly above the slope of the previous points but have higher uncertainties. At most stations we found that R_t after the M_w 6.9 was about 0.6 times its value before the M_w 6.9. We assigned a subjective uncertainty of ±0.15 m/μrad to R_t.

Is it reasonable to assume that the pressure-tilt relationship remained constant between the disappearance of the lava lake and the first collapse event? This ratio was observed to be constant for many years (*5*), and although it did change around the time of the M_w 6.9 earthquake (Fig. 3D), large increases in lava lake withdrawal and deformation rates both also occurred at that time. Because the ratio remained constant after the M_w 6.9 (when data is available), and ground deformation subsequently continued at a nearly constant rate after the lake disappeared, it seems reasonable to assume that there were no further changes prior to the first collapse event.

After the onset of collapse events, the relationship between tilt and pressure change is more complex. As one end member, assuming that collapse-induced ground deformation was due entirely to reservoir pressurization, the scaling relationship may not have changed. However, this assumption neglects the influence of other processes on the tilt data during this time, so is likely only partly valid (*50*).

Pressure at the onset of collapse

An important goal is to estimate the pressure change in the shallow magma reservoir at the onset of caldera collapse. To do so we divided the data into two periods: before and after the M_w 6.9 earthquake. To compute pressure change prior to the earthquake we used $\Delta p(t) = \rho g \Delta h(t)$ where $\Delta h(t)$ is the lava lake surface height relative to its approximate average level prior to the onset of deflation (1027 m asl). A lava lake density of 2400 kg/m^3 (the mean of the prior probability distribution we used, above) yields a pressure change at 12:30 pm on 4 May, immediately prior to the M_w 6.9 earthquake, of -1.9 MPa. Accounting for uncertainty in ρ using 1×10^6 samples drawn from its probability

distribution, we found Δp = -1.9 ± 0.12 MPa. If pressure decreased at a steady 1.25 MPa/d (main text) over the 12.2 days between the M_w 6.9 earthquake and the first collapse on 16 May, then total pressure reduction from the onset of deflation (including the pre-M_w 6.9 period) would have been 17.2 ± 1.1 MPa.

As an alternative approach for computing pressure change after the M_w 6.9 earthquake, we used tilt data as a direct proxy for reservoir pressure change using $\Delta p(t) = \Delta\theta(t) R_t \rho g$, where $\Delta\theta$ is the change in tilt relative to 1 pm on 4 May (just after the M_w 6.9 earthquake) at a particular station, and R_t is the ratio of lava lake surface height to ground tilt (above) observed after the M_w 6.9 earthquake before the lake disappeared (Fig. 3D). We used the radial component of data on all tiltmeters except at UWE, for which we used north tilt (the east channel was non-functional during part of this time period). We used 1×10^6 samples drawn from probability distributions for ρ and R_t (above) and found that uncertainty in ρ dominated our estimated uncertainties. Adding pre-M_w 6.9 pressure change to post-M_w 6.9 pressure change we obtained results in Fig. 7 and S10. For most stations, total estimated pressure decrease by the time of the first collapse on 16 May was between 15-20 MPa. Because we did not know which instrument most faithfully recorded reservoir pressure change, we finally combined all samples for all instruments, yielding a pressure change of -17.8 ± 2.1 MPa. This result is consistent with the model-based estimate, above, as expected by the near-constant rate of deformation in the caldera.

Further assuming that the lake-tilt ratio remained constant between the onset of collapses on 16 May and the onset of larger collapses on 29 May, we inferred a pressure change on 29 May of a bit less than 25 MPa (from UWD; pressure change inferred from IKI is higher, at nearly ~34 MPa, but this instrument is less sensitive to reservoir pressure changes (*6*) and experienced data gaps during the 2018 eruption). These results assumed that collapse-induced ground deformation was due entirely to reservoir pressurization with a relationship unchanged from the pre-collapse period. This assumption is likely not completely correct (*50*). At the other extreme, if episodic inflationary deformation was unrelated to pressurization of the reservoir, pressure reduction would have been greater after 16 May than estimated here. Although we find this scenario unlikely, our estimated pressure change for 29 May should be considered much more uncertain than for 16 May.

Ground deformation model

We computed ground deformation (displacement and tilt) as a function of reservoir pressure change using a numerical model of a spheroidal magma reservoir embedded in a homogeneous elastic medium. The spheroid may not dip but may take any aspect ratio from prolate (vertical pipe) to oblate (horizontal pancake). We did not account for topography due to the relatively flat terrain at Kīlauea's summit. We neglected as minor the ground deformation caused by the lava lake conduit itself. (Finite element calculations for a vertical cylindrical conduit with radius 100 m extending from the surface to the reservoir suggest less than 1 cm and 3 cm of vertical and horizontal surface displacements, respectively, from removal of the lava lake, even close to the vent, and a displacement field that decays rapidly with distance.) We neglected viscoelastic crustal processes, the time scales of which should be much longer than the duration of the time period considered here, and treated the crust as a homogeneous elastic material. Although numerous caldera-bounding faults clearly exist at Kīlauea, and collapse in 2018 occurred

in part along pre-existing zones of weakness, InSAR data from early May do not in general show strong discontinuities across faults and there is not a strong correlation between the pre-existing caldera shape and the pattern of ground deformation [as often observed at calderas (*93*)], although some heterogeneity is clearly present within the caldera.

Analytical deformation models for spheroidal magma reservoirs exist [e.g., (*94*, *95*)] but the assumptions that go into their derivation break down for reservoirs relatively close to the surface – a condition that likely exists at Kīlauea. To overcome this limitation we constructed a numerical (finite-element) deformation model [e.g., (*96*)] implemented in COMSOL Multiphysics (fig. S11). The general form of our radially-symmetric finite element model is given by

$$\boldsymbol{u}_j(\boldsymbol{x_r}) = \frac{V\dot{p}}{\mu} g_j(d, \omega, V, \nu; \boldsymbol{x_r})$$

where $\boldsymbol{u}$ is the deformation velocity vector, subscript j indicates the deformation component (either radial or vertical), $\boldsymbol{x_r}$ is the vector of radial observation coordinates on the free surface, V is reservoir volume, $\dot{p}$ is reservoir pressure change rate, μ and ν are shear modulus and Poisson's ratio respectively (material properties), d is reservoir centroid depth, and ω is aspect ratio of the reservoir (height/width; not to be confused with the aspect ratio of the roof block above the reservoir). Here g is the nonlinear functional relationship between reservoir geometry, Poisson's ratio, and deformation, computed by the finite element model, with units of 1/length^2. Deformation is linear in the term $V\dot{p}\mu^{-1}$, which can be considered a geodetic source strength, but displacements are also nonlinearly related to volume V through the function g. In practice therefore we parameterized the finite element model by only the parameters d, ω, and V (we fixed ν to 0.25) and an arbitrary $\dot{p}$ and μ, and then later scaled the results using $\dot{p}/\mu$ to yield deformation for any pressure change and shear modulus.

We confirmed that the finite element model reproduces results from analytical models in (*45*) and (*94*, *95*) in cases where the analytical models are expected to be valid (relatively small, deep reservoirs) (fig. S12).

Emulator for the ground deformation model

Running a full finite element model many thousands of times, as required in an MCMC simulation, is prohibitively slow; for this reason most inversions utilizing FEM deformation models involve optimization (finding the best-fitting solution) (*97*) rather than a full characterization of the posterior PDF. To overcome this limitation, we developed an emulator (surrogate model) to approximate the finite element model output at any combination of model parameters using the actual finite element model output from a small, carefully-selected set of model parameters. We utilized the well-studied Gaussian stochastic process (GafSP) (*98–100*). For each set of inputs (height, width and depth of the reservoir) the finite element model outputs displacements at a vector of pre-selected radial distances. To emulate the displacement vector, which is a highly nonlinear function of the input parameters, we implemented the parallel partial Gaussian stochastic process (PP GaSP) emulator developed in (*17*). Similar sets of input parameters generally predict more similar (correlated) output. The kernel function in the PP GaSP emulator

models this correlation as a function of the distances between the inputs, which captures the nonlinearity in the geodetic model.

In implementing the PP GaSP emulator, we assumed a product Matérn kernel function of the model outputs at any observation coordinate (*101*) and estimated range parameters by the marginal posterior mode with the jointly robust prior (*102*) The shared covariance function across different observation coordinates reduces the computational complexity of fitting an emulator with distinct kernel functions at different coordinates (*17*). On the other hand, ground displacements from the geodetic model change greatly as a function of spatial coordinate (distance on the surface from the reservoir), so we assume distinct mean and variance parameters at each observation coordinate. The different mean and variance parameters at observation coordinates are crucial for capturing the change of the geodetic model.

Given a kernel function, we estimated the mean and variance parameters of the ground displacement at any observation coordinate by the posterior mean estimator using the reference prior (*101*, *103*). Note that the parameters only needed to be estimated once when constructing the emulator. For any new input parameters we used the predictive mean of the emulator to compute ground displacements. We implemented the MATLAB version of the PP GaSP emulator in (*104*).

To implement the PP GaSP emulator, we first computed $n \approx 700$ selected space-filling design inputs (combinations of models parameters) from the maximin Latin Hypercube (*105*) and then deleted combinations that were nonphysical or highly implausible; we were left with $n = 376$. For each of these remaining points we ran the finite element forward model, storing predicted horizontal (radial) and vertical displacements at $k = 1700$ spatially-dense distances spaced in proportion to the square root of distance from 0.01 m to ~30 km. Using all outputs we estimated the parameters of the PP GaSP emulator. The predictive mean of the trained emulator can finally be used to predict output at any arbitrary set of input parameters at the same 1700 pre-specified distances, and output at other distances can be computed using linear interpolation. We found that this two-step approach yields fast and accurate predictions at any coordinate.

To compute ground tilt we performed spatial differentiation of emulated vertical displacements. Predicted radial displacements were converted to east and north using station coordinates. Finally, InSAR displacements were computed by taking the dot product of the 3-component displacement vector with a normal vector representing the oblique look direction between the satellite and ground.

The computational cost of building the emulator (estimating the parameters of the PP GaSP emulator) scales as the maximum of $O(n^3)$ and $O(kn^2)$, where n is the number of design points and k is the number of observation points. However, this need be done only once, and exercising the fully constructed emulator in the MCMC inversion scales as $O(nk)$. We found that exercising the emulator to predict output is orders of magnitude faster than the finite element model, and several times faster than even the analytical model (*95*) for large numbers of observations points (e.g., InSAR data).

Fig. S13 compares output from the full finite element model, the emulator, and the analytical model for combinations of model parameters selected randomly from the posterior distribution of a model simulation. The emulator faithfully reproduces the finite element model, but both often differ significantly from the analytical model which does

not properly enforce a uniform pressure boundary condition when the chamber is relatively close to the surface.

The R package of the emulator code is available at the Comprehensive R Archive Network (*103*) and the MATLAB version is available at GitHub (*104*).

Combined deformation-lake model for Bayesian parameter estimation (inverse)

To estimate properties of the magma storage system and its temporal evolution prior to collapse we developed a combined geodetic - lava lake model. This model relates reservoir pressure change rate $\dot{p}$ to ground deformation rate (GPS $\dot{u}$, tilt $\dot{\theta}$, and InSAR $\dot{v}$) at observation coordinates $\mathbf{x}_{GPS}$, $\mathbf{x}_{\text{tilt}}$, and $\mathbf{x}_{InSAR}$, respectively, using our emulator, and to the rate of lava lake surface height change using the magmastatic relationship. The full system of equations is given by:

$$\dot{\mathbf{u}}_j(\mathbf{x}_{GPS}) = f_j(\boldsymbol{\xi}, \dot{p}, V, \omega, \nu, \mu; \mathbf{x}_{GPS})$$

$$\dot{\boldsymbol{\theta}}_{j=1,2}(\mathbf{x}_{\text{tilt}}) = -\frac{\partial f_3(\boldsymbol{\xi}, \dot{p}, V, \omega, \nu, \mu; \mathbf{x}_{\text{tilt}})}{\partial \mathbf{x}_{\text{j=1,2}}}$$

$$\dot{\mathbf{v}}_I(\mathbf{x}_{InSAR}) = \widehat{\alpha_I} \cdot f\left(\boldsymbol{\xi}, \dot{p}, V, \omega, \nu, \mu; \mathbf{x}_{\text{InSAR}_I}\right) + \lambda_I$$

$$\dot{h} = \dot{p}/\rho g$$

where f is the ground deformation model (the emulated finite element model supplemented with parameters such as those necessary to convert from radial to cartesian coordinates), subscript $j = 1,2,3$ is the spatial direction (east, north, up), $\boldsymbol{\xi}$ is the reservoir centroid position (east, north, and depth), I is the interferogram number, $\widehat{\alpha}$ is a normal vector representing the oblique look direction between the satellite and ground which converts 3D displacements to line-of-sight satellite displacements, and λ_I is a bias term which accounts for constant shift in each interferogram (because interferograms measure relative displacement). East and north positions are relative to 19.4073° N, 155.2784° W (near the east rim of pre-collapse Halema‘uma‘u crater). Because we model the volcano as a flat elastic halfspace, depths are approximately relative to mean observation elevation of ~1100 m asl.

Excluding parameters that we set to fixed values (Poisson’s ratio $\nu = 0.25$ and gravity $g = 9.81$), the full model includes the parameters $\boldsymbol{\xi}, \dot{p}, V, \omega, \mu$ and ρ.

Data and relationship with model

To constrain the model, we used ground deformation velocities and the rate of lava lake withdrawal (as well as prior information, discussed below). For ground deformation we used the data from 14 continuous GPS instruments, three borehole tiltmeters, and four InSAR interferograms from the Sentinel-1 and COSMO SkyMed platforms (table S1).

We assumed that observed data $\mathbf{d}$ may be explained by

$$\mathbf{d}_k(\mathbf{x}_k) = \mathbb{G}_k(\mathbf{m}; \mathbf{x}_k) + \boldsymbol{\delta}_k(\mathbf{x}) + \lambda_k + \boldsymbol{\epsilon}_k$$

where subscript k refers to the individual data set (GPS, tilt, InSAR, or lava lake), $\mathbb{G}$ is the full forward model described above (which can be treated as sub-models necessary to

predict each data set), model vector $\mathbf{m} = [\boldsymbol{\xi}, \dot{p}, V, \omega, \mu, \rho, \nu, g]^T$, $\boldsymbol{\delta}$ accounts for discrepancy between the model and reality, $\boldsymbol{\lambda}$ is a mean (bias) parameter, and $\boldsymbol{\epsilon}$ is observation error. Observation errors $\boldsymbol{\epsilon}$ are estimated directly from the data, as described above, and are held constant during the inverse. Terms $\boldsymbol{\delta}$ account for discrepancies between the mathematical representation and the earth, and in geophysical inversions are often masked by relatively large data uncertainties $\boldsymbol{\epsilon}$. In this work, however, signal-to-noise ratio in most geodetic data is very high. Although discrepancy terms can be modeled using statistical functions (*106*), for simplicity here we fixed $\boldsymbol{\delta} = \mathbf{0}$ and utilized the approach of (*107*) to weight geodetic data uncertainties (data covariance matrices) with unknown hyperparameters to account in a simplified way for unmodeled data error and model discrepancy (we did not weight the lava lake data, which can be fit to within uncertainty without compromising the fit to any other data sets). After (*107*), we assumed $\boldsymbol{\epsilon}_k \sim N(\mathbf{0}, \gamma_k^2 \Sigma_k)$ where Σ_k is the data covariance matrix (estimated directly from the data) and γ_k is the unknown weight hyperparameter for the *k*th data set.

$\boldsymbol{\lambda}$ terms are nonzero only for InSAR data and account for the fact that unwrapped interferograms yield deformation only relative to a point which is assumed to be non-deforming, yielding possible constant bias in all pixels (we assumed that ramp terms due to satellite orbital errors are minimal over the relatively small area of the images). Treating the bias correction as part of the geophysical model and including $\boldsymbol{\lambda}$ terms in the model vector, then,

$$\mathbf{d}_k(\mathbf{x}_k) = \mathbf{G}_k(\mathbf{m}; \mathbf{x}_k) + \boldsymbol{\epsilon}_k$$

The full data vector including N interferograms is given by

$$\mathbf{d} = \left[\dot{h}, \dot{\mathbf{u}}, \dot{\boldsymbol{\theta}}, \dot{\mathbf{v}}_1, \cdots, \dot{\mathbf{v}}_N\right]^T$$

where $\dot{h}$ is lava lake surface height rate, $\dot{\mathbf{u}}$ is deformation velocity (GPS), $\dot{\boldsymbol{\theta}}$ is tilt rate, $\dot{\mathbf{v}}$ are InSAR velocities, and $N = 4$ is the total number of interferograms. The uncertainties for each element of $\mathbf{d}$ are independent.

Bayesian inverse formulation

Our goal was to probabilistically estimate model parameters $\mathbf{m} = [\boldsymbol{\xi}, \dot{p}, V, \omega, \mu, \rho, \boldsymbol{\lambda}]^T$ as well as hyperparameters γ. We treated γ and all parameters in $\mathbf{m}$ as unknowns and allowed them to vary over reasonable a priori ranges.

To probabilistically constrain model parameters we used observed data and independent prior information from the results of previous studies. We framed the estimation problem in a Bayesian sense, in which probability density functions (PDFs) characterize prior constraints (information about model parameters derived from independent sources – here, previous studies), data uncertainties, and the parameter estimates that are the solution to the inverse problem. We applied informative priors to constrain the density of the lava lake and the rigidity (shear modulus) of the host rock. The philosophy of our Bayesian inversion is to evaluate the full range of model parameters consist with the data and prior information. It is important however to remember when interpreting posterior PDFs that they are conditional upon the assumptions that go into the inverse (model, data uncertainties, and priors).

Using data weighting hyperparameters as described above, the likelihood for each data set k is given by

$$P_k(\mathbf{d}_k|\mathbf{m},\boldsymbol{\gamma}_k^2) = (2\pi\gamma_k^2)^{-N_k/2}|\Sigma_k|^{-1/2}\exp\left[-\frac{1}{2\gamma_k^2}\mathbf{r}_k^T\Sigma_k^{-1}\mathbf{r}_k\right]$$

where N is the number of data points in the data set, and $\mathbf{r}$ is the residual vector, $\mathbf{r}_k = \mathbf{d}_k - \mathbf{G}_k(\mathbf{m})$. The total likelihood is given by the product of the individual likelihoods:

$$P(\mathbf{d}|\mathbf{m},\gamma^2) = P(\mathbf{d}_1,\mathbf{d}_2,\cdots,\mathbf{d}_K,|\mathbf{m},\gamma_1^2,\gamma_2^2,\cdots,\gamma_K^2) = \prod_{k=1}^{K} P_k\,(\mathbf{d_k}|\mathbf{m},\gamma_k^2)$$

where K is the total number of datasets. Similarly, assuming independence, prior distributions are given by

$$P(\mathbf{m},\boldsymbol{\gamma}^2) = \prod_{n=1}^{M} P\,(m_n)\prod_{k=1}^{K} P\,(\gamma_k^2)$$

where M is the total number of model parameters. Likelihood and prior distributions are combined using Bayes' Theorem:

$$\begin{aligned} P(\mathbf{m},\boldsymbol{\gamma}^2|\mathbf{d}) &= P(\mathbf{d}|\mathbf{m},\boldsymbol{\gamma}^2)P(\mathbf{m},\boldsymbol{\gamma}^2) \\ &= \prod_{k=1}^{K} P_k\,(\mathbf{d_k}|\mathbf{m},\gamma_k^2)P_k(\gamma_k^2)\prod_{n=1}^{M} P\,(m_n) \end{aligned}$$

Bayesian prior information

Information derived from independent studies in the literature is essential for placing constraints on lava lake density ρ and host rock shear modulus μ. Both parameters are important in the volcano model but neither can necessarily be resolved by our data. These studies and our interpretation of them are uncertain, so priors must be characterized by probability distributions.

Additionally, we placed an a priori physical constraint on the top depth of the magma reservoir, rejecting models which placed magma in unreasonable proximity to the surface. This is not clearly known but should be below (and perhaps well below) the level at which the lava lake drained from sight (at ~700 m asl, roughly 400 m below our mean GPS station elevation). We computed the reservoir's top depth directly from the model's geometric parameters and rejected (assigned zero probability) to modeled reservoirs which placed magma closer than 750 m to the surface.

For other parameters we used uniform prior distributions between fixed lower and upper bounds. All parameters were sampled in Cartesian space except for pressure change rate, reservoir volume, shear modulus, reservoir aspect ratio, and data weighting hyperparameters (discussed in the next sections); we estimated the logarithm of these parameters and treated their priors as uniform on a log scale. In practice the posterior

distributions for pressure change rate and reservoir aspect ratio are so well constrained by the data that the choice of their objective prior distributions makes little difference.

Inverse algorithm

We sampled the posterior distribution using a standard Markov chain Monte Carlo (MCMC) algorithm (*108*, *109*) as implemented by (*37*). The Metropolis MCMC acceptance test utilizes the ratio of posterior probability between a given set of model parameters and a perturbed set osf model parameters. For the MCMC acceptance test in the presence of unknown hyperparameters γ see (*107*). We ran 8 independent parallel MCMC chains each for 1×10^6 iterations, storing every 10th sample. We ensured that all runs converged to similar distributions and then combined all samples to derive final posterior PDFs. In practice, we found that posterior distributions are adequately characterized with far fewer samples than we computed here.

Fits to data

Figs. 7 and S15 show the fit of model predictions to data. Data fits are qualitatively very good but cannot explain the GPS and InSAR data to within formal uncertainties. These discrepancies are likely due to the geometrical simplicity of the deformation model, which cannot account for magma outside of the primary spheroidal storage reservoir. Elastic heterogeneity likely also plays a role. Our estimated hyperparameters scale the data covariance matrices to account for this discrepancy. We estimated mean hyperparameter values for tilt, GPS, and InSAR data of 1.0, 14.7, and 2.1, respectively (fig. S17). Tilt data uncertainties are thus largely unmodified, InSAR data uncertainties roughly doubled, and GPS uncertainties increased by more than an order of magnitude.

Post-processing: reservoir centroid pressure

Given posterior distributions $P(\mathbf{m}, \boldsymbol{\gamma}^2|\mathbf{d})$ it is straightforward to compute dependent parameters (those that can be computed explicitly as functions of the estimated model parameters) using the posterior samples directly or by using Monte Carlo procedures. Using the posterior PDF for reservoir centroid depth d from the Bayesian inverse analysis together with the prior distribution for magma density ρ, we probabilistically estimated pressure at the centroid depth using the magmastatic relationship. This estimate neglects pre-eruptive overpressure, which we argue was minimal due to the presence of a lava lake overflowing from the open vent.

Post-processing: volume change rate

We computed $\dot{V}$ from inverse results using $\dot{V} = \beta_{ch} V \dot{p}$ where β_{ch} is magma reservoir compressibility (which describes the relative change in reservoir volume for a given pressure change), and for V and $\dot{p}$ we use posterior samples taken directly from the inverse results. Following (*110*), we computed reservoir compressibility using the finite element method for an arbitrary non-dipping spheroidal reservoir as a function of its depth, geometry, and the shear modulus μ of the host rock. For a deeply-buried sphere $\beta_{ch} = 3/4\mu$ (*45*) but compressibility can be quite different for relatively large, shallow reservoirs or for non-spherical sources (*110*, *111*) (fig. S14). Using the same general emulation technique described above we built an emulator for the finite element output using ~800 design points (pre-computed finite element model outputs). Reservoir

compressibility is a scalar value that does not depend on distance from the reservoir, so emulator construction was more straightforward. Our estimate of $\dot{V}$ is independent of host rock shear modulus and as a result is well-constrained.

Post-processing: magma compressibility and flow rate

To compute the volumetric rate of magma flow from the reservoir we used $q = \dot{V}(1 + R)$ where $R \equiv \beta_m/\beta_{ch}$ and β_m is magma compressibility (which describes relative change in magma density for a given change in pressure). The ratio R may be computed explicitly using physical models [e.g., (*110*, *112*, *113*)] and/or constrained a priori using observations and modeling from other volcanoes and eruptions (*37*). Here we used a prior distribution for R modified slightly from (*37*), which was derived from theoretical constraints and previous observations at Kīlauea. Our distribution is uniform between 0.25 and 3 and decreases normally outside of this range with a standard deviation of 0.5. Combining this prior distribution with reservoir compressibility β_{ch} computed using the emulator and estimated shear modulus from MCMC samples, we were also able to compute a distribution for magma compressibility β_m that is consistent with data and the independent constraint on R. Our results suggest a magma compressibility of 2×10^{-10} to 9×10^{-10} at 68% credible bounds (fig. S17, table S2). These values are mostly higher than estimated by (*112*) for a gas-poor basalt, so suggest the presence of bubbles in the reservoir. Note that our estimate for β_m is constrained largely by priors on R and μ rather than the data (although our results do suggest a shear modulus at the low end of its prior distribution; fig. S17).

Probabilistic 3D constraint on magma storage ("pseudotomography")

We randomly selected 1000 sets of model parameters from the posterior distribution, computed the 3D spheroidal reservoir geometry for each, and combined these on a $250 \times 250 \times 250$ grid to estimate the relative probability of finding magma at a given 3D location beneath the caldera (*114*).

Pressure change and host rock failure

Reservoir pressure change induces stress in the surrounding crust; in the case of roof failure, these stresses exceed the strength of the rock. A deflating spherical reservoir will induce compression above the reservoir and tension at distances greater than some critical value, but collapse processes are complex and there has long been debate about the nature of collapse fractures and their relation to the stress field (*115*), even neglecting complexity such as reservoir shape or pre-existing rock weaknesses. Theoretical models have even suggested that spherical reservoirs are unlikely to generate ring faults (*23*). Nonetheless, a simple force balance can be used to relate reservoir pressure change with shear stress on a hypothetical vertical cylindrical ring fault:

$$\tau_c = \frac{\Delta p}{4R_a}$$

where τ_c is the change in shear stress before failure and R_a is roof aspect ratio (*18*, *20*). Calculations are given in the main text. Additionally, although outside the scope of this work, τ_c may be related to failure criterion such as Mohr-Coulomb (*18*, *20*, *54*). Ignoring

any prior shear stress or extension due to south flank motion, the normal stress on faults extending to 1-2 km would be ~25 MPa; neglecting cohesion, this suggests a coefficient of friction of about 0.3 to 0.5.

Influence of propagating faults on geodetic data

Many laboratory experiments have indicated that roof block failure begins with the propagation of faults from near the top of the reservoir (*116*). Slip along ring-like faults at depth can localize deformation in the caldera, biasing geodetic inversions which assume a homogeneous elastic medium and even leading to overlapping deformation patterns which could be misinterpreted as caused by two reservoirs (*117*). Upwards propagation of these faults during continued reservoir depletion would increasingly localize deformation into a piston-like subsiding block.

We modeled data from before the onset of clear fault propagation and argue that the effect of such processes on our data should be minor. InSAR data from Kīlauea in 2018 demonstrate that strain localization likely associated with slip on buried faults did occur but was not largely developed until after our modeled time period. Secondly, the observed deformation pattern during our modeled pre-collapse time period was similar to that observed variously over many years at Kīlauea when there was no evidence of fault slip (*6*, *31–34*, *36*, *37*), and our modeled source depth and geometry are similar to previous analyses of these data. Thirdly, geophysical signals indicative of collapse-induced reservoir pressurization did not occur before 16 May (excepting small events likely caused by rockfalls into the lava lake). Although this does not entirely preclude motion along buried faults [and abundant seismicity may indicate the early stages of slip (*58*)] it does preclude the sudden collapse of large rock masses into the reservoir during such slip (slow and steady collapse might not be detected). Despite these arguments we do acknowledge the possibility that slip on buried faults could somewhat bias our results, and we note certain relatively minor changes in the geodetic time series over several days before 16 May that could be due to these processes.

Change in the lake-deformation ratio and influence of the south caldera reservoir

The ratio between lava lake surface height and radial ground tilt (R_t) at station UWE was nearly constant for many years, so the change around the time of the M_w 6.9 is notable. The change in this ratio was produced by a larger increase in deformation rate than lake withdrawal rate. Using the magmastatic lava lake relationship, the ratio of lava lake surface height rate to deformation rate is proportional to

$$\frac{\mu}{\rho V g}$$

Decreasing this ratio by 40% (Fig. 3D) requires correspondingly decreasing the shear modulus, or increasing lava lake density or reservoir volume. Such a large change in lava lake density is implausible on physical grounds and would also have dramatically affected the lake draining rate. Such a large decrease in shear modulus likewise seems unlikely, although the M_w 6.9 and related seismicity could have had some effect (there is some evidence that the change in lake-tilt ratio began somewhat before the M_w 6.9, however). Finally, increasing the effective reservoir volume (perhaps by tapping into new

sources of magma) would presumably also have slowed the rate of reservoir pressure change (which in elastic models is inversely proportional to volume), unless compensated by an increase in outflux rate. A reduced rate of pressure change is contrary to the data.

The expression above does not account for geodetic sources which are not in direct magmastatic connection with the lava lake. An increase in deformation rate from such a source could reduce R_t, but would presumably also change the spatial pattern of deformation. Deflation of Kīlauea's south caldera reservoir is evident in our data misfits, but the modeled Halemaʻumaʻu reservoir explains the great majority of observed subsidence. Nonetheless, we acknowledge that some bias is possible.

Although the cause of the change in R_t is not clear, we can speculate about the effect of mismodeling it. The pressure change rate we estimated is obtained directly from the lava lake time series, so is insensitive to changes in R_t. Furthermore, the pressure time series in Fig. 6 and fig. S10 are entirely empirical and rely only on R_t remaining constant over each time period. If deformation due to an unmodeled source affected the geodetic data but not the lava lake data, we would overestimate reservoir volume. Ultimately it is difficult to quantify the effect that these uncertainties have on our results, and although we believe them to be largely second-order we acknowledge that some bias to estimated parameters could occur.

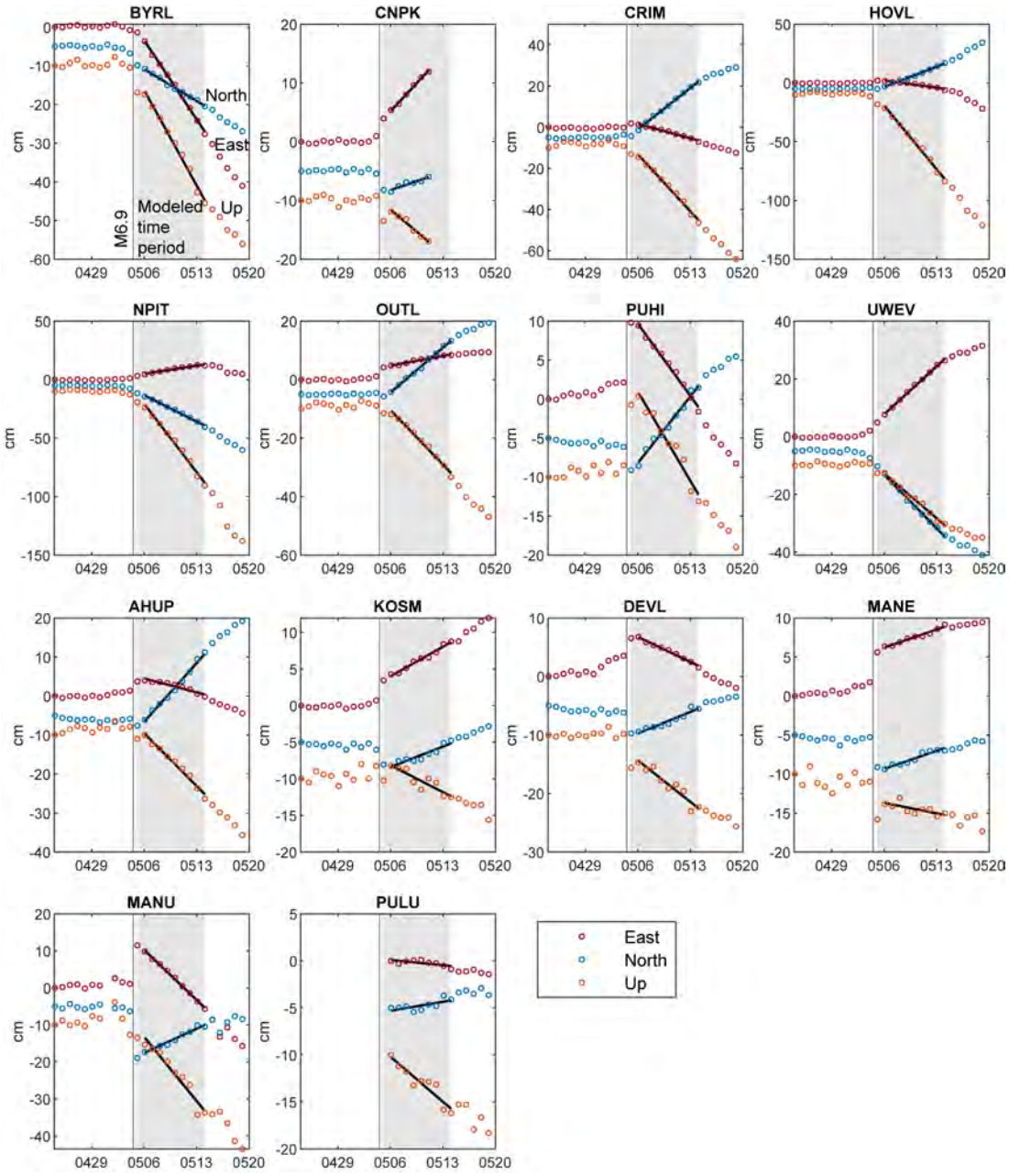

Fig. S1.

Daily GPS solutions and best-fit velocities. Vertical line on 4 May shows the time of the M_w 6.9 south flank earthquake (abbreviated "M6.9"). For clarity, coseismic M_w 6.9 earthquake offsets are approximately removed using data from high-rate GPS solutions (significant residuals remain at some stations). Pre-M_w 6.9 velocities are also estimated for comparison, but for clarity are not shown here. Period used to compute post-M_w 6.9 velocities shaded in gray.

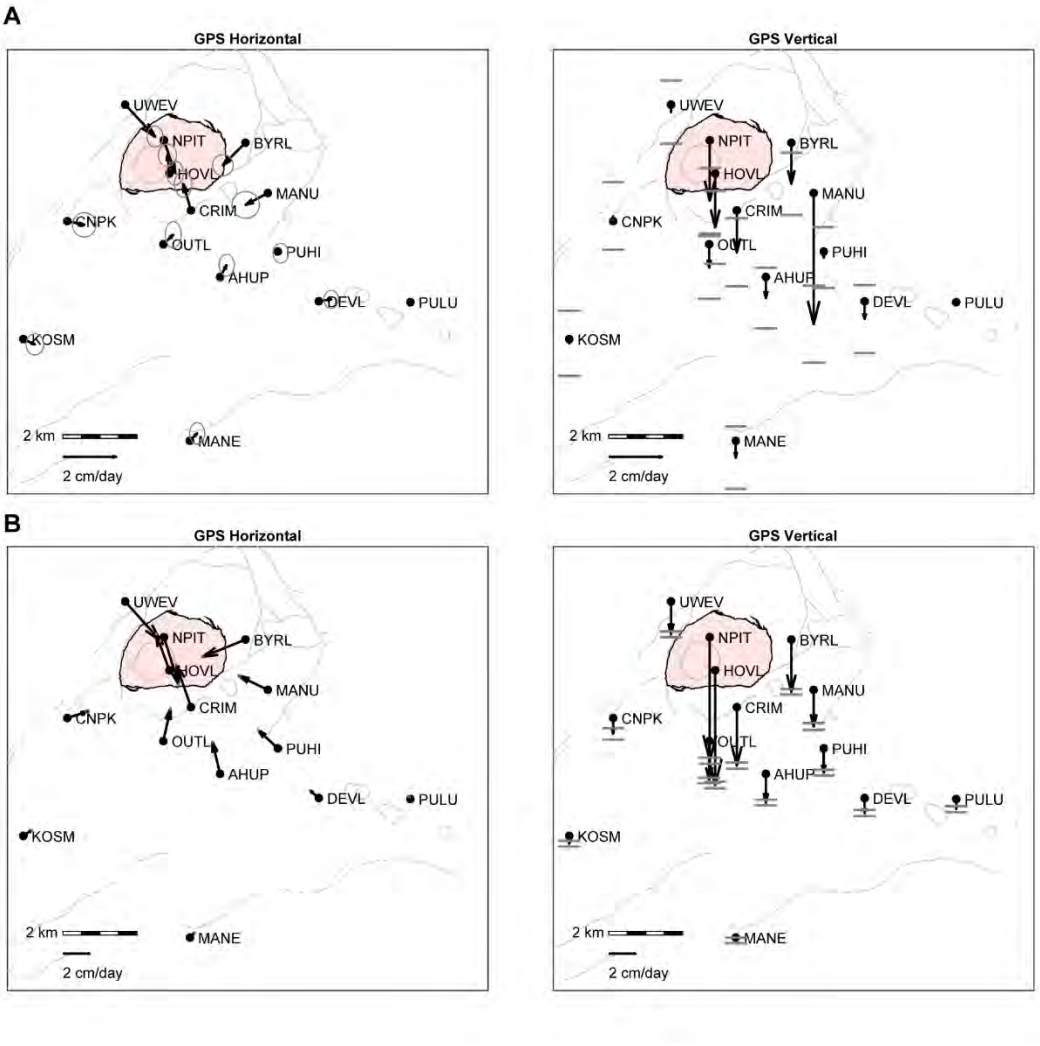

Fig. S2.

Best-fit GPS velocity vectors with formal uncertainties. Background line map shows location of summit caldera; shaded area shows 2018 collapse. (**A**) 2-4 May. (**B**) 6-14 May. Confidence ellipses and bars are 95%. Map units are meters east and north of 19.4073° N, 155.2784° W (east rim of pre-collapse Halema‘uma‘u crater). 2-4 May velocities are not used in modeling and are shown here only for comparison; note that vertical motion at MANU during this time is an outlier.

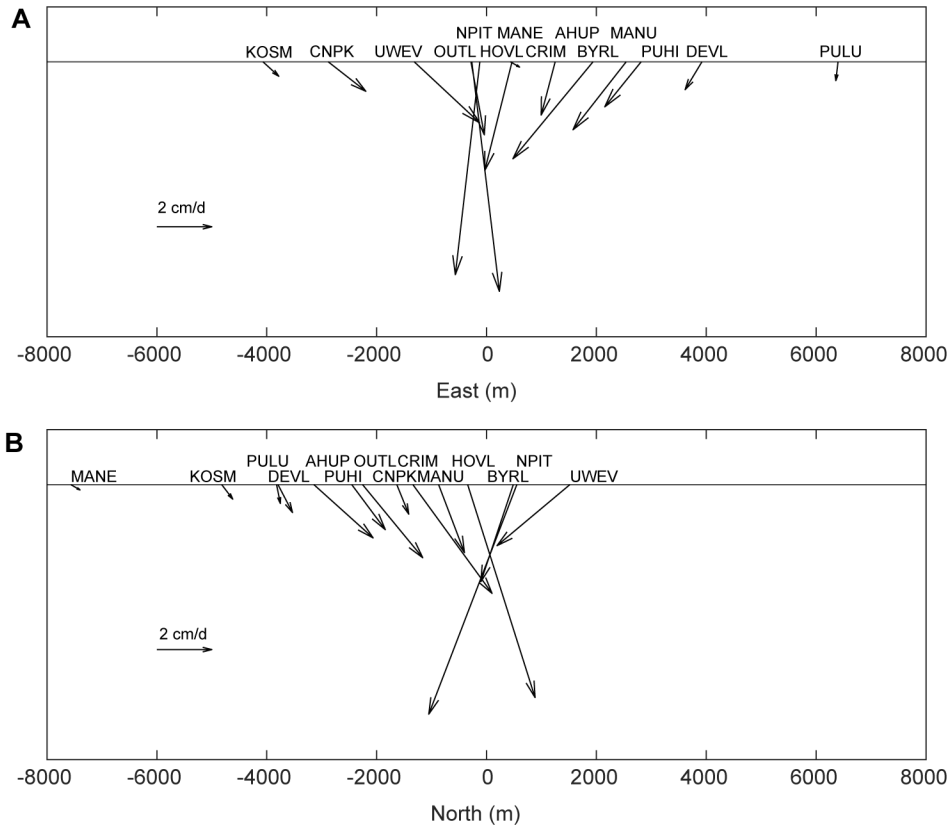

Fig. S3.

GPS velocity vectors for 6-14 May. All stations are plotted as if at the same elevation (horizontal line). (**A**) View looking north. (**B**) View looking west. Distances are relative to the center of the local coordinate system.

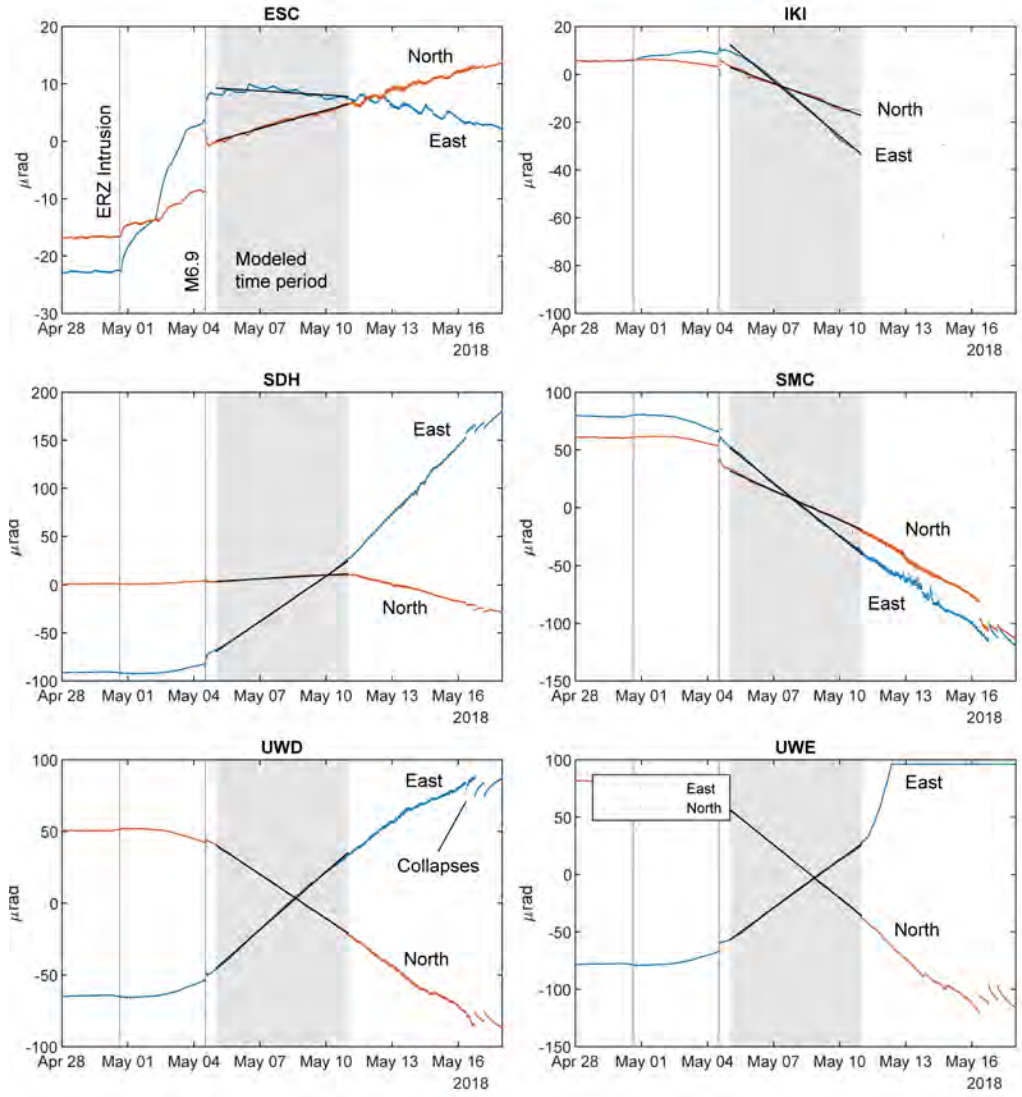

Fig. S4.

Ground tilt and best-fitting velocities. The first vertical line is the onset of the LERZ dike intrusion and middle ERZ rift contraction, which was clearly recorded at ESC; the second vertical line is the M_w 6.9 earthquake. Note that UWE reached its maximum instrumental east-west tilt around ~11 May. Offsets associated with the M_w 6.9 earthquake are roughly removed from the times series.

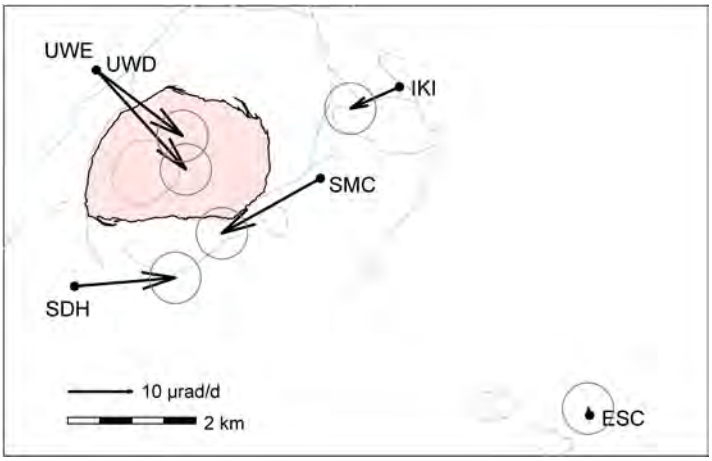

Fig. S5.

Tilt vectors for shaded time period in fig. S4, with 95% data uncertainties. Shaded area shows 2018 collapse. SMC and SDH are not modeled in this study.

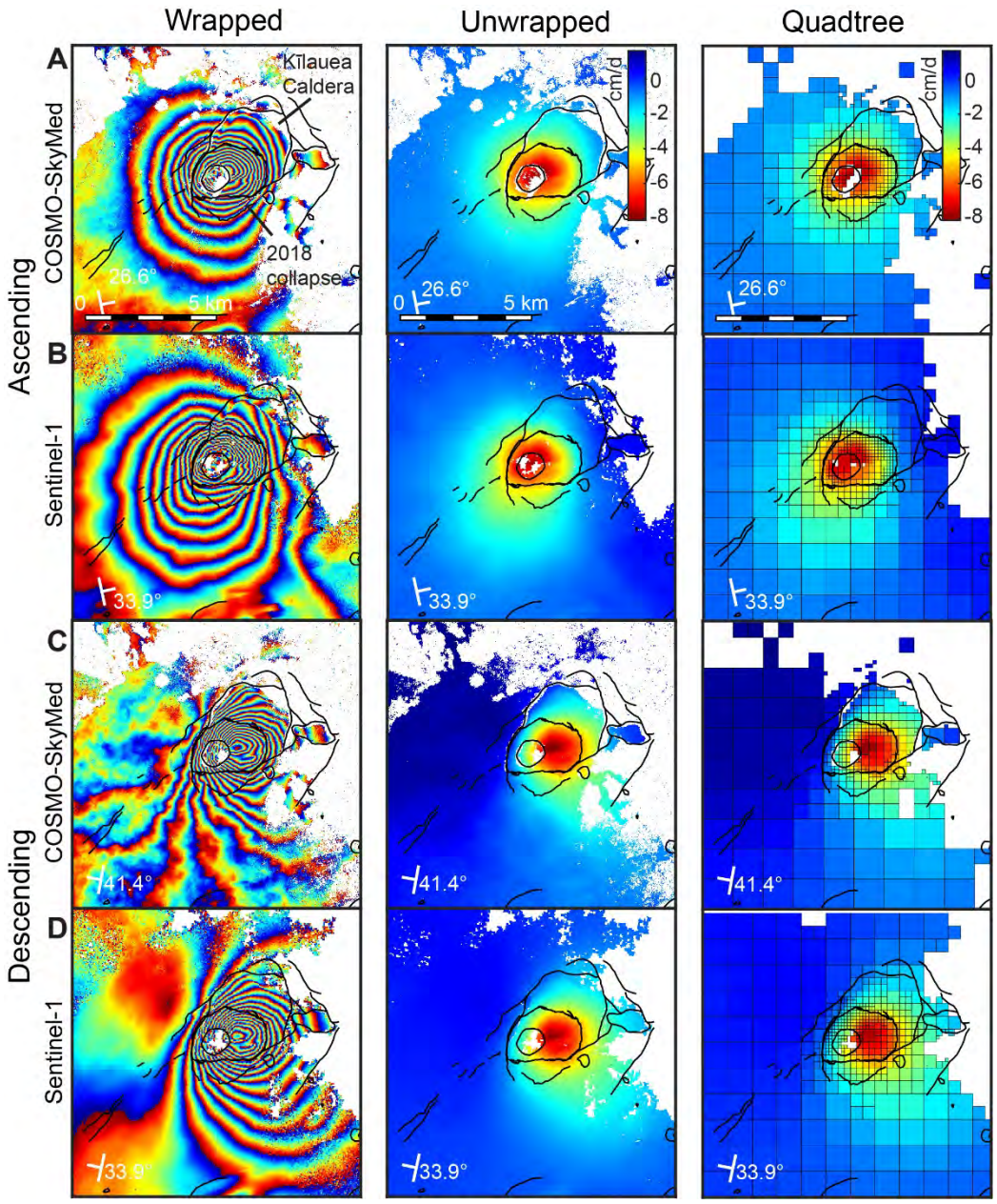

Fig. S6.

InSAR data used in this study. Rows show interferograms corresponding to letters in table S1. The first column is re-wrapped at a rate of 0.5 cm/day per fringe, the second is unwrapped, and the third is quadtree-decimated. The look vector symbol (lower left of each panel) denotes the flight direction and look direction of the satellite. The look direction is always 90 degrees perpendicular to the right of the flight direction. The number in degrees indicates the deviation of the radar signal from vertical.

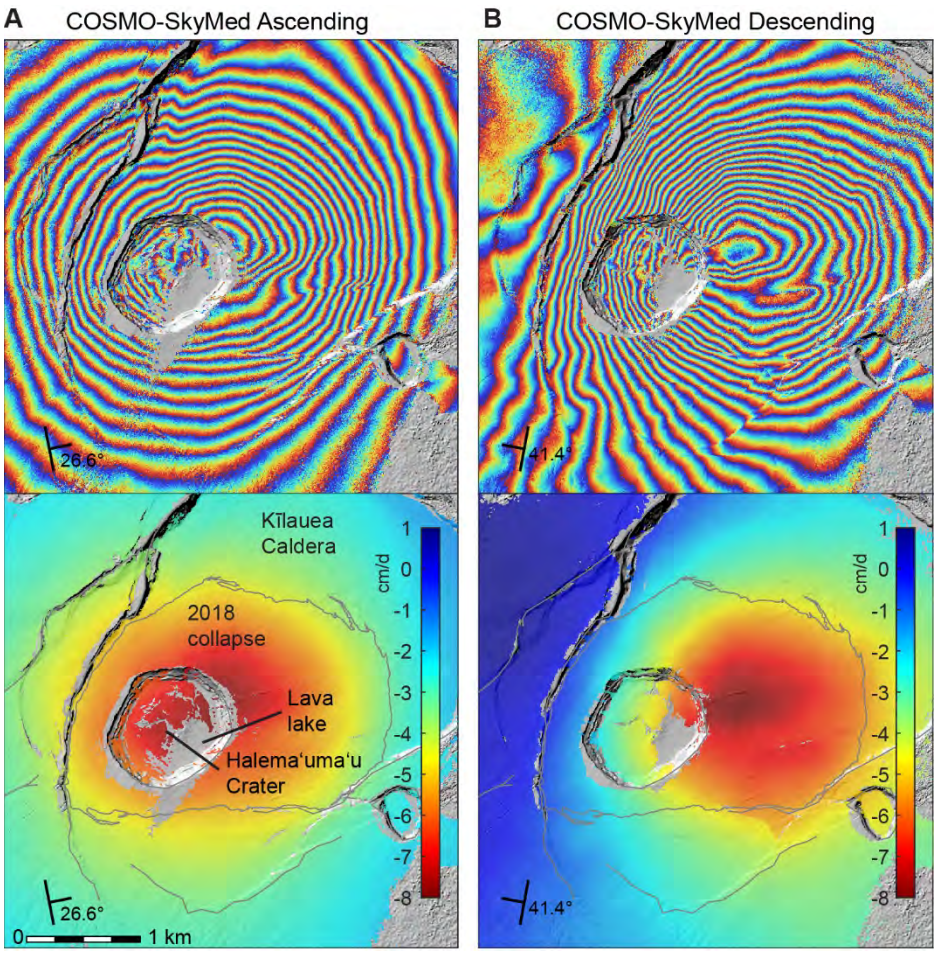

Fig. S7.

Enlarged ascending-mode (**A**) and descending mode (**B**) COSMO-SkyMed interferograms showing subsidence at Kīlauea's summit (A and C in table S1, respectively). Background DEM shows pre-collapse topography. Data are rewrapped at 0.3 cm/day per fringe to better show details of deformation in the caldera. A roughly-circular subsidence pattern was centered just east of Halema‘uma‘u crater. Second-order perturbations to the overall pattern are evident, however, particularly in the high-resolution ascending-mode scene which reveals kinks in the fringe pattern near the caldera wall north and east of the crater, and small fault offsets. The descending-mode image (B) also shows some complexity in the fringe pattern over the source east of the crater (a pattern which has been observed previously at Kīlauea). The descending-mode image is relatively noisier; the look angle is also more oblique (less vertical).

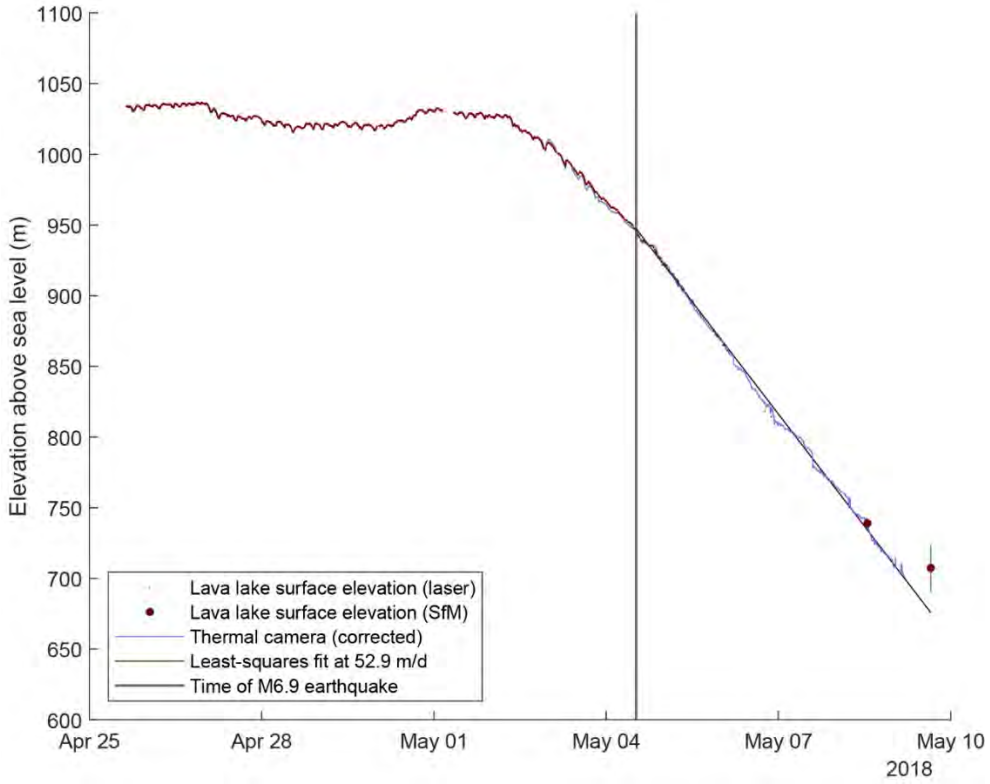

Fig. S8.

Lava lake surface height from laser rangefinder, thermal camera (corrected as described in the text), and SfM photogrammetry. Confidence bars for SfM points are 95%. Vertical line is the M_w 6.9 earthquake.

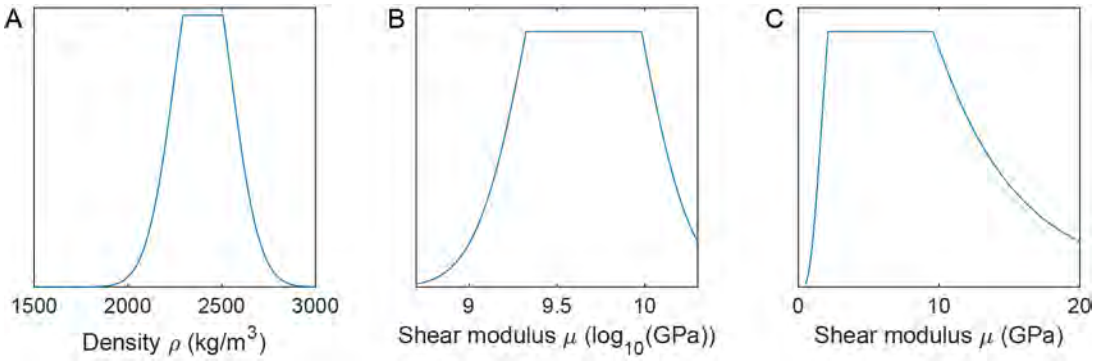

Fig. S9.

Prior distributions. Probabilities are zero outside of the range shown here and the y axes are relative probability only. (**A**) Average lava lake and conduit magma density. (**B**) Host rock static shear modulus. (**C**) Shear modulus in linear space, shown for convenience only (we estimate the log of shear modulus, as shown in B).

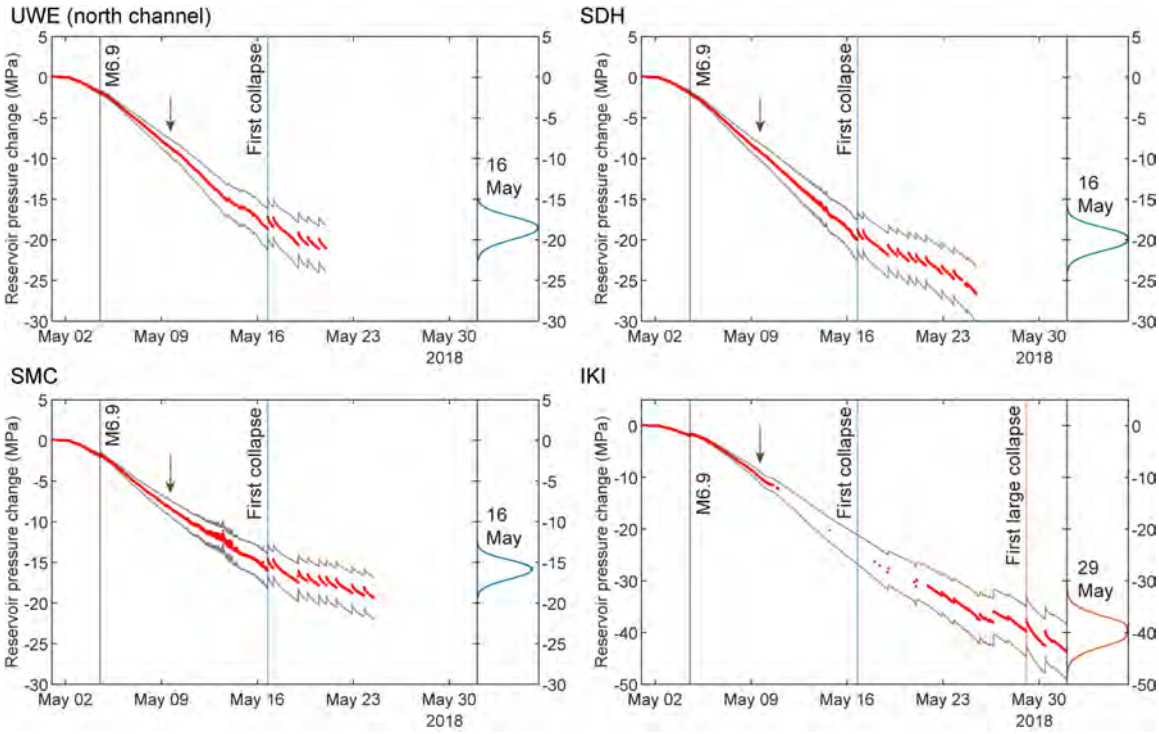

Fig. S10.

Pressure change distributions obtained by scaling tilt data at stations UWE, SDH, SMC, and IKI (UWD is presented in the main text). Arrow denotes the time of the last lava lake measurement on 9 May. Time series include small offsets associated with pre-collapse explosions, which are likely due to changes in reservoir pressure; spikes associated with earthquakes are also evident.

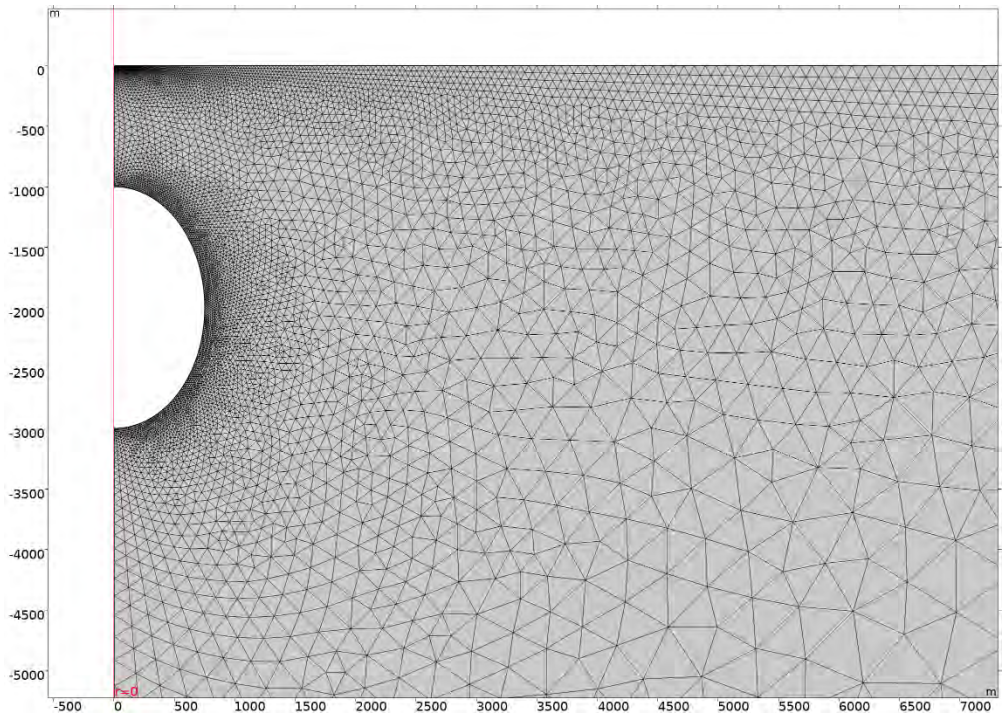

Fig. S11.

A portion of an example finite element mesh with reservoir centroid at 2 km depth with vertical radius of 1000 m and horizontal radius of 750 m (in practice we compute deformation due to reservoirs of different aspect ratios at many different depths). The model is symmetric about the vertical red line.

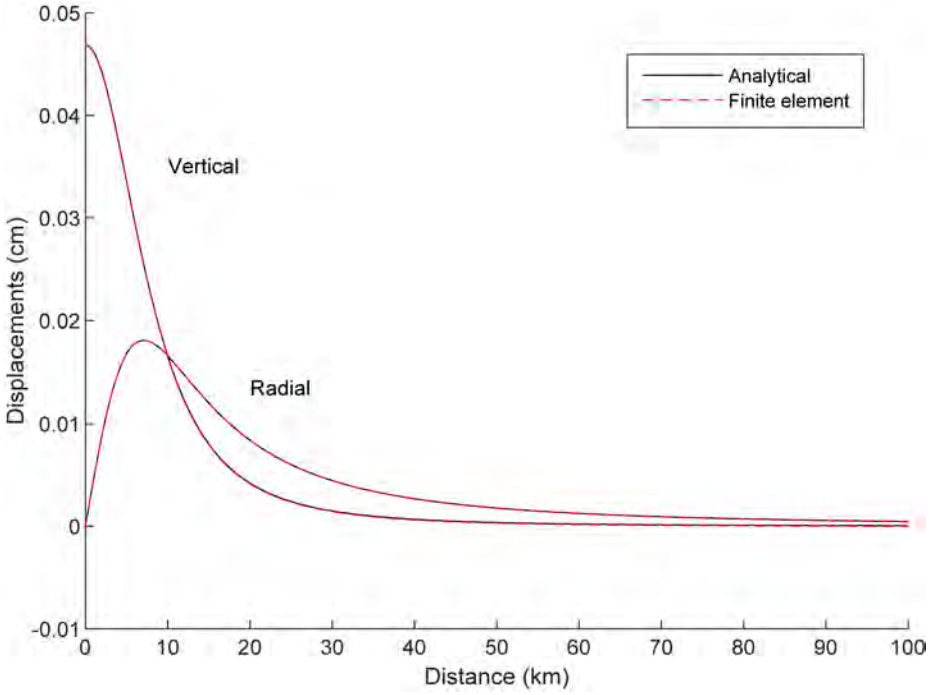

Fig. S12.

Comparison of finite element results with the McTigue analytical spherical reservoir model, here for a reservoir with radius 500 m at 10 km depth with a uniform 10 MPa pressure boundary condition in an elastic halfspace with shear modulus of 20 GPa and Poisson's ratio of 0.25.

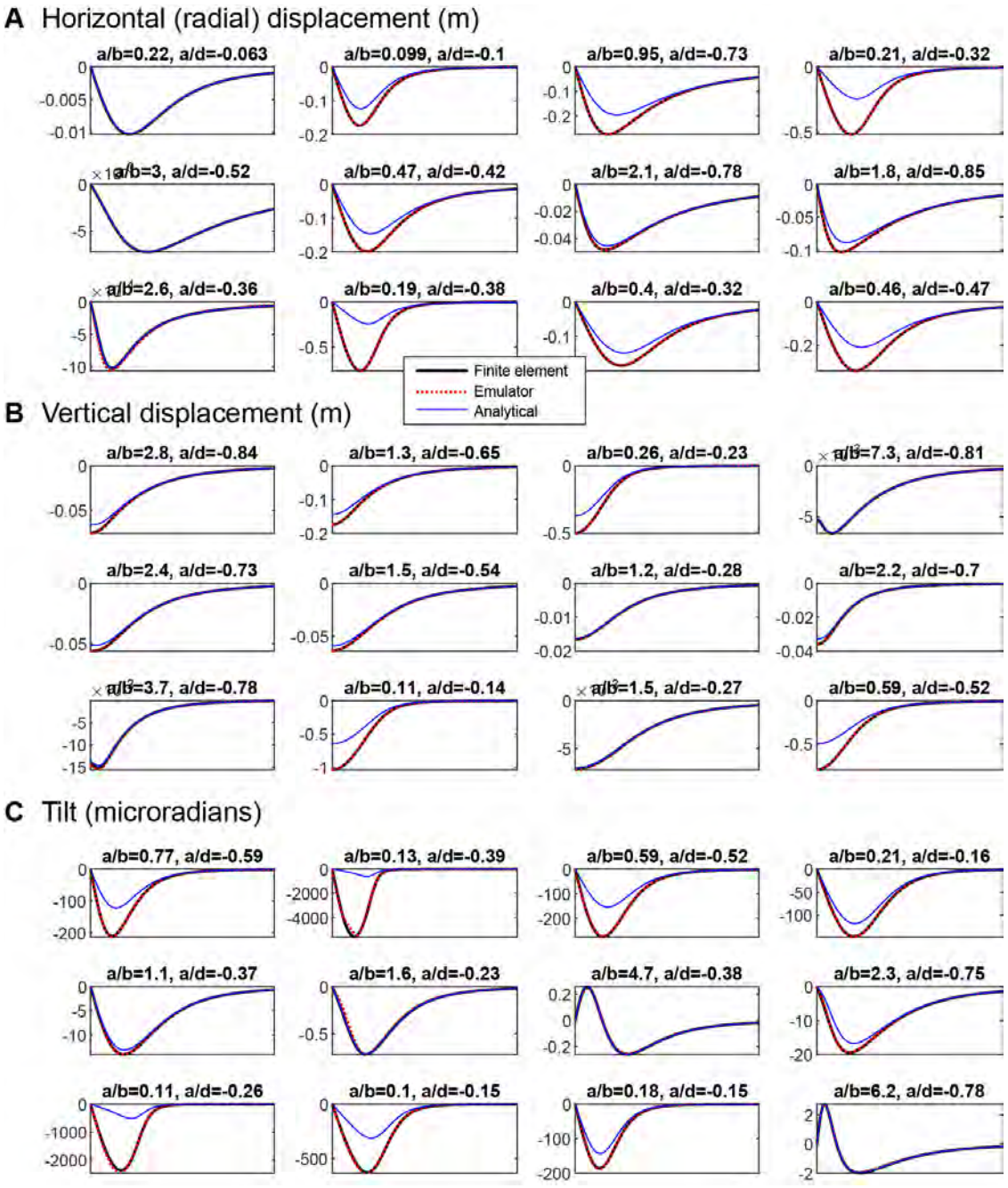

Fig. S13.

Comparison of finite element model, emulator, and analytical spheroid model for randomly-selected combinations of reservoir vertical dimension a, horizontal dimension b, and (negative) depth d. (**A**) Radial horizontal displacements. (**B**) Vertical displacements. (**C**) Tilt. In all cases the x axis extends from 0 km (left) to 10 km (right) from the reservoir centroid. Output from the emulator closely matches output from the finite element model. The analytical model diverges for particularly shallow and/or sill-like reservoirs, where it under-predicts deformation.

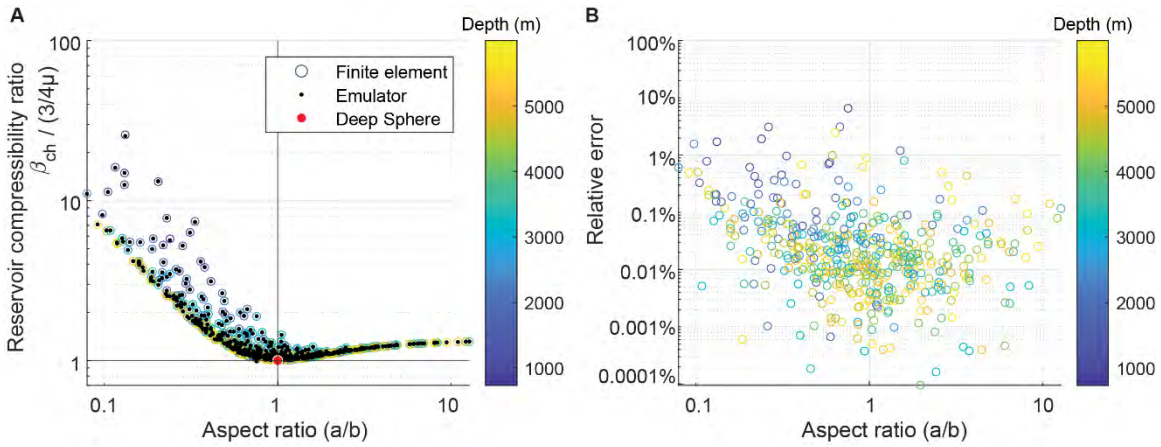

Fig. S14.

Compressibility of a spheroidal cavity in a homogeneous elastic halfspace with shear modulus of 20 GPa. (**A**) Magma compressibility (normalized by the compressibility of a deeply-buried sphere) as a function of reservoir aspect ratio. Open circles, colored by reservoir depth, show results for ~500 test geometries (which were not used to construct the emulator) computed using the finite element method; smaller black points show corresponding results from the emulator, which should ideally plot in the center of the open circles. Reservoirs on the right side of the figure are vertically prolate and those on the left are oblate (pancake-like). Vertical scatter in points (particularly for oblate reservoirs) is due to variability in reservoir depth. (**B**) Similar to (A) but showing relative error between the finite element model and the emulator. Relative error is nowhere above 10% and is usually <0.1% (RSME = 9×10^{-13}).

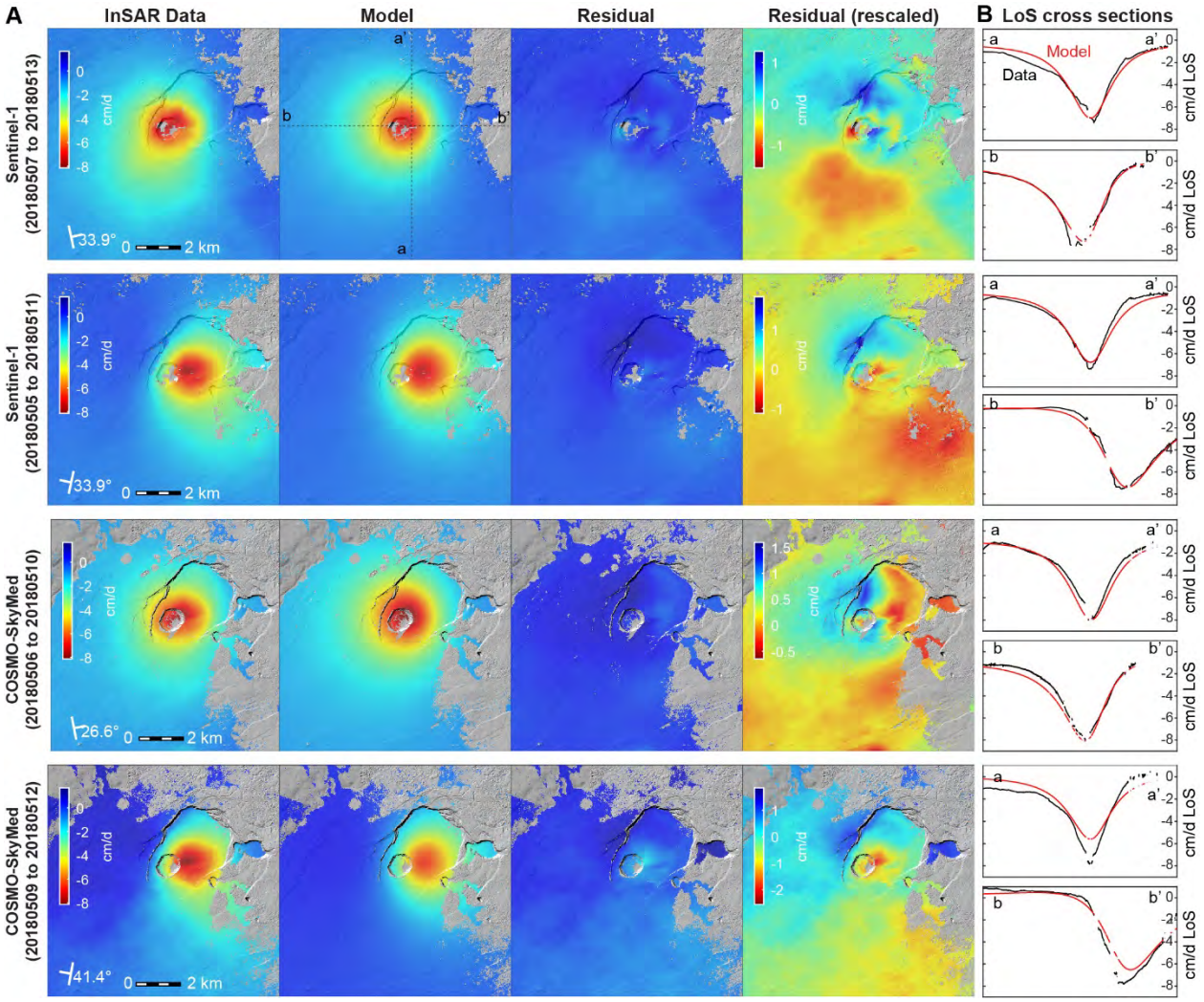

Fig. S15.

Fit of model predictions to InSAR data, following Fig. 6 in the main text, but also including data from the COSMO-SkyMed platform. (**A**) Unwrapped interferograms. (**B**) Line-of-sight cross sections through unwrapped interferograms in (A). Cross-section locations are denoted in (A).

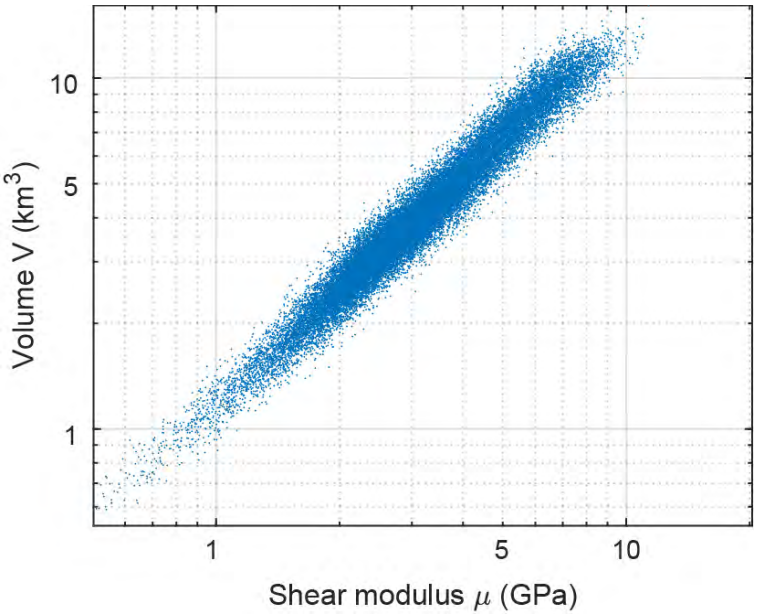

Fig. S16.

Relationship between reservoir volume and shear modulus for accepted MCMC samples, demonstrating the strong correlation. The slope of the correlation is governed by the ratio dV/dp (fig. S17) and scatter is in part due to variability in reservoir compressibility.

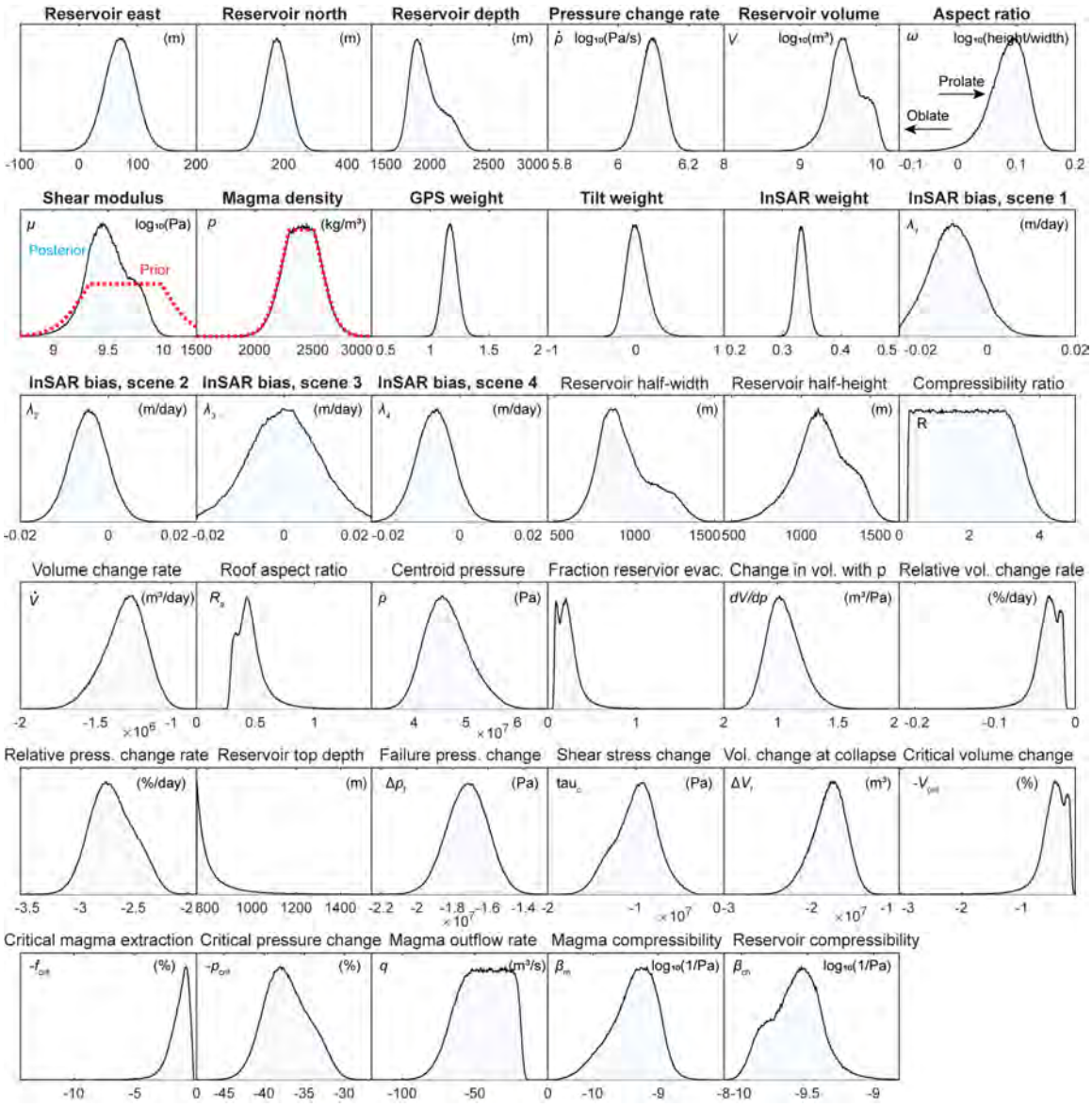

Fig. S17.

Marginal posterior distributions for estimated (bold text) and post-processed (plain text) model parameters. Prior PDFs are shown by dotted lines (uniform prior PDFs are not shown). Vertical axes indicate relative probability, which is not scaled between parameters. InSAR scene numbers correspond to table S1. When interpreting these distributions it is important to remember that they do not account for limitations in the model itself. In particular, the simple reservoir geometry utilized in this study accounts for the first-order pattern of deformation, but not its fine structure.

Table S1.

Interferograms used in this study. Number of data points given are for quadtree-decimated data. Acquisition times are HST.

	Satellite	Band	Mode	First acquisition	Second acquisition	Quadtree boxes
A	COSMO-SkyMed	X	Ascending	2018-05-06 06:06	2018-05-10 06:06	202
B	Sentinel-1	C	Ascending	2018-05-07 18:29	2018-05-13 18:29	280
C	COSMO-SkyMed	X	Descending	2018-05-08 17:58	2018-05-11 17:58	200
D	Sentinel-1	C	Descending	2018-05-05 06:15	2018-05-11 06:15	278

Table S2.

Parameter values estimated in the joint Bayesian estimation and also post-processed from those results. We do not include all nuisance parameters (magma density, InSAR bias terms, and data uncertainty hyperparameters); these are shown in fig. S17.

Parameter	Symbol or equation	Unit	Median	Lower 68%	Upper 68%
Bayesian parameter estimation					
Reservoir volume	V	km^3	3.94	2.53	7.23
Reservoir centroid east	-	m	70.3	44.0	96.2
Reservoir centroid north	-	m	183	157	210
Reservoir centroid depth	d	m	1940	1840	2120
Reservoir aspect (height/width)	ω	-	1.23	1.14	1.31
Pressure change rate	$\dot{p}$	MPa/d	1.25	1.15	1.34
Host rock shear modulus	μ	GPa	3.08	2.06	5.23
Post-processed and other estimated parameters					
Reservoir initial pressure	p_0	MPa	46.1	42.2	50.7
Reservoir volume change rate	$\dot{V}$	Mm^3/d	-1.30	-1.45	-1.17
Change in volume with pressure	dV/dp	m^3/Pa	1.04	0.918	1.19
Magma evacuation rate	q	m^3/s	-44.1	-62.1	-26.8
Relative volume change rate	$\dot{V}/V$	%/day	-0.0328	-0.0478	-0.0198
Relative pressure change rate	$\dot{p}/p_0$	%/day	-2.71	-2.91	-2.48
Failure press. change (16 May)	Δp_f	MPa	-17.2	-18.3	-16.0
Failure vol. change (16 May)	ΔV_f	m^3	-17.9	-20.0	-16.1
Reservoir compressibility	β_{ch}	1/Pa	2.63e-10	1.59e-10	3.86e-10
Magma compressibility	β_{m}	1/Pa	4.60e-10	1.83e-10	9.10e-10
Critical pressure change	p_{crit}	%	37.4	34.1	39.9
Critical volume change	V_{crit}	%	0.451	0.272	0.658
Critical magma evacuation	f_{crit}	%	1.23	0.684	2.15
Roof aspect ratio	R_a	-	0.473	0.341	0.551
Caldera vol. / reservoir vol.	-	%	20.9	11.4	32.7
Cylindrical fault stress change	τ_c	MPa	-9.83	-12.5	-7.71

Movie S1.

Time-lapse movie of thermal camera images (*82*) showing Kīlauea's lava lake from 25 April to 9 May, 2018. Overflows from the lava lake are visible in late April, followed by draining. The lake's surface withdrew by ~300 m, over much of this time at a near-constant rate of 53 m/d. Wallrock collapses and explosions are visible as the lake drained. An explosion on 9 May terminated the thermal camera's image stream.

References and Notes

1. H. Williams, in *Bulletin of the Department of Geological Sciences*, G. D. Louderback, C. A. Anderson, C. L. Camp, R. W. Chaney, H. Williams, Eds. (Univ. of California Publications, ed. 25, 1941), pp. 239–346.

2. A. Geyer, J. Martí, The new worldwide collapse caldera database (CCDB): A tool for studying and understanding caldera processes. *J. Volcanol. Geotherm. Res.* **175**, 334–354 (2008). doi:10.1016/j.jvolgeores.2008.03.017

3. M. T. Gudmundsson, K. Jónsdóttir, A. Hooper, E. P. Holohan, S. A. Halldórsson, B. G. Ófeigsson, S. Cesca, K. S. Vogfjörd, F. Sigmundsson, T. Högnadóttir, P. Einarsson, O. Sigmarsson, A. H. Jarosch, K. Jónasson, E. Magnússon, S. Hreinsdóttir, M. Bagnardi, M. M. Parks, V. Hjörleifsdóttir, F. Pálsson, T. R. Walter, M. P. J. Schöpfer, S. Heimann, H. I. Reynolds, S. Dumont, E. Bali, G. H. Gudfinnsson, T. Dahm, M. J. Roberts, M. Hensch, J. M. C. Belart, K. Spaans, S. Jakobsson, G. B. Gudmundsson, H. M. Fridriksdóttir, V. Drouin, T. Dürig, G. Aðalgeirsdóttir, M. S. Riishuus, G. B. M. Pedersen, T. van Boeckel, B. Oddsson, M. A. Pfeffer, S. Barsotti, B. Bergsson, A. Donovan, M. R. Burton, A. Aiuppa, Gradual caldera collapse at Bárdarbunga volcano, Iceland, regulated by lateral magma outflow. *Science* **353**, aaf8988 (2016). doi:10.1126/science.aaf8988 Medline

4. M. R. Patrick, K. R. Anderson, M. P. Poland, T. R. Orr, D. A. Swanson, Lava lake level as a gauge of magma reservoir pressure and eruptive hazard. *Geology* **43**, 831–834 (2015). doi:10.1130/G36896.1

5. M. Patrick, D. Swanson, T. Orr, A review of controls on lava lake level: Insights from Halema'uma'u Crater, Kīlauea Volcano. *Bull. Volcanol.* **81**, 13 (2019). doi:10.1007/s00445-019-1268-y

6. K. R. Anderson, M. P. Poland, J. H. Johnson, A. Miklius, "Episodic deflation-inflation events at Kīlauea Volcano and implications for the shallow magma system," chapter 11 in *Hawaiian Volcanism: From Source to Surface*, R. J. Carey, M. P. Poland, V. Cayol, D. Weis, Eds. (AGU Geophysical Monograph Series vol. 208, AGU, 2015), pp. 229–250; doi:10.1002/9781118872079.ch11.

7. C. A. Neal, S. R. Brantley, L. Antolik, J. L. Babb, M. Burgess, K. Calles, M. Cappos, J. C. Chang, S. Conway, L. Desmither, P. Dotray, T. Elias, P. Fukunaga, S. Fuke, I. A. Johanson, K. Kamibayashi, J. Kauahikaua, R. L. Lee, S. Pekalib, A. Miklius, W. Million, C. J. Moniz, P. A. Nadeau, P. Okubo, C. Parcheta, M. R. Patrick, B. Shiro, D. A. Swanson, W. Tollett, F. Trusdell, E. F. Younger, M. H. Zoeller, E. K. Montgomery-Brown, K. R. Anderson, M. P. Poland, J. L. Ball, J. Bard, M. Coombs, H. R. Dietterich, C. Kern, W. A. Thelen, P. F. Cervelli, T. Orr, B. F. Houghton, C. Gansecki, R. Hazlett, P. Lundgren, A. K. Diefenbach, A. H. Lerner, G. Waite, P. Kelly, L. Clor, C. Werner, K. Mulliken, G. Fisher, D. Damby, The 2018 rift eruption and summit collapse of Kīlauea Volcano. *Science* **363**, 367–374 (2019). doi:10.1126/science.aav7046 Medline

8. Materials and methods are available as supplementary materials.

9. M. R. Patrick, E. F. Younger, W. Tollett, Lava level and crater geometry data during the 2018 lava lake draining at Kilauea Volcano, Hawaii, ScienceBase (2019); doi:10.5066/P9MJY24N.

10. H. L. Kehoe, E. D. Kiser, P. G. Okubo, The rupture process of the 2018 Mw 6.9 Hawai‘i earthquake as imaged by a genetic algorithm-based back-projection technique. *Geophys. Res. Lett.* **46**, 2467–2474 (2019). doi:10.1029/2018GL080397

11. P. Dawson, B. Chouet, Characterization of very-long-period seismicity accompanying summit activity at Kīlauea Volcano, Hawai‘i: 2007–2013. *J. Volcanol. Geotherm. Res.* **278–279**, 59–85 (2014). doi:10.1016/j.jvolgeores.2014.04.010

12. H. Munekane, J. Oikawa, T. Kobayashi, Mechanisms of step-like tilt changes and very long period seismic signals during the 2000 Miyakejima eruption: Insights from kinematic GPS. *J. Geophys. Res.* **121**, 2932–2946 (2016). doi:10.1002/2016JB012795

13. T. Staudacher, V. Ferrazzini, A. Peltier, P. Kowalski, P. Boissier, P. Catherine, F. Lauret, F. Massin, The April 2007 eruption and the Dolomieu crater collapse, two major events at Piton de la Fournaise (La Réunion Island, Indian Ocean). *J. Volcanol. Geotherm. Res.* **184**, 126–137 (2009). doi:10.1016/j.jvolgeores.2008.11.005

14. L. Michon, N. Villeneuve, T. Catry, O. Merle, How summit calderas collapse on basaltic volcanoes : New insights from the April 2007 caldera collapse of Piton de la Fournaise volcano. *J. Volcanol. Geotherm. Res.* **184**, 138–151 (2009). doi:10.1016/j.jvolgeores.2008.11.003

15. H. Kumagai, T. Ohminato, M. Nakano, M. Ooi, A. Kubo, H. Inoue, J. Oikawa, Very-long-period seismic signals and caldera formation at Miyake Island, Japan. *Science* **293**, 687–690 (2001). doi:10.1126/science.1062136 Medline

16. M. R. Patrick, H. R. Dietterich, L. J. Lyons, A. K. Diefenbach, C. Parcheta, K. R. Anderson, A. Namiki, I. Sumita, J. P. Kauahikaua, Cyclic lava effusion during the 2018 eruption of Kīlauea Volcano. *Science* **366**, eaay9070 (2019). doi:10.1126/science.aay9070

17. M. Gu, J. O. Berger, Parallel partial Gaussian process emulation for computer models with massive output. *Ann. Appl. Stat.* **10**, 1317–1347 (2016). doi:10.1214/16-AOAS934

18. O. Roche, T. H. Druitt, Onset of caldera collapse during ignimbrite eruptions. *Earth Planet. Sci. Lett.* **191**, 191–202 (2001). doi:10.1016/S0012-821X(01)00428-9

19. A. Geyer, A. Folch, J. Martí, Relationship between caldera collapse and magma chamber withdrawal: An experimental approach. *J. Volcanol. Geotherm. Res.* **157**, 375–386 (2006). doi:10.1016/j.jvolgeores.2006.05.001

20. N. Geshi, J. Ruch, V. Acocella, Evaluating volumes for magma chambers and magma withdrawn for caldera collapse. *Earth Planet. Sci. Lett.* **396**, 107–115 (2014). doi:10.1016/j.epsl.2014.03.059

21. S. Kusumoto, A. Gudmundsson, Magma-chamber volume changes associated with ring-fault initiation using a finite-sphere model: Application to the Aira caldera, Japan. *Tectonophysics* **471**, 58–66 (2009). doi:10.1016/j.tecto.2008.09.001

22. B. M. Kennedy, E. P. Holohan, J. Stix, D. M. Gravley, J. R. J. Davidson, J. W. Cole, Magma plumbing beneath collapse caldera volcanic systems. *Earth Sci. Rev.* **177**, 404–424 (2018). doi:10.1016/j.earscirev.2017.12.002

23. J. Martí, A. Geyer, A. Folch, J. Gottsmann, in *Caldera Volcanism: Analysis Modelling and Response* (Elsevier, 2008), vol. 10, pp. 233–283.

24. A. Di Muro, N. Métrich, D. Vergani, M. Rosi, P. Armienti, T. Fougeroux, E. Deloule, I. Arienzo, L. Civetta, The shallow plumbing system of Piton de la Fournaise Volcano (La Réunion Island, Indian Ocean) revealed by the major 2007 caldera-forming eruption. *J. Petrol.* **55**, 1287–1315 (2014). doi:10.1093/petrology/egu025

25. G. Saito, Y. Morishita, H. Shinohara, Magma plumbing system of the 2000 eruption of Miyakejima volcano, Japan, deduced from volatile and major component contents of olivine-hosted melt inclusions. *J. Geophys. Res.* **115**, B11202 (2010). doi:10.1029/2010JB007433

26. M. Bagnardi, F. Amelung, Space-geodetic evidence for multiple magma reservoirs and subvolcanic lateral intrusions at Fernandina Volcano, Galápagos Islands. *J. Geophys. Res.* **117**, 1–19 (2012). doi:10.1029/2012JB009465

27. A. Belousov, M. Belousova, B. Edwards, A. Volynets, D. Melnikov, Overview of the precursors and dynamics of the 2012–13 basaltic fissure eruption of Tolbachik Volcano, Kamchatka, Russia. *J. Volcanol. Geotherm. Res.* **307**, 22–37 (2015). doi:10.1016/j.jvolgeores.2015.06.013

28. W. W. Chadwick, S. Jónsson, D. J. Geist, M. Poland, D. J. Johnson, S. Batt, K. S. Harpp, A. Ruiz, The May 2005 eruption of Fernandina volcano, Galápagos: The first circumferential dike intrusion observed by GPS and InSAR. *Bull. Volcanol.* **73**, 679–697 (2011). doi:10.1007/s00445-010-0433-0

29. D. A. Swanson, T. R. Rose, A. E. Mucek, M. O. Garcia, R. S. Fiske, L. G. Mastin, Cycles of explosive and effusive eruptions at Kīlauea Volcano, Hawai‘i. *Geology* **42**, 631–634 (2014). doi:10.1130/G35701.1

30. W. Ellis, *Narrative of a Tour Through Hawaii, Or Owhyhee* (Fisher and Jackson, 1825).

31. S. Baker, F. Amelung, Top-down inflation and deflation at the summit of Kīlauea Volcano, Hawaii observed with InSAR. *J. Geophys. Res.* **117**, B12406 (2012). doi:10.1029/2011JB009123

32. R. S. Fiske, W. T. Kinoshita, Inflation of Kilauea volcano prior to its 1967–1968 eruption. *Science* **165**, 341–349 (1969). doi:10.1126/science.165.3891.341 Medline

33. P. F. Cervelli, A. Miklius, in *The Pu'u 'O'o-Kupaianaha Eruption of Kilauea Volcano, Hawai'i: The First 20 Years*, C. Heliker, D. Swanson, J. T. Takahashi, Eds. (USGS Professional Paper 1676, 2003), pp. 149–164.

34. M. P. Poland, J. Sutton, T. M. Gerlach, Magma degassing triggered by static decompression at Kilauea Volcano, Hawai‘i. *Geophys. Res. Lett.* **36**, L16306 (2009). doi:10.1029/2009GL039214

35. P. Lundgren, M. Poland, A. Miklius, T. Orr, S. Yun, E. Fielding, Z. Liu, A. Tanaka, W. Szeliga, S. Hensley, S. Owen, Evolution of dike opening during the March 2011 Kamoamoa fissure eruption, Kīlauea Volcano, Hawai‘i. *J. Geophys. Res.* **118**, 897–914 (2013). doi:10.1002/jgrb.50108

36. M. P. Poland, A. Miklius, E. K. Montgomery-Brown, Magma supply, storage, and transport at shield-stage Hawaiian volcanoes. *U.S. Geol. Surv. Prof. Pap. 1801*. **2010**, 1–52 (2014).

37. K. R. Anderson, M. P. Poland, Bayesian estimation of magma supply, storage, and eruption rates using a multiphysical volcano model: Kīlauea Volcano, 2000–2012. *Earth Planet. Sci. Lett.* **447**, 161–171 (2016). doi:10.1016/j.epsl.2016.04.029

38. J. Dvorak, A. Okamura, J. H. Dieterich, Analysis of surface deformation data, Kilauea Volcano, Hawaii: October 1966 to September 1970. *J. Geophys. Res.* **88**, 9295–9304 (1983). doi:10.1029/JB088iB11p09295

39. T. Ohminato, B. A. Chouet, P. Dawson, S. Kedar, Waveform inversion of very long period impulsive signals associated with magmatic injection beneath Kilauea volcano, Hawaii. *J. Geophys. Res.* **103**, 23839–23862 (1998). doi:10.1029/98JB01122

40. B. Chouet, P. Dawson, Seismic source dynamics of gas-piston activity at Kīlauea Volcano, Hawai‘i. *J. Geophys. Res.* **120**, 2525–2560 (2015). doi:10.1002/2014JB011789

41. P. Segall, P. Cervelli, S. Owen, M. Lisowski, A. Miklius, Constraints on dike propagation from continuous GPS measurements. *J. Geophys. Res.* **106**, 19301–19317 (2001). doi:10.1029/2001JB000229

42. D. J. Johnson, Dynamics of magma storage in the summit reservoir of Kilauea Volcano, Hawaii. *J. Geophys. Res.* **97**, 1807–1820 (1992). doi:10.1029/91JB02839

43. A. J. Pietruszka, D. E. Heaton, J. P. Marske, M. O. Garcia, Two magma bodies beneath the summit of Kīlauea Volcano unveiled by isotopically distinct melt deliveries from the mantle. *Earth Planet. Sci. Lett.* **413**, 90–100 (2015). doi:10.1016/j.epsl.2014.12.040

44. A. J. Pietruszka, J. P. Marske, D. E. Heaton, M. O. Garcia, J. M. Rhodes, An isotopic perspective into the magmatic evolution and architecture of the rift zones of Kīlauea Volcano. *J. Petrol.* **59**, 2311–2352 (2018). doi:10.1093/petrology/egy098

45. D. F. McTigue, Elastic stress and deformation near a finite spherical magma body: Resolution of the point source paradox. *J. Geophys. Res.* **92**, 12931 (1987). doi:10.1029/JB092iB12p12931

46. T. L. Wright, F. W. Klein, in *Dynamics of Crustal Magma Transfer, Storage and Differentiation*, C. Annen, G. F. Zellmer, Eds. (Geological Society of London, 2008), vol. 304, pp. 83–116; doi:10.1144/SP304.5.

47. D. Dzurisin, M. P. Poland, in *Field Volcanology: A Tribute to the Distinguished Career of Don Swanson*, M. P. Poland, M. O. Garcia, V. E. Cam, A. Grunder, Eds. (Geological Society of America, 2018), vol. 2538, pp. 275–295.

48. P. R. Lundgren, M. Bagnardi, H. Dietterich, Topographic changes during the 2018 Kīlauea eruption from single-pass airborne InSAR. *Geophys. Res. Lett.* **46**, 9554–9562 (2019). doi:10.1029/2019GL083501

49. L. Michon, F. Massin, V. Famin, V. Ferrazzini, G. Roult, Basaltic calderas: Collapse dynamics, edifice deformation, and variations of magma withdrawal. *J. Geophys. Res.* **116**, B03209 (2011). doi:10.1029/2010JB007636

50. P. Segall, K. R. Anderson, I. Johanson, A. Miklius, Mechanics of inflationary deformation during caldera collapse: Evidence from the 2018 Kīlauea eruption. *Geophys. Res. Lett.* 2019GL084689 (2019). doi:10.1029/2019GL084689

51. E. P. Holohan, M. P. J. Schöpfer, J. J. Walsh, Mechanical and geometric controls on the structural evolution of pit crater and caldera subsidence. *J. Geophys. Res.* **116**, B07202 (2011). doi:10.1029/2010JB008032

52. O. Roche, T. H. Druitt, O. Merle, Experimental study of caldera formation. *J. Geophys. Res. Solid Earth* **105**, 395–416 (2000). doi:10.1029/1999JB900298

53. R. Scandone, V. Acocella, Control of the aspect ratio of the chamber roof on caldera formation during silicic eruptions. *Geophys. Res. Lett.* **34**, L22307 (2007). doi:10.1029/2007GL032059

54. J. Stix, T. Kobayashi, Magma dynamics and collapse mechanisms during four historic caldera-forming events. *J. Geophys. Res.* **113**, B09205 (2008). doi:10.1029/2007JB005073

55. A. Folch, J. Martí, Time-dependent chamber and vent conditions during explosive caldera-forming eruptions. *Earth Planet. Sci. Lett.* **280**, 246–253 (2009). doi:10.1016/j.epsl.2009.01.035

56. J. Martí, A. Folch, A. Neri, M. Giovanni, Pressure evolution during explosive caldera-forming eruptions. *Earth Planet. Sci. Lett.* **175**, 275–287 (2000). doi:10.1016/S0012-821X(99)00296-4

57. B. A. Chouet, P. B. Dawson, M. R. James, S. J. Lane, Seismic source mechanism of degassing bursts at Kilauea Volcano, Hawaii: Results from waveform inversion in the 10–50 s band. *J. Geophys. Res.* **115**, B09311 (2010). doi:10.1029/2009JB006661

58. D. R. Shelly, W. Thelen, P. Okubo, "Anatomy of a caldera collapse: Kilauea 2018 summit seismicity sequence in high resolution," presented at the Seismological Society of America Annual Meeting, Seattle, WA, 23 to 26 April 2019.

59. T. H. Druitt, R. S. J. Sparks, On the formation of calderas during ignimbrite eruptions. *Nature* **310**, 679–681 (1984). doi:10.1038/310679a0

60. S. M. Bower, A. W. Woods, Control of magma volatile content and chamber depth on the mass erupted during explosive volcanic eruptions. *J. Geophys. Res.* **102**, 10273–10290 (1997). doi:10.1029/96JB03176

61. T. Simkin, K. A. Howard, Caldera collapse in the Galápagos Islands, 1968. *Science* **169**, 429–437 (1970). doi:10.1126/science.169.3944.429 Medline

62. E. P. Holohan, M. P. J. Schöpfer, J. J. Walsh, Stress evolution during caldera collapse. *Earth Planet. Sci. Lett.* **421**, 139–151 (2015). doi:10.1016/j.epsl.2015.03.003

63. L. Gailler, J. Kauahikaua, J. Lénat, A. Revil, M. Gresse, A. S. Ahmed, N. Cluzel, G. Manthilake, L. Gurioli, T. Johnson, A. Finizola, E. Delcher, 3D electrical conductivity imaging of Halema'uma'u lava lake (Kīlauea volcano). *J. Volcanol. Geotherm. Res.* **381**, 185–192 (2019). doi:10.1016/j.jvolgeores.2019.06.001

64. P. W. Lipman, Subsidence of ash-flow calderas: Relation to caldera size and magma-chamber geometry. *Bull. Volcanol.* **59**, 198–218 (1997). doi:10.1007/s004450050186

65. European Space Agency Sentinel Data Access; https://sentinel.esa.int/web/sentinel/sentinel-data-access.

66. Hawaiian Volcanoes Supersite; http://geo-gsnl.org/supersites/permanent-supersites/hawaiian-volcanoes-supersite/.

67. National Center for Airborne Laser Mapping, Hawaii Big Island Survey, OpenTopography (2012); doi:10.5069/G9DZ067X.

68. Kīlauea LiDAR Data (2018); https://kilauealidar.com.

69. I. A. Johanson, A. Miklius, Tiltmeter data from Kīlauea Volcano, Hawaii, spanning the 2018 eruption and earthquake sequence. U.S. Geological Survey data release, ScienceBase (2019); doi:10.5066/P9310M9N.

70. UNAVCO; https://unavco.org.

71. J. H. Johnson, M. P. Poland, K. R. Anderson, J. Biggs, A cautionary tale of topography and tilt from Kīlauea Caldera. *Geophys. Res. Lett.* **46**, 4221–4229 (2019). doi:10.1029/2018GL081757

72. M. L. Kohl, J. Levine, Measuring low frequency tilts. *J. Res. Natl. Inst. Stand. Technol.* **98**, 191–202 (1993). doi:10.6028/jres.098.014 Medline

73. K. Anderson, M. Lisowski, P. Segall, Cyclic ground tilt associated with the 2004-2008 eruption of Mount St. Helens. *J. Geophys. Res.* **115**, B11201 (2010). doi:10.1029/2009JB007102

74. D. C. Agnew, Strainmeters and tiltmeters. *Rev. Geophys.* **24**, 579–624 (1986). doi:10.1029/RG024i003p00579

75. T. G. Farr, P. A. Rosen, E. Caro, R. Crippen, R. Duren, S. Hensley, M. Kobrick, M. Paller, E. Rodriguez, L. Roth, D. Seal, S. Shaffer, J. Shimada, J. Umland, M. Werner, M. Oskin, D. Burbank, D. Alsdorf, The shuttle radar topography mission. *Rev. Geophys.* **45**, RG2004 (2007). doi:10.1029/2005RG000183

76. M. P. Poland, Time-averaged discharge rate of subaerial lava at Kīlauea Volcano, Hawai‘i, measured from TanDEM-X interferometry: Implications for magma supply and storage during 2011-2013. *J. Geophys. Res.* **119**, 5464–5481 (2014). doi:10.1002/2014JB011132

77. R. M. Goldstein, C. L. Werner, Radar interferogram filtering for geophysical applications. *Geophys. Res. Lett.* **25**, 4035–4038 (1998). doi:10.1029/1998GL900033

78. C. W. Chen, H. A. Zebker, Phase unwrapping for large SAR interferograms: Statistical segmentation and generalized network models. *IEEE Trans. Geosci. Remote Sens.* **40**, 1709–1719 (2002). doi:10.1109/TGRS.2002.802453

79. R. B. Lohman, M. Simons, Some thoughts on the use of InSAR data to constrain models of surface deformation: Noise structure and data downsampling. *Geochem. Geophys. Geosyst.* **6**, Q01007 (2005). doi:10.1029/2004GC000841

80. S. Jonsson, H. Zebker, P. Segall, F. Amelung, Fault slip distribution of the 1999 Mw 7.1 Hector Mine, California, earthquake, estimated from satellite radar and GPS measurements. *Bull. Seismol. Soc. Am.* **92**, 1377–1389 (2002). doi:10.1785/0120000922

81. H. Sudhaus, S. Jónsson, Improved source modelling through combined use of InSAR and GPS under consideration of correlated data errors: Application to the June 2000

Kleifarvatn earthquake, Iceland. *Geophys. J. Int.* **176**, 389–404 (2009). doi:10.1111/j.1365-246X.2008.03989.x

82. M. R. Patrick, T. Orr, L. Antolik, L. Lee, K. Kamibayashi, Continuous monitoring of Hawaiian volcanoes with thermal cameras. *J. Appl. Volcanol.* **3**, 1 (2014). doi:10.1186/2191-5040-3-1

83. D. Carbone, M. P. Poland, M. R. Patrick, T. R. Orr, Continuous gravity measurements reveal a low-density lava lake at Kīlauea Volcano, Hawai‘i. *Earth Planet. Sci. Lett.* **376**, 178–185 (2013). doi:10.1016/j.epsl.2013.06.024

84. M. P. Poland, D. Carbone, Insights into shallow magmatic processes at Kīlauea Volcano, Hawai‘i, from a multiyear continuous gravity time series. *J. Geophys. Res. Solid Earth* **121**, 5477–5492 (2016). doi:10.1002/2016JB013057

85. J. Kauahikaua, T. Hildenbrand, M. Webring, Deep magmatic structures of Hawaiian volcanoes, imaged by three-dimensional gravity models. *Geology* **28**, 883 (2000). doi:10.1130/0091-7613(2000)28<883:DMSOHV>2.0.CO;2

86. G. Lin, F. Amelung, P. M. Shearer, P. G. Okubo, Location and size of the shallow magma reservoir beneath Kīlauea caldera, constraints from near-source Vp / Vs ratios. *Geophys. Res. Lett.* **42**, 8349–8357 (2015). doi:10.1002/2015GL065802

87. T. M. Brocher, Empirical relations between elastic wavespeeds and density in the Earth’s crust. *Bull. Seismol. Soc. Am.* **95**, 2081–2092 (2005). doi:10.1785/0120050077

88. L. Gailler, in *Field Volcanology: A Tribute to the Distinguished Career of Don Swanson*, M. P. Poland, M. Garcia, V. E. Camp, A. Grunder, Eds. (Geological Society of America, 2018), pp. 297–306; doi:10.1130/2018.2538(13).

89. M. H. Manghnani, G. P. Woollard, “Elastic wave velocities in Hawaiian rocks at pressures to ten kilobars” in *The Crust and Upper Mantle of the Pacific Area*, L. Knopoff, C. L. Drake, P. J. Hart, Eds. (Geophysical Monograph Series, AGU, 1968), vol. 12, pp. 501–516.

90. P. M. Davis, D. B. Jackson, J. Field, F. D. Stacey, Kilauea volcano, hawaii: A search for the volcanomagnetic effect. *Science* **180**, 73–74 (1973). doi:10.1126/science.180.4081.73 Medline

91. G. Lin, P. M. Shearer, R. S. Matoza, P. G. Okubo, F. Amelung, Three-dimensional seismic velocity structure of Mauna Loa and Kilauea volcanoes in Hawaii from local seismic tomography. *J. Geophys. Res.* **119**, 4377–4392 (2014). doi:10.1002/2013JB010820

92. C. H. Cheng, D. H. Johnston, Dynamic and static moduli. *Geophys. Res. Lett.* **8**, 39–42 (1981). doi:10.1029/GL008i001p00039

93. G. De Natale, F. Pingue, in *Monitoring and Mitigation of Volcano Hazards*, R. Scarpa, R. I. Tilling, Eds. (Springer, 1996), pp. 365–388.

94. X.-M. Yang, P. M. Davis, J. H. Dieterich, Deformation from inflation of a dipping finite prolate spheroid in an elastic half-space as a model for volcanic stressing. *J. Geophys. Res.* **93**, 4249–4257 (1988). doi:10.1029/JB093iB05p04249

95. P. F. Cervelli, Analytical Expressions for Deformation from an Arbitrarily Oriented Spheroid in a Half-Space. *AGU Fall Meeting*, abstract V44C-06 (AGU, 2013); https://ui.adsabs.harvard.edu/abs/2013AGUFM.V44C..06C/abstract.

96. J. H. Dieterich, R. W. Decker, Finite element modeling of surface deformation associated with volcanism. *J. Geophys. Res.* **80**, 4094–4102 (1975). doi:10.1029/JB080i029p04094

97. J. Hickey, J. Gottsmann, P. Mothes, Estimating volcanic deformation source parameters with a finite element inversion: The 2001–2002 unrest at Cotopaxi volcano, Ecuador. *J. Geophys. Res.* **120**, 1473–1486 (2015). doi:10.1002/2014JB011731

98. J. Sacks, W. J. Welch, T. J. Mitchell, H. P. Wynn, Design and Analysis of Computer Experiments. *Stat. Sci.* **4**, 409–423 (1989). doi:10.1214/ss/1177012413

99. M. J. Bayarri, J. O. Berger, R. Paulo, J. Sacks, J. A. Cafeo, J. Cavendish, C.-H. Lin, J. Tu, A framework for validation of computer models. *Technometrics* **49**, 138–154 (2007). doi:10.1198/004017007000000092

100. M. J. Bayarri, J. O. Berger, E. S. Calder, K. Dalbey, S. Lunagomez, A. K. Patra, E. B. Pitman, E. T. Spiller, R. L. Wolpert, Using statistical and computer models to quantify volcanic hazards. *Technometrics* **51**, 402–413 (2009). doi:10.1198/TECH.2009.08018

101. M. Gu, X. Wang, J. O. Berger, Robust Gaussian stochastic process emulation. *Ann. Stat.* **46**, 3038–3066 (2018). doi:10.1214/17-AOS1648

102. M. Gu, Jointly robust prior for Gaussian stochastic process in emulation, calibration and variable selection. *Bayesian Anal.* **14**, 857–885 (2019). doi:10.1214/18-BA1133

103. M. Gu, J. Palomo, J. O. Berger, RobustGaSP: Robust Gaussian stochastic process emulation in R. *R J.* **201**, 112–136 (2018). doi:10.32614/RJ-2019-011

104. M. Gu, RobustGaSP: Robust Gaussian stochastic process emulation in MATLAB, version v0.5.0, Zenodo (2019); doi:10.5281/zenodo.3370575.

105. T. J. Santner, *The Design and Analysis of Computer Experiments* (Springer, 2003).

106. M. C. Kennedy, A. O'Hagan, Bayesian Calibration of Computer Models. *J. R. Stat. Soc. Ser. B* **63**, 425–464 (2001). doi:10.1111/1467-9868.00294

107. J. Fukuda, K. M. Johnson, A fully Bayesian inversion for spatial distribution of fault slip with objective smoothing. *Bull. Seismol. Soc. Am.* **98**, 1128–1146 (2008). doi:10.1785/0120070194

108. N. Metropolis, A. W. Rosenbluth, M. N. Rosenbluth, A. H. Teller, E. Teller, Equation of state calculations by fast computing machines. *J. Chem. Phys.* **21**, 1087–1092 (1953). doi:10.1063/1.1699114

109. K. Mosegaard, A. Tarantola, Monte Carlo sampling of solutions to inverse problems. *J. Geophys. Res.* **100**, 12431–12447 (1995). doi:10.1029/94JB03097

110. K. Anderson, P. Segall, Physics-based models of ground deformation and extrusion rate at effusively erupting volcanoes. *J. Geophys. Res.* **116**, B07204 (2011). doi:10.1029/2010JB007939

111. A. Amoruso, L. Crescentini, Shape and volume change of pressurized ellipsoidal cavities from deformation and seismic data. *J. Geophys. Res.* **114**, B02210 (2009). doi:10.1029/2008JB005946

112. E. Rivalta, P. Segall, Magma compressibility and the missing source for some dike intrusions. *Geophys. Res. Lett.* **35**, L04306 (2008). doi:10.1029/2007GL032521

113. L. G. Mastin, E. Roeloffs, N. M. Beeler, J. E. Quick, in *A Volcano Rekindled: The Renewed Eruption of Mount St. Helens, 2004-2006*, D. R. Sherrod, W. E. Scott, P. H. Stauffer, Eds. (USGS Professional Paper 1750, 2008), pp. 461–488.

114. K. Anderson, P. Segall, Bayesian inversion of data from effusive volcanic eruptions using physics-based models: Application to Mount St. Helens 2004-2008. *J. Geophys. Res.* **118**, 2017–2037 (2013). doi:10.1002/jgrb.50169

115. A. Geyer, J. Martí, A short review of our current understanding of the development of ring faults during collapse caldera formation. *Front. Earth Sci.* 10.3389/feart.2014.00022 (2014). doi:10.3389/feart.2014.00022

116. V. Acocella, Understanding caldera structure and development: An overview of analogue models compared to natural calderas. *Earth Sci. Rev.* **85**, 125–160 (2007). doi:10.1016/j.earscirev.2007.08.004

117. Y. Liu, J. Ruch, H. Vasyura-bathke, S. Jónsson, Influence of ring faulting in localizing surface deformation at subsiding calderas. *Earth Planet. Sci. Lett.* **526**, 115784 (2019). doi:10.1016/j.epsl.2019.115784